

# Nano-antenna-assisted high-order harmonic generation

Von der Fakultät für Mathematik und Physik  
der Gottfried Wilhelm Leibniz Universität Hannover  
zur Erlangung des Grades

**Doktor der Naturwissenschaften**

- Dr. rer. nat. -

genehmigte Dissertation

von

**Dipl.-Phys. Nils Pfullmann**

geboren am 16.03.1983 in Stade

2012

Referent: Prof. Dr. Uwe Morgner  
Korreferent: Prof. Dr. John Tisch  
Korreferent: Prof. Dr. Manfred Lein  
Prüfungsvorsitz: Prof. Dr. Reinhard Werner  
Tag der Promotion: 17.07.2012

## Kurzfassung

Nils Pfullmann

### Erzeugung Hoher Harmonischer Strahlung mit Hilfe von Nanoantennen

Bei der Erzeugung Hoher Harmonischer Strahlung mit Laserpulsen direkt aus einem Laser Oszillator können die Frequenzkammeigenschaften des Laseroszillators auf die Harmonischen Strahlung übertragen werden. Dies ermöglicht neuartige Spektroskopie Experimente im extremen ultravioletten Spektralbereich. Auf Grund des stark nicht-linearen Konversionsprozesses werden hierfür jedoch hohe Spitzenintensitäten von mindestens  $10^{13} \text{ W cm}^{-2}$  im Fokus benötigt. Diese können zum Beispiel mit einem externen Überhöhungsresonator realisiert werden, der jedoch sehr komplex ist.

Im Rahmen dieser Arbeit werden Nanoantennen und ihre plasmonischen Resonanzen sowohl theoretisch als auch experimentell als alternativer Ansatz untersucht. Innerhalb des Spaltvolumens zwischen den einzelnen Antennenarmen zeigen resonant gewählte Nanoantennen eine Intensitätsüberhöhung von mehr als zwei Größenordnungen. Entsprechend können in Kombination mit einem harten Fokus die benötigten Spitzenintensitäten erreicht werden. Mittels numerischer Simulationen werden sowohl die Intensitätsüberhöhung als auch die thermischen Eigenschaften der Antennen untersucht. Aus den Simulationen ergibt sich eine längenabhängige Zerstörschwelle für die Antennen, die in eine Optimierung der Antennen eingeht um eine thermische Zerstörung zu vermeiden. Darüber hinaus werden die Phasenanpassungsbedingungen für Hohe Harmonische Strahlung im Bereich der Nanoantennen numerisch bestimmt. Innerhalb des Erzeugungsvolumens der Antennen, ergibt sich eine perfekte Phasenanpassung. Experimentell werden die optischen Antennen mittels der erzeugten dritten Harmonischen Strahlung charakterisiert und Spitzenintensitäten im Bereich von  $10^{13} \text{ W cm}^{-2}$  bis  $10^{14} \text{ W cm}^{-2}$  beobachtet. Darüber hinaus wird der zur Erzeugung verwendete Gasstrahl genau vermessen und die Anzahl der zur Frequenzkonversion zur Verfügung stehenden Atome bestimmt. Diese ist um Faktor zwanzig höher als in vergleichbaren Experimenten. In den gemessenen Spektren finden sich deutliche Beiträge von Spektrallinien, die von neutralem und einfach ionisiertem Xenon stammen. Darüber hinaus werden Photonen detektiert, die zu Harmonischen der Fundamental-frequenz passen. Allerdings liegen diese in der Nähe von Spektrallinien, so dass der Erzeugungsprozess durch spektrale Messungen alleine nicht bestimmt werden kann.

**Schlagwörter:** Plasmonik, Optische Antennen, Erzeugung Hoher Harmonischer Strahlung

## Abstract

Nils Pfullmann

### Nano-antenna-assisted high-order harmonic generation

High-order harmonic generation directly from a laser oscillator allows the transfer of the mode-comb properties of the oscillator to the harmonics and hence enables spectroscopic applications in the extreme ultraviolet spectral region. Due to the highly non-linear frequency conversion process, high peak intensities of at least  $10^{13} \text{ W cm}^{-2}$  are necessary in the focal spot. These can for instance be reached by external enhancement cavities, which add significant complexity to the overall system.

In this thesis nano-antennas and their plasmonic resonances are analysed both theoretically and experimentally as an alternative scheme to reach the required peak intensities. Resonant nano-antennas typically exhibit an intensity enhancement in the feedgap of more than two orders of magnitude and are therefore promising candidates. In numerical simulations based on the finite difference time domain technique, the achievable intensity enhancement as well as the thermal antenna properties are determined. A damage threshold dependent on antenna length is predicted, which is used to optimise the structures and avoid thermal damage. Furthermore, the phase-matching conditions for nano-antenna assisted high-order harmonic generation are numerically examined. Perfect phase-matching is found at the relevant length scale of the antenna thickness. Experimentally the optical antennas are characterised with the third harmonic radiation generated at the surface of the substrate. Peak intensities of  $10^{13} \text{ W cm}^{-2}$  to  $10^{14} \text{ W cm}^{-2}$  have emerged, thus confirming the feasibility of nano-antenna assisted high-order harmonic generation. Additionally a detailed analysis of the gas jet reveals a number of atoms at the sample twenty times higher than previously anticipated in similar experiments. Measured spectra contain contributions from various discrete transitions from neutral and single ionised xenon, which underlines the achieved peak intensities in the feedgap. Moreover, spectral peaks coinciding with harmonics of the driving laser are observed. However, they are in close proximity to atomic transitions and can therefore not be unambiguously attributed to a particular generation scheme solely by spectral measurements.

**Key words:** plasmonics, optical antennas, high-order harmonic generation

---

# Contents

---

<b>1</b>	<b>Introduction</b>	<b>1</b>
<b>2</b>	<b>Optical antennas and plasmons</b>	<b>5</b>
2.1	Classical antennas and scalability to optical frequencies . . . . .	5
2.2	Maxwell's equations in matter at optical frequencies . . . . .	6
2.3	Classical description of the optical properties of metals . . . . .	8
2.3.1	Drude-Sommerfeld model . . . . .	8
2.3.2	Lorentz-model . . . . .	9
2.4	Metals for plasmonic applications . . . . .	10
2.5	Surface plasmon polaritons . . . . .	11
2.6	Particle plasmons . . . . .	14
2.7	Optical nano-antennas . . . . .	15
2.7.1	Single particle antennas . . . . .	16
2.7.2	Dimer antennas . . . . .	18
2.8	Heat deposition in plasmonic structures . . . . .	21
<b>3</b>	<b>Numerical Simulations</b>	<b>23</b>
3.1	Finite difference time domain technique . . . . .	25
3.2	Transmission spectra . . . . .	28
3.2.1	Simulation geometry . . . . .	28
3.2.2	Results . . . . .	30
3.3	Near-field intensity distribution . . . . .	33
3.3.1	Simulation geometry . . . . .	33
3.3.2	Results . . . . .	34
3.4	Temperature distribution . . . . .	36
3.4.1	Simulation geometry . . . . .	37
3.4.2	Results . . . . .	38
3.5	Temperature evolution . . . . .	41
3.5.1	Model . . . . .	41
3.5.2	Results . . . . .	43
3.6	Antenna optimisation . . . . .	45

<b>4 Harmonic generation</b>	<b>51</b>
4.1 Light matter interaction with intense laser fields . . . . .	51
4.2 Surface harmonics . . . . .	52
4.3 High-order harmonic generation . . . . .	55
4.3.1 Semi-classical model . . . . .	56
4.3.2 Phase-matching conditions/macroscopic effects . . . . .	57
4.3.3 Phase-matching in the case of optical antennas . . . . .	60
4.3.4 Field inhomogeneities . . . . .	63
<b>5 Experiments</b>	<b>65</b>
5.1 Production techniques . . . . .	65
5.1.1 Electron beam lithography . . . . .	66
5.1.2 Focussed ion beam milling . . . . .	66
5.2 Nano-antenna characterisation . . . . .	69
5.2.1 Third harmonic generation . . . . .	71
5.2.2 Thermal stability . . . . .	76
5.3 Gas nozzle . . . . .	81
5.3.1 Characterisation . . . . .	81
5.3.2 Number of atoms at the sample . . . . .	83
5.4 Harmonic generation . . . . .	85
5.4.1 Low harmonic orders . . . . .	86
5.4.2 Higher harmonic orders and fluorescence . . . . .	87
5.4.3 Beam profile measurements . . . . .	93
<b>6 Summary and Outlook</b>	<b>95</b>
<b>Bibliography</b>	<b>99</b>
<b>Publications</b>	<b>115</b>
<b>Curriculum Vitae</b>	<b>117</b>







# CHAPTER 1

---

## Introduction

---

As early as Roman times people were fascinated by materials which change their colour depending on whether they are illuminated from one side or the other. The most famous example is probably the Lycurgus cup shown in figure 1.1. The origin of this behaviour lies in a plasmonic resonance of the gold nano-particles embedded in the ruby glass. Today, these materials are known as metamaterials [Leo07] with a broad range of applications. For example materials with a negative index of refraction have been fabricated [Sha07] or optical cloaking was demonstrated [Cai07].

Although plasmons are known for a long time [Kre68], the field has rapidly developed throughout the last decade and a broad range of applications has emerged particularly for extreme light concentration [Sch10b]. For instance, nano-particles can be used to locally heat biological tissue, which has already found applications in novel methods of cancer therapy [Hir03]. There, nano-particles are used to specifically destroy cancer cells without affecting the surrounding cells as in conventional approaches. Additionally, plasmons and nano-antennas in particular are a tool in non-linear optics facilitating, for example, enhanced second harmonic generation from non-linear media [Fan06]. Recent theoretical calculations even suggest the generation of isolated attosecond pulses, employing the



**Fig. 1.1:** Lycurgus cup. Image taken from [Leo07].

nano-plasmonic field enhancement in ellipsoidal antennas [Ste11]. Moreover, numerical simulations reveal the feasibility of attosecond plasmonic streaking [Sko11].

This bridges the gap to a different rapidly growing field – namely high-order harmonic generation (HHG) in noble gases. The process was first observed roughly twenty years ago [Fer88; McP87] and has since then provided a coherent light source in the extreme ultraviolet spectral range. Due to the shorter wavelength, the pulse durations achieved have been pushed from the femtosecond into the attosecond regime [Dre01]. Today, light pulses as short as 80 as are routinely generated [Gou08] and a whole new field of physics has been opened up [Kra09]. This unprecedented temporal resolution enables, among other things, new measurements in fundamental physics to study electron dynamics in molecules.

In parallel to this development, high-precision spectroscopy was also greatly improved by the frequency comb technique, which is now commonly used [Ude02]. However, its extension to the ultraviolet regime is challenging due to the low conversion efficiency of the HHG-process. To circumvent this issue and to increase the harmonic photon flux, external enhancement cavities have been developed and investigated extensively [Goh05; Jon05; Oza08; Yos09]. One intriguing application of a frequency comb in the vacuum-ultraviolet range is the possibility of performing direct frequency comb spectroscopy [Cin12; Mar04; Wit05; Zin06] in this spectral range.

Recently, the first frequency comb measurement on helium in the extreme ultraviolet regime has been reported with an improved accuracy of nearly one order of magnitude. Thus, new tests of quantum electrodynamics calculations as well as upper bounds on the drift of fundamental constants are envisaged [Kan10]. Additionally, nuclear transitions are also located in this spectral range. For instance Th-229 has a transition at 7.8 eV [Bec07], which could be probed with the fifth harmonic of a Ti:sapphire laser [Pei03]. A successful measurement would be the first ever spectroscopy of a nuclear transition with a laser system.

In summary, there is tremendous interest among physicists to establish a frequency comb in the ultraviolet regime. By employing a plasmonic resonance in optical nano-antennas, a different approach for HHG directly from a laser oscillator is envisaged [Kim08]. A successful implementation of this novel scheme would furthermore bridge the gap between two different fields of physics: plasmonics with typically low pulse energies and structure dimensions in the nanometre regime on one hand and high-field physics with peak intensities in excess of  $10^{14} \text{ W cm}^{-2}$  on the other.

## Goal and structure of the thesis

Within this thesis nano-antennas are analysed both theoretically and experimentally with respect to their applicability for high-order harmonic generation. Numerical simulations provide a tool to determine crucial antenna parameters for HHG. Here, particular emphasis is put on the thermal properties of the antennas to assess possible damage processes which are likely to occur for high incident intensities. Finally, the antennas are optimised to facilitate a maximised field enhancement without being thermally destroyed. The obtained results are experimentally verified and measurements on nano-antenna-assisted HHG are performed. During the experiments, great care has been taken to fully understand all experimental parameters and rigorously characterise the used components.

The thesis is organised in four parts. Chapter 2 introduces the theoretical background of plasmons and nano-antennas. Afterwards the numerical simulations and their results are described in chapter 3, followed by a brief review of optical harmonic generation in chapter 4. Finally, the experiments and the respective results are outlined in chapter 5. Chapter 6 summarises the present work and gives an outlook on future prospects.



# CHAPTER 2

---

## Optical antennas and plasmons

---

The following chapter introduces the basic concepts used within the thesis. It starts with a cursory review of classical antennas and their scalability to optical frequencies, followed by a brief introduction of Maxwell's equations in matter in this frequency range. Afterwards two classical models which describe the optical properties of metals are explained and analysed with a particular emphasis on plasmonic devices. The metal properties play an important role in the oscillations of conduction electrons, whose quanta are called plasmons. Various types of plasmons exist and their unique features are introduced by examining surface plasmon polaritons (SPPs) in more detail followed by particle plasmons (PPs). Both form the basis for a thorough understanding of optical antennas, which itself are a key element for the experiments performed within this thesis. Finally, heat deposition in plasmonic structures is analysed to assess possible destruction processes at high incident intensities.

### 2.1 Classical antennas and scalability to optical frequencies

For radio frequencies, simple dipole antennas are known from textbooks and are widely used for various applications. A standing wave is formed within the antenna and the antenna length is chosen as  $\lambda/2$  to work at resonance. These antennas are therefore also known as half-wave dipole antennas. However, in practice radiation at the antenna ends leads to a damping and the resonance is shifted to lower frequencies. This effect is compensated for by shortening the antenna length to approximately  $0.95 \times \lambda/2$  [Mil05].

In order to tune an antenna to be resonant at optical frequencies the antenna length has to be in the order of 100 nm. Thus, it is challenging to manufacture optical antennas. Moreover, at optical frequencies metals no longer behave as perfect conductors since the conductive electrons have an effective mass, which results in a phase lag between the electrons and the oscillating electromagnetic field. Despite these challenges, optical antennas have been produced recently [Müh05] and their properties are explained in more detail in section 2.7. As a basis, Maxwell's equations in matter at optical frequencies are described briefly below.

## 2.2 Maxwell's equations in matter at optical frequencies

The propagation of light in solid materials is described by the macroscopic Maxwell's equations which are for example found in [Jac98] and have the following form in SI-units:

$$\begin{aligned}
 \nabla \cdot \mathbf{D} &= \rho_{\text{ext}} \\
 \nabla \cdot \mathbf{B} &= 0 \\
 \nabla \times \mathbf{H} &= j_{\text{ext}} + \frac{\partial}{\partial t} \mathbf{D} \\
 \nabla \times \mathbf{E} &= -\frac{\partial}{\partial t} \mathbf{B} .
 \end{aligned} \tag{2.1}$$

Here,  $\mathbf{E}$  denotes the external electric field, which induces electric dipoles in matter and leads to a local polarisation  $\mathbf{P}$ . The same is true for external magnetic fields  $\mathbf{B}$ , resulting in a local magnetisation  $\mathbf{M}$ . Hence, two new vector fields, the displacement  $\mathbf{D}$ , and the magnetic field intensity  $\mathbf{H}$  further link the macroscopic fields via the material equations

$$\mathbf{D} = \varepsilon_0 \mathbf{E} + \mathbf{P} \quad \text{and} \tag{2.2}$$

$$\mathbf{H} = \frac{1}{\mu_0} \mathbf{B} - \mathbf{M} , \tag{2.3}$$

where  $\mu_0 = 4\pi \cdot 10^{-7} \text{ N/A}^2$  denotes the permeability and  $\varepsilon_0 = 8.854 \cdot 10^{-12} \text{ F/m}$  the permittivity of free space respectively. The external charge density  $\rho_{\text{ext}}$  is the source of the displacement and the current density  $j_{\text{ext}}$  likewise for the magnetic field intensity.

Furthermore, via the constitutive relations

$$\begin{aligned} j_{\text{ext}} &= \sigma \mathbf{E} \ , \\ \mathbf{M} &= \chi_{\text{M}} \mathbf{H} \ , \\ \mathbf{P} &= \varepsilon_0 \chi_{\text{E}} \mathbf{E} \ , \end{aligned} \tag{2.4}$$

the material response is related to phenomenological quantities, i.e. the conductivity  $\sigma$  and the magnetic and electric susceptibilities  $\chi_{\text{M,E}}$ , respectively. In equation (2.4) a linear response to the external field and a homogeneous and isotropic medium are assumed. By using the given relations, the displacement and the magnetic field can be written more conveniently as

$$\mathbf{D} = \varepsilon_0 (1 + \chi_{\text{E}}) \mathbf{E} = \varepsilon_0 \varepsilon \mathbf{E} \quad \text{and} \tag{2.5}$$

$$\mathbf{B} = \mu_0 (1 + \chi_{\text{M}}) \mathbf{H} = \mu_0 \mu \mathbf{H} \ . \tag{2.6}$$

In this work, only non-magnetic solids are used for which  $\chi_{\text{M}} = 0$  and hence  $\mu = 1$ .

However,  $\chi_{\text{E}}$  is non-zero and the permittivity  $\varepsilon$  is generally frequency dependent. To account for dissipation effects at optical frequencies,  $\varepsilon(\omega)$  is a complex quantity written as  $\varepsilon(\omega) = \varepsilon_1(\omega) + i\varepsilon_2(\omega)$ . The complex dielectric function is connected to the index of refraction  $n$  and the absorption coefficient  $\kappa$  by the Maxwell relation  $\varepsilon = (n + i\kappa)^2$  and hence

$$\varepsilon_1(\omega) = n(\omega)^2 - \kappa(\omega)^2 \tag{2.7}$$

$$\varepsilon_2(\omega) = 2n(\omega)\kappa(\omega) \ . \tag{2.8}$$

The values of  $n$  and  $\kappa$  are parameters which have to be determined experimentally by ellipsometry measurements [Tom05] and are tabulated for instance in [Joh72] or [Pal98]. The parameters of noble metals like gold or silver are of special interest for plasmonic experiments. Although the value of the dielectric function is calculated correctly for different photon energies, no physical explanation for this dependence is obtained. However, classical models based on the Drude-Lorentz model describe the observed effects accurately and give further insight [Mai07]. They are introduced in the following chapter to describe the optical properties of metals.

## 2.3 Classical description of the optical properties of metals

The dielectric function of metals and semiconductors depends on the photon energy as pointed out previously. Solid-state theory gives a detailed understanding and provides methods to calculate these material properties. Here, a Drude-Sommerfeld model and a Lorentz oscillator model are introduced.

### 2.3.1 Drude-Sommerfeld model

The optical properties of metals can already be explained for a wide range of frequencies by a simple plasma model in which a gas of free electrons of number density  $n$  moves relative to a background of positively charged metal ions, and band structure details are considered via an effective mass  $m$  for each electron. An external electric field results in an electron oscillation which is damped by collisions, occurring at a rate  $\gamma = 1/\tau$  with the relaxation time  $\tau$  of the free electron gas. This leads to a dielectric function given by

$$\varepsilon_{\text{Drude}}(\omega) = 1 - \frac{\omega_p^2}{\omega^2 + i\gamma\omega} , \quad (2.9)$$

with the plasma frequency  $\omega_p = \sqrt{ne^2/\varepsilon_0 m_e}$ , which is approximately  $13.8 \cdot 10^{15} \text{ s}^{-1}$  for gold. The real and imaginary parts of the dielectric function are

$$\begin{aligned} \varepsilon_1(\omega) = \text{Re}(\varepsilon(\omega)) &= 1 - \frac{\omega_p^2 \tau^2}{\omega^2 \tau^2} \\ \varepsilon_2(\omega) = \text{Im}(\varepsilon(\omega)) &= \frac{\omega_p^2 \tau}{\omega(1 + \omega^2 \tau^2)} . \end{aligned} \quad (2.10)$$

In figure 2.1 experimental data for gold is compared with the Drude-Sommerfeld model. Despite the simplicity of the model, it does reproduce major aspects of metals for wavelengths between 650 nm and 1.2  $\mu\text{m}$ . For instance in the optical frequency regime, the real part of the dielectric function is negative, such that the conduction electrons do not oscillate in phase with the applied external field. Moreover, the imaginary part is significant, which accounts for dispersion. Nonetheless, for example interband transitions are not considered, which for gold become apparent for wavelengths shorter than 650 nm as depicted in figure 2.1. This limits the applicability of the model.



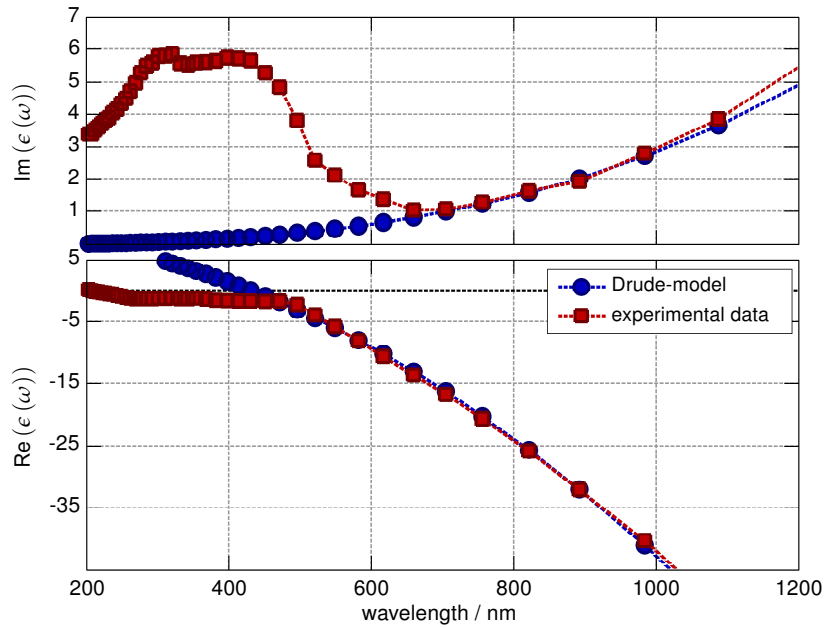


**Figure 2.1:** Comparison of experimental data for gold from [Joh72] with the Drude-Sommerfeld model. Already in the visible range the model starts to deviate from experimental data and around 400 nm interband transitions become significant illustrating the model's limits.

### 2.3.2 Lorentz-model

As already mentioned beforehand, the Drude-Sommerfeld model only describes the dielectric function correctly for photon energies below the threshold at which transitions between electronic bands can occur.

Interband transitions are caused by high-energy photons promoting electrons from lower-lying bands into the conduction band and can classically be described by a collection of damped harmonic oscillators  $j$  with resonance frequency  $\omega_j$ . This results in a contribution to the dielectric function of the form

$$\varepsilon_{\text{Lorentz}}(\omega) = 1 + \frac{\tilde{\omega}_p^2}{(\omega_j^2 - \omega^2)^2 - i\tilde{\gamma}\omega}, \quad (2.11)$$

with  $\tilde{\omega}_p = \sqrt{\tilde{n}e^2/\varepsilon_0 m}$  being the plasma frequency for the bound electrons of number density  $\tilde{n}$ , electron mass  $m$  and  $\tilde{\gamma}$  their respective damping constant. In practice, this leads to a maximum for  $\text{Im}(\varepsilon(\omega))$  near the resonance frequencies  $\omega_j$  and hence an increased Ohmic damping. By adding multiple Lorentz terms with the form of

equation (2.11) to the Drude-Sommerfeld model in equation (2.10), the dielectric function of metals can be accurately modelled [Mai07].

## 2.4 Metals for plasmonic applications

Various parameters have to be considered to determine an optimal metal for plasmonic applications and antennas in particular. First of all, Ohmic losses should be as low as possible to achieve low damping for electromagnetic waves. Ohmic absorption is proportional to  $\text{Im}(\varepsilon(\omega))$  and the losses occur close to the surface within the skin-depth  $\delta_{\text{skin}}$  which is given by

$$\delta_{\text{skin}} = \frac{c\sqrt{|\text{Re}(\varepsilon(\omega))|}}{\omega\text{Im}(\varepsilon(\omega))} \quad (2.12)$$

[Mai07]. According to equation (2.12) losses are kept low by choosing a metal with a large real part of the dielectric function to increase the reflectivity. Alternatively, since the imaginary part of the dielectric function accounts for Ohmic damping, a material with a low  $\text{Im}(\varepsilon(\omega))$  will have intrinsically low Ohmic losses in agreement with equation (2.12). Such a material is generally better suited for plasmonic applications because the occurrence of plasmon resonances strongly depends on  $\text{Im}(\varepsilon(\omega))$ , as will be explained in detail in section 2.7.1.

For comparison, the dielectric functions for a number of metals are shown in figure 2.2. Copper and gold have similar dielectric functions, which are governed by a Drude-Sommerfeld behaviour for wavelengths larger than 600 nm. In the green part of the visible spectrum interband transitions occur, resulting in an increased Ohmic damping. Nonetheless, both materials are well suited to build antennas for the red and near-infrared spectral region. In the case of silver, interband transitions become significant for wavelengths shorter than 400 nm, which makes it a better material for applications in the visible.

However, despite the dielectric function's spectral properties, the chemical stability also has to be taken into account for setting up experiments. Copper and silver for example quickly oxidise, so that experimental handling becomes cumbersome. Gold on the other hand combines both chemical stability as well as a favourable dielectric function in the red and near-infrared spectral region. It is therefore used for all experiments conducted within this thesis.

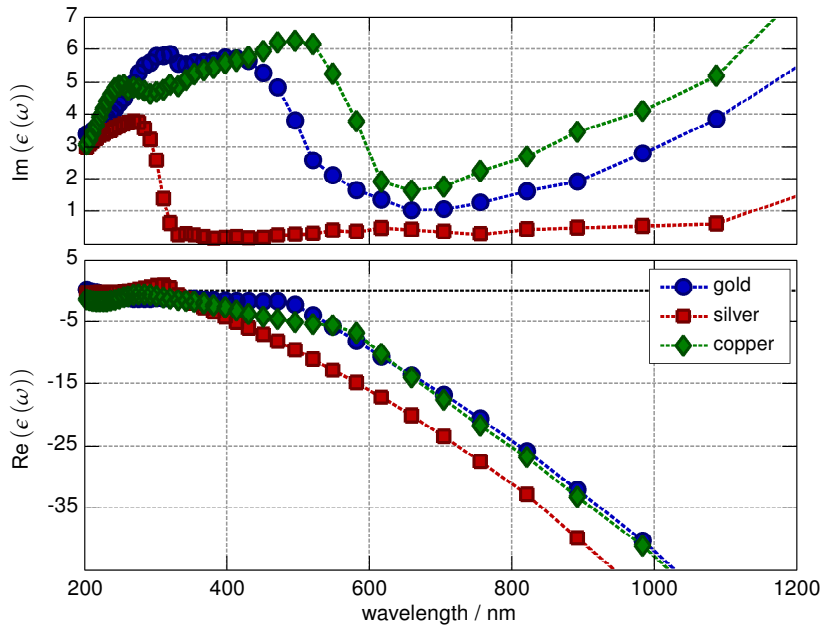


**Figure 2.2:** Dielectric functions for gold, silver and copper according to [Joh72].

## 2.5 Surface plasmon polaritons

Within metals, oscillations of the conduction electrons can occur. The quanta of these charge oscillations are called plasmons and have either longitudinal or transverse character. The longitudinal modes are represented by volume plasmons and can only be excited by particles and not by electromagnetic waves. Volume plasmons are thus not further considered since all described experiments within this thesis rely on a plasmon excitation with light.

The transverse mode, on the other hand, has a hybrid character of both an electromagnetic wave and a surface charge density and is also known as a surface plasmon polariton (SPP). To understand their properties, solutions to the wave equation with boundary conditions at a flat interface between a conductor and a non-absorbing dielectric, as illustrated in figure 2.3, are considered. Due to the transverse mode with a magnetic field in  $y$  direction, only electromagnetic waves with a polarisation parallel to the plane of incidence can couple to SPPs [Mai07; Sam91]. To generate the surface charge, an electric field normal to the surface is necessary, as is known from electrostatics. The hybrid character also leads to an evanescent field component, which is perpendicular to the surface and decays exponentially with distance away

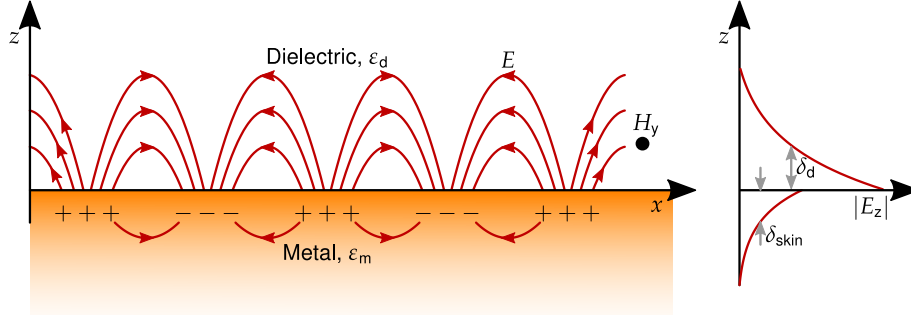


**Figure 2.3:** Surface plasmon polariton at a metal/dielectric interface: The electric field is normal to the surface to generate the surface charge. The interaction of surface charge and electric field leads to an evanescent field component  $E_z$  with a decay length  $\delta_d$  in the dielectric. Within the metal the decay length is given by the skin depth  $\delta_{\text{skin}}$  [Bar03].

from it. This is crucial because otherwise power would propagate away from the surface. Surface plasmons are therefore bound and non-radiative as sketched in the right part of figure 2.3.

The behaviour of SPPs is mainly governed by their dispersion relation, which is obtained from solving Maxwell's equations for transverse magnetic modes located at the interface between a metal and a dielectric

$$k_{\text{SPP}} = k_0 \sqrt{\frac{\varepsilon_d \varepsilon_m}{\varepsilon_d + \varepsilon_m}} \quad (2.13)$$

with a free space wave vector  $k_0 = \omega/c$ .  $\varepsilon_d$  and  $\varepsilon_m$  denote the complex dielectric functions of the dielectric and the metal, respectively. Figure 2.4 shows the dispersion relation for an ideal metal (red curve), real metal (green curve) and a free space photon (blue curve). Due to the interaction between surface charges and the electromagnetic field, the SPP's momentum  $\hbar k_{\text{SPP}}$  is usually larger than the free space momentum  $\hbar k_0$  of photons with the same frequency. This larger momentum is generally associated with the binding of the SPP to the surface [Bar03]. Furthermore, SPPs only exist if the involved dielectric functions,  $\varepsilon_d$  and  $\varepsilon_m$ , have opposite signs, which is the case for metals as described in section 2.3.1.

In order to couple light to a surface plasmon polariton, both the energy and the momentum have to be matched, i.e.  $\hbar\omega_{\text{photon}} = \hbar\omega_{\text{SPP}}$  and  $\hbar k_0 = \hbar k_{\text{SPP}}$ . In the frequency range where ideal Drude-Sommerfeld behaviour is observed, e.g. for an ideal metal or real metal in the infrared spectral range, no phase matching is possible. For real metals, on the other hand, damping i.e.  $\text{Im}(\varepsilon_m(\omega))$  lowers the surface plasmon

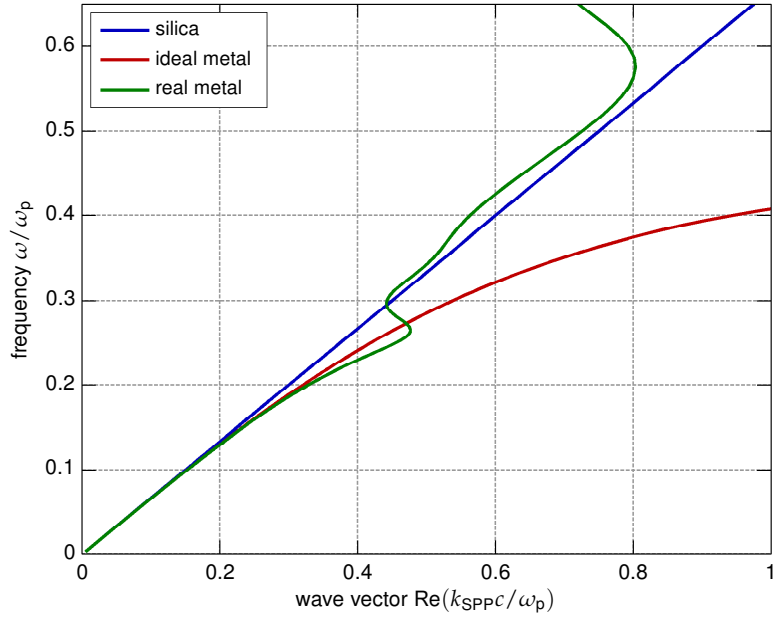


**Figure 2.4:** Dispersion relations of surface plasmon polaritons at the interface between an ideal metal (Drude metal), a real metal and silica. For an ideal metal light cannot couple to a surface plasmon polariton, because the momenta cannot be matched. For a real metal damping limits the SPP wave vector such that phase matching is possible.

polariton wave vector, which is therefore limited to a finite maximum value occurring at the surface plasmon frequency  $\omega_{\text{SP}}$ ,

$$\omega_{\text{SP}} = \frac{\omega_p}{\sqrt{1 + \varepsilon_d(\omega)}} \quad (2.14)$$

[Mai07]. Thus, phase matching is possible at a particular frequency. According to equation (2.13), this frequency depends on the dielectric functions of the involved materials at the interface, which inherently limits that approach.

Consequently, several other techniques to compensate for the momentum mismatch have been developed to couple light to a SPP. For example, a prism [Kre68; Ott68; Rae88] or a metallic grating structure [Rae88] can be used to enhance the momentum of the incident light.

Once a surface plasmon polariton has been excited, its propagation along the metal surface is of special interest for further applications like plasmonic waveguides or subwavelength optics [Dit02]. The propagation is characterised by the propagation length  $\delta_{\text{SPP}}$  which is limited by material damping. The imaginary part of the wave

vector from equation (2.13) determines  $\delta_{\text{SPP}}$  and evaluates to

$$\delta_{\text{SPP}} = \frac{c}{\omega} \sqrt{\left( \frac{\varepsilon_{1,m} + \varepsilon_d}{\varepsilon_{1,m} \varepsilon_d} \right)^3 \frac{\varepsilon_{1,m}^2}{\varepsilon_{2,m}}} . \quad (2.15)$$

Typical propagation distances for SPPs at a gold/silica interface in the visible to near-infrared spectral range are in the order of  $10 \mu\text{m}$  to  $30 \mu\text{m}$ . Plasmon based antennas for the visible spectral range are therefore feasible.

## 2.6 Particle plasmons

Since surface plasmon polaritons travel at an interface between a dielectric and a metal as explained in section 2.5, they are also excited in small metal nano-particles. To understand their plasmonic behaviour, a simple spherical particle with radius  $R$  and a dielectric constant  $\varepsilon$  embedded in an environment with  $\varepsilon_{\text{env}}$  is considered. Furthermore an incident electric field  $\mathbf{E}$  illuminates the sphere as sketched in figure 2.5. The response of the particle to the plane-wave illumination with wavelength  $\lambda$  is described by Mie theory and yields an induced dipole moment [Boh07]

$$\mu_p = 4\pi R^3 \varepsilon_0 \frac{\varepsilon - \varepsilon_{\text{env}}}{\varepsilon + 2\varepsilon_{\text{env}}} \mathbf{E} . \quad (2.16)$$

For very small particles where  $R \ll \lambda$ , the electric field can be considered constant over the particle, such that the phase is constant as well. In this so called quasistatic approximation, no retardation effects occur and hence it is justified to replace the dielectric constant  $\varepsilon$  in equation (2.16) by the dielectric function  $\varepsilon(\omega)$ .

Equation (2.16) already shows some major features of optical antennas, most strikingly a resonant enhancement, when  $|\varepsilon + 2\varepsilon_{\text{env}}|$  has a minimum, which simplifies for small

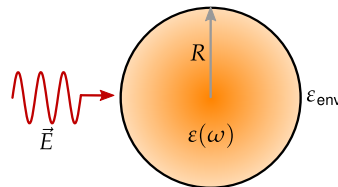


**Figure 2.5:** Spherical particle with dielectric function  $\varepsilon(\omega)$  illuminated by a plane wave with electric field  $\mathbf{E}$ , embedded in an environment with  $\varepsilon_{\text{env}}$ .

imaginary parts of the dielectric function to

$$\operatorname{Re}(\varepsilon(\omega)) = -2\varepsilon_{\text{env}} . \quad (2.17)$$

As shown in figure 2.2 for noble metals like gold and silver, this condition is met in the visible spectral range and for instance nicely illustrated by the Lycurgus cup (figure 1.1). On resonance the induced dipole moment is strongly increased but limited by the non-zero remaining imaginary part of the dielectric function. The electric field inside the sphere is given by

$$\mathbf{E}_{\text{sphere}} = \frac{3\varepsilon_{\text{env}}}{\varepsilon(\omega) + 2\varepsilon_{\text{env}}} \mathbf{E} , \quad (2.18)$$

which is also strongly increased at resonance. In contrast to surface plasmon polaritons, the plasmonic mode associated with the resonance does not propagate. Thus it is possible to excite the plasmonic resonance by direct light illumination, which is also referred to as a localised surface plasmon resonance (LSPR) or particle plasmon (PP) [Mai07].

Although spheroidal antennas give a first insight into plasmonic nano-antennas and their resonances, single-wire antennas are used more often and also form the basic building blocks for complex antenna designs. To understand their scaling behaviour for different aspect ratios, Mie theory is applicable too. However, little physical insight is gained with this description despite matching predictions of the occurring resonances. A Fabry-Pérot resonator model, on the other hand, describes the nature of the eigenmodes of plasmonic structures [Bar08; Val08].

## 2.7 Optical nano-antennas

For radio frequencies and in the microwave regime, antennas are widely used for various applications. In the visible spectral range however, the concept has only recently been introduced [Müh05]. This is partly due to the required antenna dimensions in the optical regime, which are in the order of hundreds of nanometers and therefore difficult to manufacture. To understand the behaviour of optical antennas, single particle antennas are explained first followed by dimer antennas.

### 2.7.1 Single particle antennas

#### Fabry-Pérot resonator model

Consider a metallic single-wire nano-antenna with a dielectric function  $\varepsilon(\omega)$  as a wave-guide for surface plasmon polaritons. As introduced in section 2.5, SPPs have a finite propagation length due to Ohmic damping as well as evanescently decaying near-fields. This decay in the transverse direction causes a shorter effective wavelength and hence a reduced propagation speed for the guided modes compared to light in vacuum [Nov94]. The reduced wavelength in turn strongly effects the design for optical antennas [Dor09; Nov07; Søn08], since an ideal classical single-wire antenna has its resonance of the  $n$ -th order at a length  $L = n\frac{\lambda}{2}$ . As pointed out in section 2.1, damping effects also affect the antenna length for classical antennas [Mil05]. At optical frequencies, however, they are much more pronounced than for radio frequencies.

Figure 2.6 shows a sketch of a typical rod-type antenna of length  $L$  and radius  $R$  with an incident electric field polarised along the long axis. The two wire ends act like mirrors and a one dimensional cavity is formed. During propagation along the antenna with the propagation constant  $\gamma$ , the SPP picks up a phase of  $\gamma L$  and suffers a phase jump  $\delta\phi$  upon reflection at the end [Bar08; Val08]. Resonances of the  $n$ -th order therefore occur for antenna lengths  $L(n)$ , where the total accumulated phase per round trip equals  $n$  times  $2\pi$

$$\gamma L(n) + \delta\phi = \pi n \quad . \quad (2.19)$$

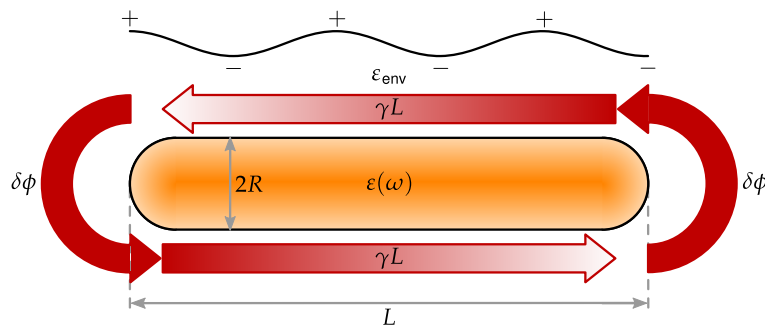


**Figure 2.6:** Single-wire antenna of length  $L$  and radius  $R$  made of a metal rod with dielectric function  $\varepsilon(\omega)$ . Incident light with wavelength  $\lambda$  polarises the ends resulting in a standing surface charge wave.  $\gamma$  is the propagation constant of the guided mode. At the end cap, a phase jump  $\delta\phi$  occurs, which is strongly dependent on the end cap geometry.



According to equation (2.19), the phase jump can also be interpreted as an apparent length increase  $\delta L = \delta\phi/\gamma$ , leading to shorter resonance lengths independent of resonance order  $n$ . At resonance, a standing surface charge wave builds up in the antenna, again exhibiting the LSPR nature already pointed out for spherical particles. In other words, one can also think of the plasmon resonance in optical antennas as a SPP first being launched, which then forms a particle plasmon (PP), i.e. it has a hybrid character.

Furthermore, equation (2.19) shows a linear relation between the resonance length  $L$  of the antenna and the plasmon wavelength  $\lambda_{\text{SPP}} = 2\pi/\gamma$ . For materials with a Drude-Sommerfeld behaviour, the plasmon wavelength is related to the wavelength of the incident light  $\lambda_0$  by

$$\lambda_{\text{SPP}} = n_1 + n_2\lambda_0 \quad , \quad (2.20)$$

with  $n_1$  and  $n_2$  only depending on the exact antenna geometry and the dielectric function of the metal [Nov07]. At frequencies where interband transitions become significant, deviations from equation (2.20) occur. Nonetheless, for typical optical antenna applications the antenna's resonance length  $L$  depends linearly on the incident wavelength  $\lambda_0$ . Thus, for an increasing antenna length the resonant wavelength shifts towards the near-infrared region.

So far an electric field polarised along the main antenna axis has been considered. For an orthogonally polarised incident field, exactly the same model holds. Due to the changed polarisation the charges oscillate along the short antenna axis. Thus the plasmonic resonance occurs spectrally separated towards the UV spectral range.

It should be noted, that the Fabry-Pérot resonator model does not explain the phase jump's origin. This is included in electromagnetic approaches based on the involved currents and fields in the single-wire antenna [Dor10; Tam11]. They confirm the results from the simpler picture presented here, though.

At resonance, single-wire antennas as well as spherical ones exhibit a strong local field enhancement. Figure 2.7 shows the normalised intensity enhancement  $|\mathbf{E}|^2$  around a single-wire antenna illuminated by a plane wave with  $\lambda = 800$  nm, which is polarised along the  $x$ -axis. The antenna is 100 nm long, 25 nm wide and 25 nm high. Each sub-figure shows a line-out along the solid and dashed line respectively. Due to the phase jump at the ends the antenna radiates significantly and the electric field extends

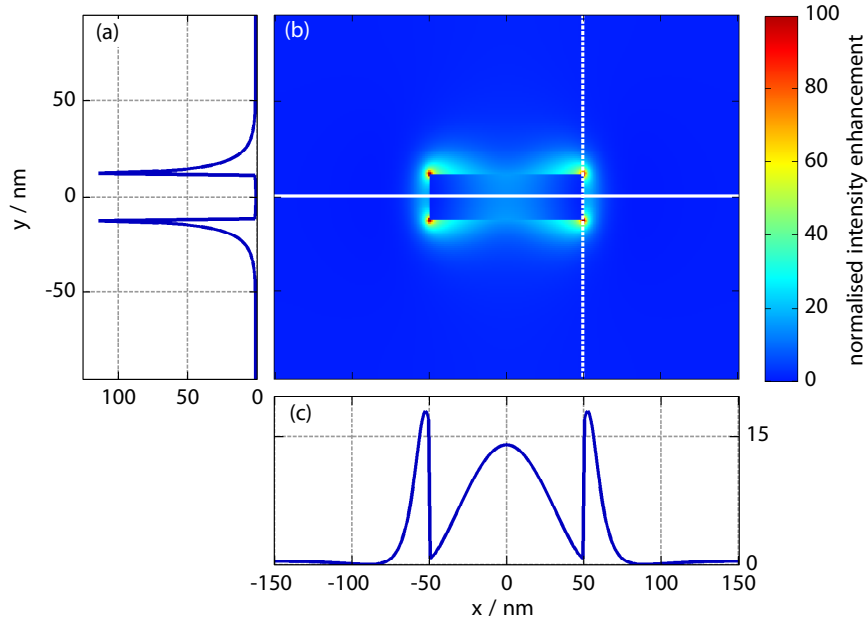


**Figure 2.7:** Electric field enhancement  $|\mathbf{E}|^2$  around a single-wire antenna illuminated by a plane wave with  $\lambda = 800$  nm, which is polarised along the  $x$ -axis. Sub-figure (a) shows a line-out in  $y$ -direction along the dashed line and (c) respectively in  $x$ -direction along the solid line. Significant enhancement is observed at the antenna ends due to the resonant excitation.

into the dielectric. This shows up as a strong local field enhancement with normalised enhancement factors of up to 115. Figure 2.7 has been calculated with the finite difference time domain method, which solves Maxwell's equations on a grid. The method as well as the simulation geometry for figure 2.7 is explained in detail in chapter 3.

### 2.7.2 Dimer antennas

Dimer antennas consist of two individual single particle antennas separated by a feed gap of width  $d$ . Depending on the interparticle distance  $d$  and the orientation of each antenna, the single particle resonances couple [Fun09; Mer08]. For resonant optical antennas, the end-to-end coupling is most important, leading to strongly enhanced and highly localised fields inside the gap. A typical design consisting of two single-wire antennas of length  $L$  with an incident electric field polarised along the main axis is sketched in figure 2.8.

The incident field excites a longitudinal mode, as described in section 2.7.1, within each antenna arm, leading to a surface charge density as depicted in figure 2.8. For large gap sizes no coupling between the modes is observed and each antenna arm acts as a separate single-wire antenna [Fun09]. This situation is shown in the middle of figure 2.9. For smaller gap sizes however, the near-fields interact with each other which is described by the plasmon hybridisation model [Nor04; Pro03].

Two different cases have to be considered: First, the resulting surface charge density from the LSPR can couple such that the two rods interact via an attractive coupling with alternating charges as shown in the bottom part of figure 2.9. Because of the interaction, the resonance energy is lowered such that a red-shift is observed in experiments [Rec03; Su03]. For spheres, the distance dependence on the frequency shift has been calculated to scale with  $d^{-3}$  [Nor04]. This was experimentally confirmed [Rec03] although exponential fits also approximate the data well [Su03]. In both cases, coupling only occurs for inter-particle distances up to 2.5 times the particle diameter. For experimental designs with more complex shapes, the resonance wavelength is determined by numerical simulations [Sun05], which are described in chapter 3.

The second coupling mode is an antibonding mode in which the surface charge density in each antenna is symmetric around the gap, leading to a repulsive interaction. Thus the resonance energy is increased and the plasmon resonance is slightly blue-shifted [Rec03]. To observe the antibonding mode strong coupling i.e. small gap sizes are necessary. Moreover, the mode is symmetry-forbidden for normally incident plane waves such that it is usually not excited in experiments and also known as a "dark" mode. Therefore, it has only recently been experimentally observed in a symmetric two-wire antenna with a slightly displaced focus with respect to the antenna [Hua10b].

As mentioned earlier, dimer antennas exhibit strong field localisation and enhancement

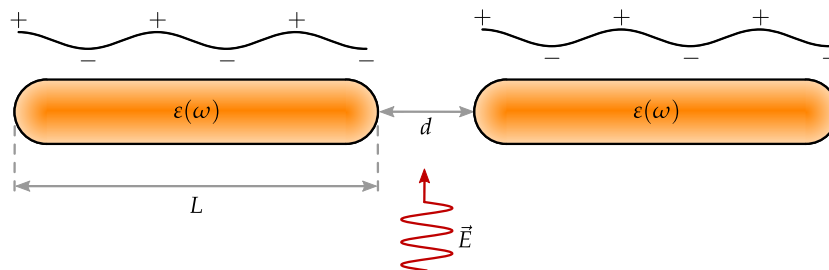


**Figure 2.8:** Two single wire antennas of length  $L$  separated by a distance  $d$ . The modes of each arm couple to a bonding mode, i.e. at each side of the gap opposite charges are present. Thus the resonance wavelength is red-shifted towards the near-infrared.

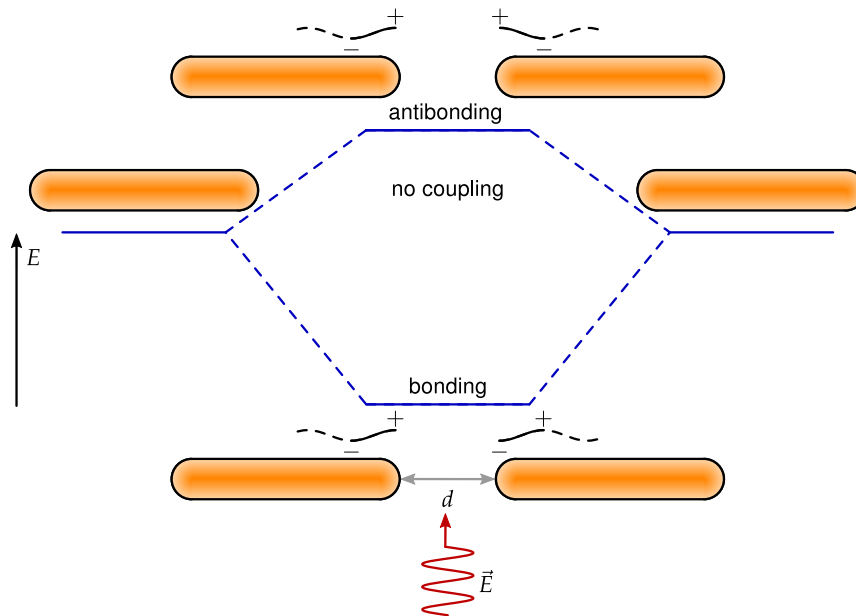


**Figure 2.9:** Two single-wire antenna modes couple depending on their separation  $d$ . The bonding mode is always present, the antibonding mode however can only be observed for distances smaller than 10 nm [Hua10b] and a broken system symmetry e.g. via asymmetric illumination.

in the feed gap. Figure 2.10 shows the normalised intensity enhancement  $|\mathbf{E}|^2$  around a dimer antenna illuminated by a plane wave with  $\lambda = 800$  nm, which is polarised along the  $x$ -axis. Each antenna arm is 75 nm long, 25 nm wide and 25 nm high, separated by a gap of 10 nm. The two sub-figures show line-outs along the solid and dashed line respectively. As for single-wire antennas, each arm radiates and the electric field extends into the dielectric. In the gap, the two near-fields of each arm overlap, leading to significant enhancement of the near-fields with enhancement factors of up to 450. Figure 2.10 has been calculated with the finite difference time domain method, like figure 2.7 before. A detailed explanation of the method and the used geometry is given in chapter 3.

In summary plasmon resonances in single particle antennas have been introduced and explained by a Fabry-Pérot resonator model. In dimer antennas these resonances couple and intensity enhancement factors of typically two orders of magnitude are found in the feed gap. Therefore optical antennas are well suited to reach intensities of  $10^{13} \text{ W cm}^{-2}$  when illuminated with a tightly focussed beam from a laser oscillator.

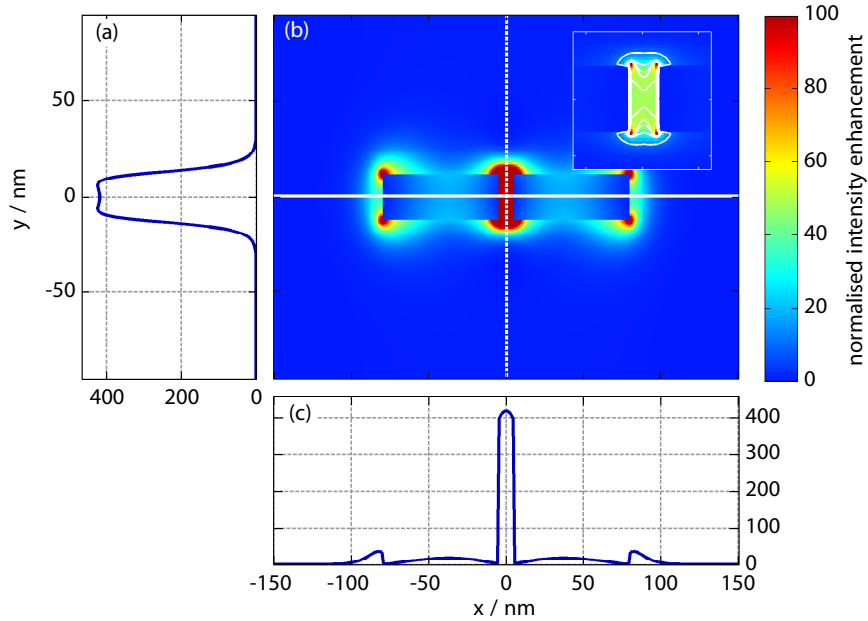


**Figure 2.10:** Electric field enhancement  $|\mathbf{E}|^2$  around a pair of two single-wire antennas illuminated by a plane wave with  $\lambda = 800$  nm. Sub-figures (a) and (c) show line-outs in  $y$ -direction along the dashed line and along the solid line, respectively. In the gap region enhancement factors of up to 450 are observed. On the outer edges of each single-wire antenna significant enhancement occurs, too. The inset shows a detailed plot of the gap region with a different colourmap.

## 2.8 Heat deposition in plasmonic structures

In the spectral range in which optical antennas operate, all metals have a non-zero imaginary part of the dielectric function. This dispersive behaviour leads to an absorption of the incident light and energy is deposited within the metal. Analysing the Poynting vector  $\mathbf{S} = \mathbf{E} \times \mathbf{H}$  and taking the electric polarisation into account allows to calculate the time-averaged dissipative electromagnetic energy [Lou70; Rup02].

For non-magnetic dispersive materials, like noble metals, the heat source density is given by

$$q = \frac{1}{2} \varepsilon_0 \omega \operatorname{Im}(\varepsilon(\omega)) |\mathbf{E}|^2, \quad (2.21)$$

and has a unit of  $\text{J m}^{-3}$ . Ultimately, the absorbed electromagnetic energy is converted

into heat in the metal. For a structure of volume  $V$  this leads to

$$Q = \int_V q \, dV . \quad (2.22)$$

Thus, by calculating the electric field inside e.g. an optical antenna the resulting temperature can be determined in two steps. First the absorbed energy leads to an initial temperature increase  $\Delta T$ . Subsequently the structure cools down due to heat diffusion into the surrounding medium. To obtain the resulting temperature after time  $t$  the diffusion equation

$$\rho C \frac{\partial T(\mathbf{r}, t)}{\partial t} + \kappa \nabla^2 T(\mathbf{r}, t) = -q(\mathbf{r}, t) \quad (2.23)$$

has to be solved, where  $\rho$  denotes the mass density,  $C$  the specific heat capacity and  $\kappa$  the thermal conductivity [Baf11]. Especially for applications with high intensities, the temperature evolution of the antenna is crucial, because reshaping due to melting can occur [Wan11], which is usually detrimental to the original design.

# CHAPTER 3

---

## Numerical Simulations

---

Plasmonic structures and optical antennas in particular feature among other things distinct resonances and a pronounced electric field enhancement which have been introduced in the previous chapter. Only for rather basic structures, resonance frequencies, electric field distributions or the electric field enhancement can be calculated analytically. Thus, numerical simulations offer a tool to investigate and optimise for instance optical antennas for different applications. Consequently, various numerical techniques have been developed over the past decades to simulate electromagnetic fields in metallic structures. However, plasmonic devices are particularly challenging for all available techniques because of the rapidly decaying near fields at the metal-dielectric interface. Therefore, to resolve these fields a very high spatial resolution is necessary. Consequently, the applied method has to be maximally efficient to be computationally feasible.

In the discrete dipole approximation, the investigated structure is divided into a finite array of polarisable points. In response to an applied external field, each point then gains a dipole moment and the resulting electric field is determined by summing up the individual dipole fields [Dra94]. This calculation is performed in the frequency domain, leading to two major consequences; firstly, it is easy to take material dispersion into account because  $\varepsilon(\omega)$  can be used directly from experiments. Unfortunately, only a limited number of frequencies can be considered due to the computational effort, which prohibits the application to broadband pulses. Secondly, the discrete dipole approximation can only be used to model structures embedded in uniform media, because it is based on the field of a dipole in a homogeneous medium [Bro07].

The latter drawback is overcome by a finite difference frequency domain method, where derivatives in Maxwell's equations are substituted by finite differences. The structure is again modelled by a discrete grid on which the field quantities are determined by solving the differential Maxwell equations directly [Jin02]. While this is a more general approach and no assumptions about the field have to be made, additional complexity is added. Due to discretisation, artificial wave reflections occur at the boundary of the finite computational domain, which have to be dealt with by introducing absorbing boundary conditions [Taf05]. Nonetheless, the technique can be used to model arbitrary plasmonic devices. The inability to simulate broadband pulses, however, remains a weakness. In the time domain pulses are described easily, though. Thus a finite difference time domain (FDTD) method has been developed over the last decades [Taf05; Taf80; Yee66], which is widely used to simulate optical antennas [Cro03; Cub08; Sun05] and other plasmonic devices [Ver08]. Consequently, the FDTD method in three dimensions is also applied within this thesis to assess the response of nano-antennas to ultrashort laser pulses. Below, the method as well as the simulation geometries employed here are explained in more detail.

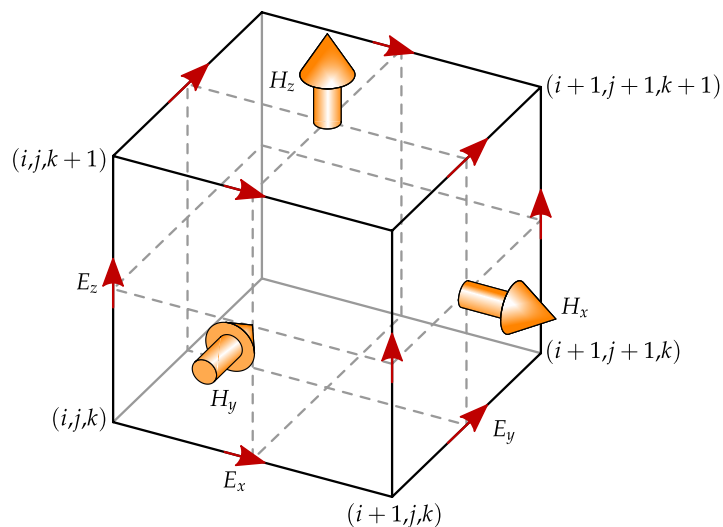


**Figure 3.1:** Yee-lattice for the FDTD method. Magnetic field vectors are located at the face centres, whereas electric field vectors are determined at the edges. The arrangement implicitly satisfies both Gauss's laws and therefore simplifies the calculation of electric and magnetic fields.



### 3.1 Finite difference time domain technique

In the FDTD method, the whole simulation volume is discretised into small finite unit cells of width  $\Delta x$ , depth  $\Delta y$  and height  $\Delta z$  depicted in figure 3.1. Thus, a point in space is denoted by

$$(i, j, k) \hat{=} (i\Delta x, j\Delta y, k\Delta z) . \quad (3.1)$$

Analogously, time is also discretised with a time increment  $\Delta t$ , such that  $t = n\Delta t$ . A function  $U$  is furthermore denoted as

$$U(i\Delta x, j\Delta y, k\Delta z, n\Delta t) \hat{=} U_{i,j,k}^n . \quad (3.2)$$

Electric and magnetic field vectors are shifted relative to one another both in space and time such that electric fields are determined at the edges and have integral indices  $i, j, k, n$  whereas magnetic fields are located at the cube's face centre and have half-integer indices. This particular arrangement is also known as the Yee-cell [Yee66]. Because of the chosen grid, both of Gauss's laws are implicitly satisfied and don't have to be enforced. Thus from Maxwell's equations (2.1) only the two coupled time-dependent curl equations remain. There, all spatial derivatives of a quantity  $U$  are substituted by finite differences of the following form

$$\frac{\partial U}{\partial x}(i\Delta x, j\Delta y, k\Delta z, n\Delta t) = \frac{U_{i+1/2,j,k}^n - U_{i-1/2,j,k}^n}{\Delta x} + \mathcal{O}((\Delta x)^2) . \quad (3.3)$$

The spatial shift by  $\Delta x/2$  on the right hand side of equation (3.3) is beneficial for solving Maxwell's equations as will be explained below. In analogy to the spatial shift between electric and magnetic fields, there is also a shift in time according to a leapfrog arrangement. For a particular time step, all electric field calculations are carried out and stored with previously obtained magnetic field data. With this data, the magnetic fields for the next time step are determined to restart the cycle until time stepping is concluded. Temporal derivatives of a quantity  $U$  are therefore expressed as

$$\frac{\partial U}{\partial t}(i\Delta x, j\Delta y, k\Delta z, n\Delta t) = \frac{U_{i,j,k}^{n+1/2} - U_{i,j,k}^{n-1/2}}{\Delta t} + \mathcal{O}((\Delta t)^2) . \quad (3.4)$$

The combination of equation (3.3) and equation (3.4) leads to a set of finite difference equations for the magnetic and the electric field [Taf05; Yee66]. In these equations the temporal derivative of the electric field only depends on the spatial derivative of the magnetic field and vice versa. As a consequence the shifted lattices greatly simplify the calculation. Let  $f$  be a function to calculate the respective field components. The above outlined scheme is thus summarised to

$$\begin{aligned} H^{n+1/2} &= f(H^{n-1/2}, E^n) \\ E^{n+1} &= f(H^{n+1/2}, E^n) \end{aligned} \quad (3.5)$$

In their original form, the finite difference equations only considered isotropic and non-dispersive media. Hence, extensions to them have to be made to describe e.g. gold and its dispersive character. Since all calculations are carried out in the time domain, the dielectric function has to be modelled as described in sections 2.3.1 and 2.3.2 and transferred from the frequency domain. Various algorithms have been developed for the transformation [Jos91; Kas90; Lue90; Sul92; You01], which are all based on the same underlying principle. The general idea is explained below:

Assume the respective field components are again determined via a function  $f$ . As the magnetic field is not subject to dispersion and thus obtained equivalently to the previous case, it is

$$H^{n+1/2} = f(H^{n-1/2}, E^n) \quad (3.6)$$

Next, the displacement is calculated by incorporating a Fourier-transformed analytic expression of the dielectric function  $\varepsilon(\omega)$ :

$$D^{n+1} = f(D^n, H^{n+1/2}) \quad (3.7)$$

From these two expressions, the resulting electric field is finally obtained, leading to the following calculation scheme:

$$\begin{aligned} H^{n+1/2} &= f(H^{n-1/2}, E^n) \\ D^{n+1} &= f(D^n, H^{n+1/2}) \\ E^{n+1} &= f(E^n, E^{n-1}, D^{n+1}, D^n, D^{n-1}) \end{aligned} \quad (3.8)$$

Comparing equation (3.5) with equation (3.8) clearly shows the increased effort to

simulate dispersive materials both in terms of memory and simulation run time. Nonetheless, the extensions greatly expand the FDTD technique.

A common problem in all finite difference techniques is the occurrence of artificial wave reflections at the cell boundaries as introduced earlier. They arise from both the space discretisation and the finite simulation cell size and are avoided by using appropriate boundary conditions. The most simple condition ensures a reflectionless boundary by simply forcing the fields to zero. This mimics a perfect metal surrounding with zero absorption and zero skin depth and is thus termed a metallic wall boundary condition. However, it is only seldom applicable due to the severe constraints for the fields. A practically more relevant approach makes use of the system's periodicity. Assuming a cell size  $L$ , each field component satisfies

$$f(x + L) = f(x) , \quad (3.9)$$

which is also known as a Bloch periodic boundary condition.

To simulate open boundaries e.g. isolated single antennas, a different method is needed, absorbing all incident waves without any reflections. This is achieved by a perfectly matched layer (PML), which actually is not a boundary condition, but a special absorbing material placed adjacent to the boundary [Ber94]. The material is designed with magnetic and electric conductivities, matching those of the surrounding medium such that it is theoretically non-reflecting for any wavelength and incidence angle. Discretisation, however, causes imperfections and leads to a small residual reflection. These are compensated for by giving the PML a finite thickness and turning the conductivities gradually on over the thickness. Since a PML is absorbing, it can affect evanescent modes lying in close proximity by extracting energy from the system. Therefore a sufficiently large computational cell has to be chosen to avoid a perturbation of the results [Taf05].

So far, the general calculation scheme as well as an incorporation of dispersive media and suitable boundary conditions have been introduced. A plane wave source to simulate, for example, optical antennas is still missing, though. Originally this was implemented by specifying the incident wave as an initial condition for each electric and magnetic field component within the simulation cell [Yee66]. However, this approach only works for non-dispersive materials and is thus not applicable for simulations of plasmonic devices [Taf05]. Instead of defining the electric field

directly, an oscillating current amplitude is placed at the desired position [Wag98]. Unfortunately, the resulting electric field cannot be set directly with a current source due to the surrounding medium. Within a perfect electric conductor for example, the electric field from a current source will be zero. Therefore two calculations have to be performed to normalise the results from the structure under investigation to those from a reference run.

All FDTD calculations within this thesis were carried out with an open source implementation of the FDTD algorithm developed at the Massachusetts Institute of Technology termed MIT Electromagnetic Equation Propagation (MEEP) [Osk10]. The simulation geometries used to determine, for instance, near-field intensity enhancement factors are explained in detail below.

## 3.2 Transmission spectra

### 3.2.1 Simulation geometry

According to section 2.7.2, coupled optical antennas exhibit a strong local field enhancement within the feed gap when illuminated at their resonance frequency. For complex antenna geometries this frequency is determined by FDTD simulations.

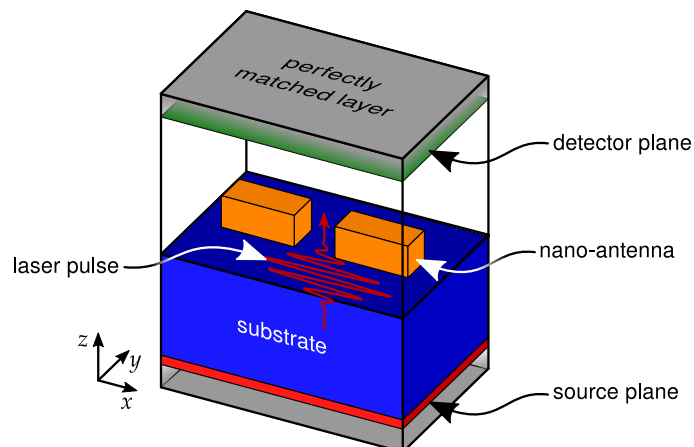


**Figure 3.2:** Simulation geometry to calculate transmission spectra. The polarisation of the incident laser pulse is aligned along the principal antenna axis. PMLs in positive and negative  $z$ -direction avoid spurious reflections from the simulation cell's boundary. In  $x$ - and  $y$ -direction Bloch periodic boundary conditions are used to model an antenna array. The antenna itself is placed on top of a substrate, which covers the bottom half of the simulation cell.

Figure 3.2 sketches the exemplary rod-type geometry used for those calculations. The simulation cell's bottom half is filled by a substrate material, which dielectric function is described by the index of refraction at the centre wavelength of the incident pulse via the Maxwell relation  $\varepsilon = n^2$ . The gold antenna itself is centred in the  $xy$ -plane and lies on top of the substrate. The dielectric function of gold is modelled with a Drude-Lorentz model, incorporating a sum of Lorentz terms to accurately represent interband transitions as described in section 2.3.2. The parameters needed to represent and match the experimental values of the dielectric function are taken from [Rak98]. Figure 3.3 shows a comparison between experimental data for gold [Joh72] and the dielectric function used in the simulation. Qualitatively the model reproduces the experimental data with the distinctive interband transitions. Quantitatively, however, differences are apparent; In the Drude-Sommerfeld regime damping is overestimated whereas the strength of interband transitions is underestimated. Despite these differences, a good agreement between experiments and simulations of plasmonic devices has been found [Via05]. A detrimental influence on the simulation results is therefore not expected from the small deviations.

In  $x$ - and  $y$ -direction Bloch periodic boundary conditions model an antenna array

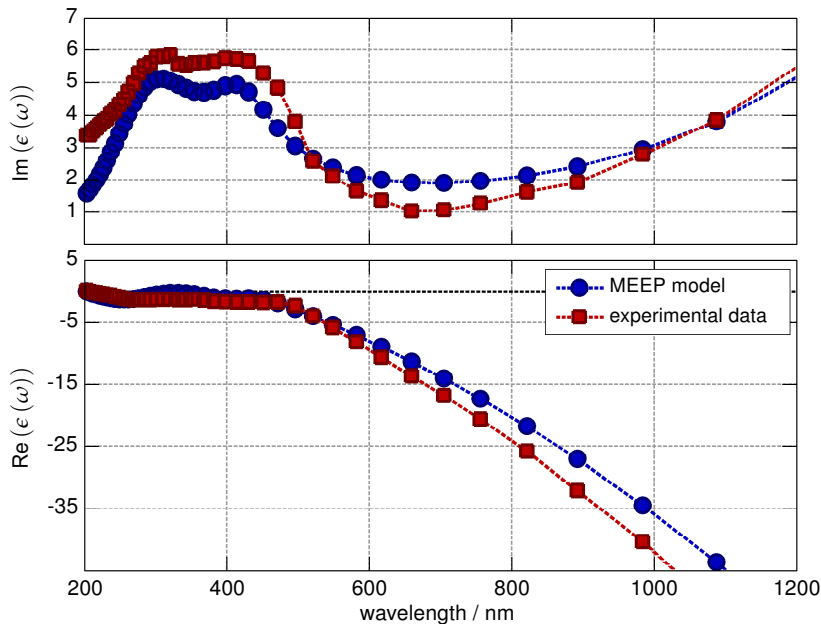


**Figure 3.3:** Dielectric function of gold in MEEP. The parameters to model the dielectric function are taken from [Rak98] and experimental data originates from [Joh72].

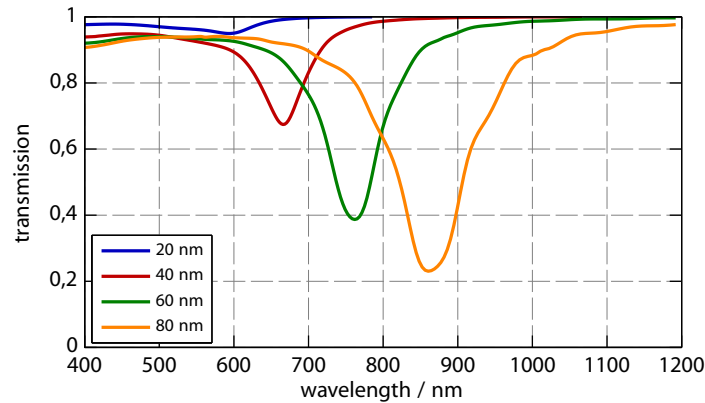
and the respective cell dimensions match those from conducted experiments to allow a direct comparison. The structures are illuminated from the substrate side by a broadband Gaussian-like excitation pulse with a spectral Gaussian width spanning from 400 nm to 1200 nm and its polarisation aligned along the principal antenna axis. The source is implemented with a current source covering the whole  $xy$ -plane to achieve plane wave illumination. Since waves are emitted both in positive and negative  $z$ -direction, a perfectly matched layer is placed at the simulation cell's bottom and top to avoid numerical reflections. Moreover, the source plane lies on top of the bottom PML to immediately absorb the wave travelling in negative  $z$ -direction by coupling directly into the PML. Otherwise spurious residual reflections from the PML could perturb the calculation.

The antenna's response to the excitation pulse is measured in the detection plane placed 10 nm below the top PML. A frequency resolved transmission curve within the excitation bandwidth is obtained by calculating the flux of the Fourier-transformed electric field going through the plane. As a reference calculation the same principal geometry without the antenna is used, leading to a relative transmission curve depicted in figure 3.4(a). From this curve the resonance wavelength is determined.

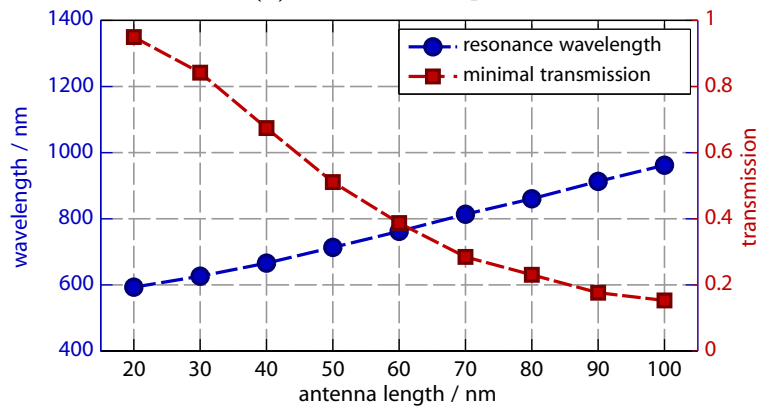
### 3.2.2 Results

Figure 3.4 shows transmission spectra and derived quantities for rod-type optical antennas with different antenna arm lengths  $L$ . It was varied from 20 nm up to 100 nm to find a resonant design for experimentally available laser pulses at 800 nm with pulse durations of  $<10$  fs, i.e. spectral bandwidths of approximately 300 nm. The feed gap as well as the antenna height and width are kept constant at 20 nm and 24 nm respectively. In figure 3.4(a) representative transmission curves are shown, illustrating previously introduced properties. As described in section 2.7 a longer antenna arm length leads to a significant red-shift e.g. a 20 nm antenna being resonant at 593 nm and a 80 nm antenna at 860 nm, respectively. Both the resonance wavelength  $\lambda_{\text{res}}$  as well as the minimal transmission are plotted as a function of the antenna arm length  $L$  in figure 3.4(b). For short antenna lengths e.g. 20 nm, the resonance is barely visible in the spectra. However, for larger ones, a pronounced dip is observed with a significantly lower transmission of just 0.15 %.

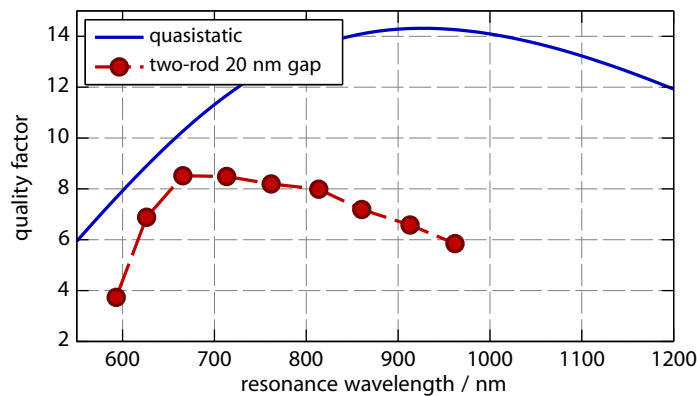
The resonance wavelength on the other hand, exhibits a linear scaling behaviour in the



(a) Transmission spectra.



(b) Resonance wavelength and minimal transmission, extracted from transmission spectra above. Dashed lines serve as a guide to the eye.



(c) Quality factor derived from transmission spectra above. Dashed lines serve as a guide to the eye.

**Figure 3.4:** Transmission spectra for rod-type optical antennas with a length  $L$  at a fixed feed gap of 20 nm. The antennas are illuminated from the substrate side with broadband pulses covering a spectral range from 400 nm to 1200 nm. Their polarisation is parallel to the principal antenna axis.

near-infrared spectral range, which is expected from equation (2.20). Towards the blue, deviations from linearity occur, which are caused by the onset of interband transitions, although their effect is still rather small. In addition to the resonance frequency, the plasmon resonance is also characterised by its quality factor  $Q$ . For non-linear optics experiments, a strong local-field enhancement is desirable and achieved by a sharp resonance. This is represented by a high  $Q$  factor, which is defined by

$$Q \simeq \frac{\lambda_{\text{res}}}{\Delta\lambda_{\text{res}}} , \quad (3.10)$$

where  $\lambda_{\text{res}}$  denotes the resonance wavelength and  $\Delta\lambda_{\text{res}}$  the full width at half maximum of the resonance. Simulated results are displayed in figure 3.4(c) and compared to analytic calculations based on the quasistatic approximation [Jac98]. In this approximation only Ohmic losses are considered and it evaluates to

$$Q(\omega) = \frac{\omega}{2 \text{Im}(\varepsilon(\omega))} \frac{\text{dRe}(\varepsilon(\omega))}{\text{d}\omega} , \quad (3.11)$$

with the resonance frequency  $\omega$  and the dielectric function  $\varepsilon(\omega)$  [Wan06]. Most notably equation (3.11) does not depend on the antenna geometry. The quasistatic approximation is therefore an upper limit to the quality factor for structures, which are not governed by retardation effects. This is mostly the case for small particles, although small resonators with  $Q$  values far larger than the quasistatic limit have been built [Fei08]. According to equation (3.11) the plasmon resonance's sharpness is fixed once the material and the resonance frequency are chosen. Different geometric antenna shapes thus mainly change the resonance frequency and have less influence on the quality factor.

In comparison with the quasistatic limit, the simulated  $Q$  values are lower than the approximated ones, which is caused by a combination of Ohmic and radiation losses. Recent experiments have shown a dominance of radiation damping in optical antennas [Han12], which is characterised by the plasmon damping time. Typical time scales range from 2 fs to 5.5 fs depending on the antenna shape and volume [Han09; Han12]. Although simulated quality factors show a maximum around a resonance wavelength of 700 nm, it is advantageous to work in the infrared or near-infrared spectral range. First of all, resonant antennas are larger there, which makes it easier to manufacture them according to the simulated design. Secondly, all materials for plasmonic applications behave more like ideal metals in that spectral range leading to reduced losses.



### 3.3 Near-field intensity distribution

#### 3.3.1 Simulation geometry

Aside from the spectral properties of the antenna resonance, the near-field intensity distribution is also of fundamental interest, particularly the intensity enhancement. Both quantities are obtained from FDTD calculations. Figure 3.5 depicts the simulation geometry used for the near-field intensity distribution calculations. The principal setup including the applied material models and boundary conditions, is analogous to the one used for transmission spectra in section 3.2. However, the antennas are illuminated by a 16 fs excitation pulse centred around 800 nm to match later experiments. Moreover, the detection plane is placed at half the antenna's height to measure the electric field from which the near-field intensity enhancement  $\alpha_{\text{FDTD}}$  is determined. It is defined by

$$\alpha_{\text{FDTD}} = \frac{|\mathbf{E}|^2}{|\mathbf{E}_0|^2} = \frac{E_x^2 + E_y^2 + E_z^2}{E_{x,0}^2 + E_{y,0}^2 + E_{z,0}^2}, \quad (3.12)$$

where  $\mathbf{E}_0$  denotes the incident electric field [Sch05]. The latter is obtained from a reference calculation, where the same simulation geometry without the antenna is used. A typical colour plot of the near-field intensity enhancement is shown in figure 3.6.

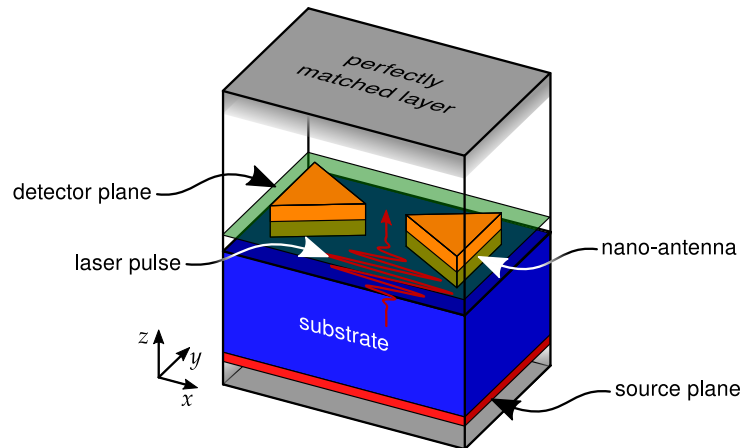


**Figure 3.5:** Simulation geometry to calculate the near-field intensity enhancement of optical antennas. The geometry is similar to the previous one. Despite outputting the flux going through a detection plane, the electric field within a detection plane is examined. The detection plane is placed at half the antenna's height to avoid perturbations from the edges.

### 3.3.2 Results

The normalised near-field intensity enhancement for a rod-type optical antenna is plotted colour coded in sub-figure (b) of figure 3.6. Sub-figures (a) and (c) show line-outs in  $y$ -direction along the dashed line and along the solid line respectively. The antenna in question has an arm length of 75 nm, a width and height of 24 nm, and a feed gap of 20 nm. Each antenna arm radiates significantly at the outer edges and the near-fields stretch into the surrounding dielectric. Sharp corners show an increased enhancement due to the lightning rod effect, leading to enhancement factors of up to 100. However, even at the flat end facets an approx. 50 fold increase in intensity is observed. The highest values occur in the gap region though, where the near-fields of each antenna arm overlap constructively and an intensity enhancement of up to 190 is achieved. To visualise the enhancement at the end facets the maximum colour value in figure 3.6 is set to 100. The inset shows a close up of the gap region with a different colourmap compared to sub-figure (b) to illustrate the intensity distribution there. It is non-uniform and exhibits slightly different features than the field at the outer edges, where the maximum enhancement occurs at the antenna surface. In the gap on the other hand it is higher in the centre in  $x$ -direction as plotted in sub-figure (c). In sub-figure (a) the enhancement in  $y$ -direction shows two maxima positioned at the same value as the antenna's upper and lower surface. Furthermore, the lightning rod effect also occurs in the gap region, leading to strongly localised enhancement factors of up to  $9 \cdot 10^2$ . However, the covered volume is tiny compared to the rest of the feed gap volume. On the other hand, the red area in sub-figure (b) indicates a region with an enhancement factor of  $10^2$  or larger, which extends further into the surrounding dielectric and even beyond the actual gap area. This results in a relatively large enhancement volume, which is crucial for non-linear experiments. Moreover, an enhancement factor of  $10^2$  is theoretically very often sufficient since, for instance, laser oscillators reach peak intensities of  $10^{11} \text{ W cm}^{-2}$  when tightly focussed. Thus, with the given enhancement factor, intensities in the order of  $10^{13} \text{ W cm}^{-2}$  are accessible, which are necessary for high-order harmonic generation. The mechanism behind this process is explained in more detail in chapter 4.

Although rod-type antennas facilitate high intensity enhancement factors, even higher values are beneficial for non-linear optics experiments since these processes scale strongly with the incident intensity. As already seen, notably higher enhancement is caused by the lightning rod effect. Bow tie antennas make use of it to achieve

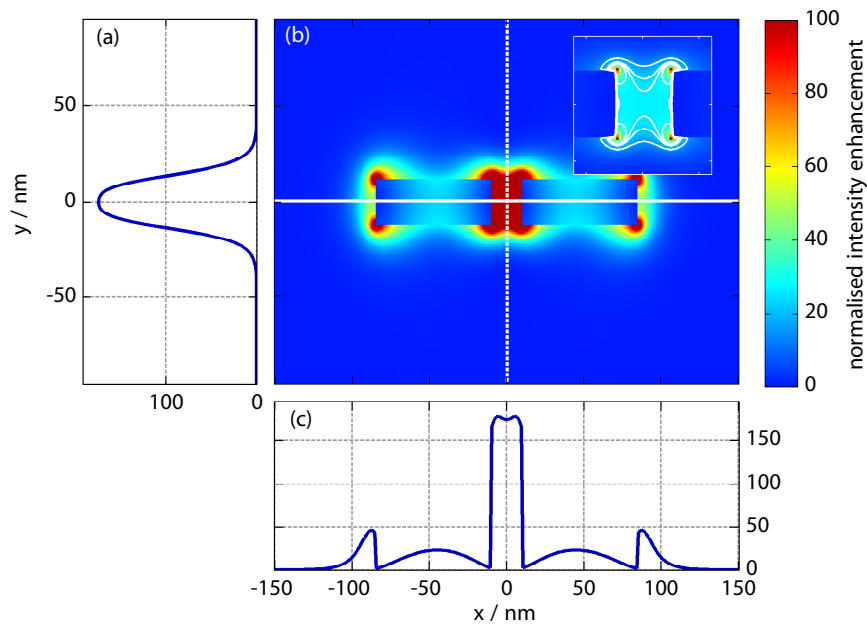


**Figure 3.6:** Near-field intensity distribution for a rod-type optical antenna. Sub-figure (a) and (c) show line-outs in  $y$ -direction along the dashed line and along the solid line, respectively. In the gap region enhancement factors of up to 190 are observed. On the outer edges of each single-wire antenna significant enhancement occurs, too. The inset shows a detailed plot of the gap region with a different colourmap ranging from 0 (blue) to 650 (red).

enhancement factors of up to  $10^3$ .

A typical map with line-outs in  $x$ - and  $y$ -direction is plotted in figure 3.7. As before, the maximum colour value in sub-figure (b) is limited to 100 to show field distribution details at the outer antenna edges. A close up of the gap region is plotted in the inset using a different colourmap with respect to sub-figure (b) and contour lines for further illustration. The principal field distribution resembles that of rod-type antennas with significant enhancement at the outer antenna edges. There, the highest enhancement factors occur at the antenna surface, reaching values in the order of 60. Furthermore, the geometry with its rounded edges is mapped into the field distribution. Local hot spots appear both at the curved and at the tilted surface. They result from the grid discretisation, leading to a staircasing approximation of the antenna geometry [Kun93]. Thus, they have no physical counterpart. However, a rough surface also leads to hot spots in experiments, which are similar to those from the staircasing effect. Within the gap region, the electric field is strongly enhanced in a large area. The field reaches its

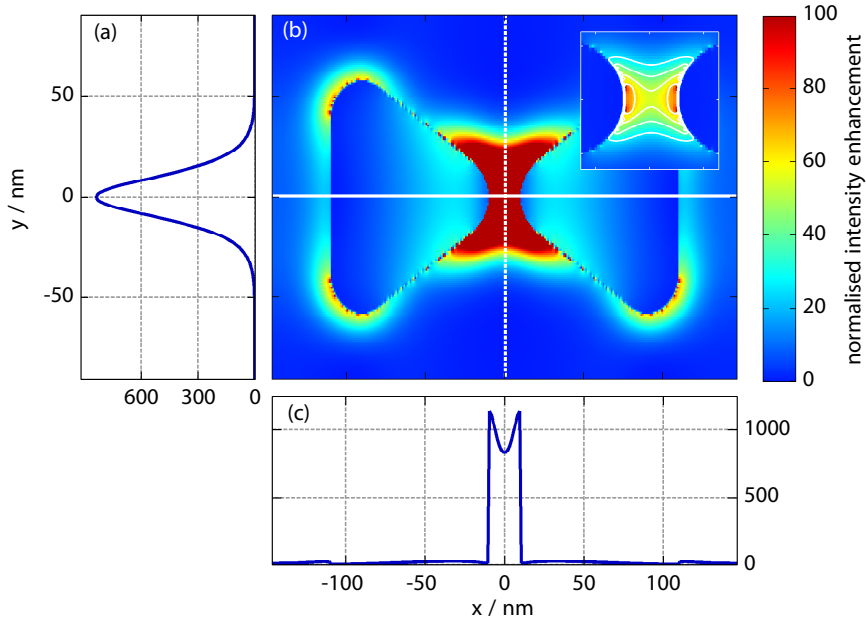


**Figure 3.7:** Near-field intensity distribution for a bow tie optical antenna. Sub-figure (a) and (c) show line-outs in  $y$ -direction along the dashed line and along the solid line, respectively. In the gap region enhancement factors of up to 1500 are observed. On the outer edges of each antenna arm significant enhancement occurs, too. The inset shows a detailed plot of the gap region with a different colourmap ranging from 0 (blue) to 1500 (red).

maximum directly at the tip's surface with enhancement factors of up to  $1.5 \cdot 10^3$  as shown in sub-figure (c). The inset illustrates its waist in  $x$ -direction, which is centred in the middle of the gap. In the  $y$ -direction, the maximum enhancement is reached in the centre and gradually falls off to the sides. To summarise, bow tie antennas facilitate a field enhancement almost three times larger than rod-type antennas do. Experimentally they are harder to manufacture though, because the geometry is more complex than rod-type antennas.

### 3.4 Temperature distribution

The temperature distribution within optical antennas is usually measured via two photon luminescence studies [Baf10], showing good agreement with theoretical considerations outlined in section 2.8. Particularly for experiments aiming at high-order harmonic generation via a plasmonic field enhancement, the temperature distribution

of the antennas is of major importance, since reshaping due to melting can occur [Cha99; Lin99a; Wan11]. FDTD-calculations give access to the electric field and hence the heat source density  $q_{\text{FDTD}}$ , which is defined by equation (2.21). Here, the focus lies on the spatial heat distribution and its maximum value after exposure to a single laser pulse. Moreover, the introduced antenna shapes are compared with each other to assess their susceptibility to thermal damage. The resulting temperature increase after illumination with a particular laser pulse is calculated in section 3.5 and not considered here.

### 3.4.1 Simulation geometry

Figure 3.8 shows a sketch of the simulation geometry used to determine the temperature distribution within optical antennas. The principal setup is again analogous to the one used for transmission spectra in section 3.2. However, to calculate the antenna temperature, the heat source density within the whole antenna is needed. According to equation (2.21), this mainly depends on the electric field as well as the imaginary part of the dielectric function. Thus, both quantities are analysed within the depicted detection volume. A simulation without the antenna serves as a reference to normalise the electric field analogous to near-field intensity calculations described previously.

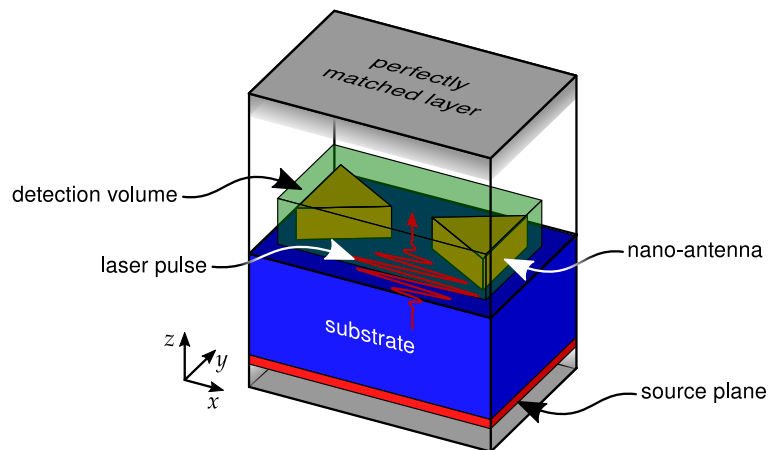


**Figure 3.8:** Simulation geometry to calculate the temperature distribution inside an optical antenna. Both  $\text{Im}(\varepsilon(\omega))$  and the electric field inside the detection volume are output for further analysis.

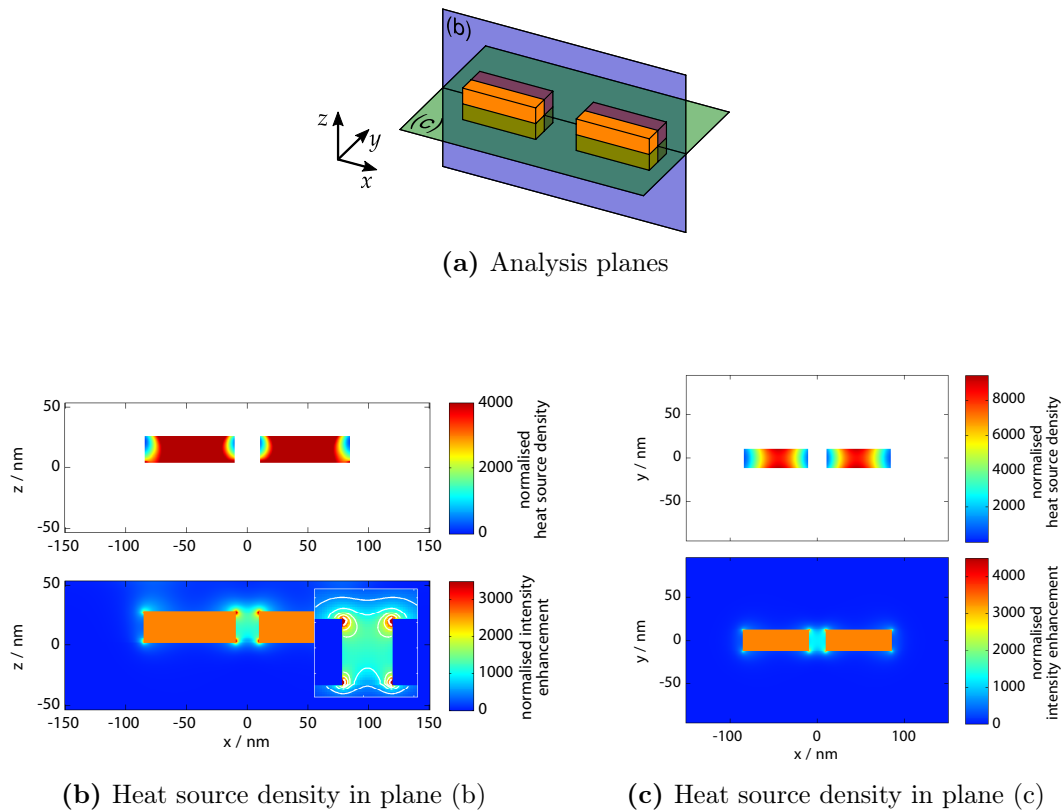


**Figure 3.9:** top: heat source density of a rod-type two-wire antenna. The antenna has an arm length of 75 nm, an antenna width of 24 nm, and a feed gap of 10 nm. bottom: corresponding normalised intensity enhancement.

### 3.4.2 Results

In figure 3.9, the heat source density and the normalised intensity enhancement for a rod-type two-wire antenna with an arm length of 75 nm, an antenna width of 24 nm, and a feed gap of 20 nm are displayed in the planes sketched in figure 3.9(a). The heat source density is calculated according to equation (2.21) from the determined electric field and the fitted data for the dielectric function. In figure 3.9(b) the substrate is located in the bottom half and treated as an ideal dielectric with a zero imaginary part of the dielectric function. Thus, the heat source density is also zero and the laser pulse itself does not deposit heat in the substrate. In the antenna on the other hand, the non-zero imaginary part of the dielectric function leads to an almost uniform heating of the structure with two prominent minima at the outer antenna edges.

The respective intensity enhancement is plotted in the bottom half of figure 3.9(b). Within the gap area maxima occur at the sharp antenna edges. At the antenna's top,

the enhancement stretches far into the dielectric, whereas at the bottom this area is smaller due to the substrate material. Generally, with resonantly chosen antenna lengths, enhancement factors are in the order of 1000 and larger.

In figure 3.9(c) the heat source density as well as the intensity enhancement in the  $xy$ -plane are plotted. Towards the upper and lower antenna edges the former exhibits two distinct maxima in each antenna arm. This is in good agreement with previous calculations for currents in a rod-type geometry [Cro03]. At the outer antenna ends the current decreases, leading to a charge accumulation which in turn causes the pronounced enhancement in the gap area. The latter is shown in the bottom half of figure 3.9(c).

Analogous calculations were carried out for a bow tie antenna with 110 nm antenna length,  $30^\circ$  opening angle, 20 nm feed gap, 20 nm radius of curvature and an antenna height of 30 nm. Both the heat source density as well as the normalised intensity enhancement are displayed in figure 3.10 in the planes sketched in sub-figure (a). As

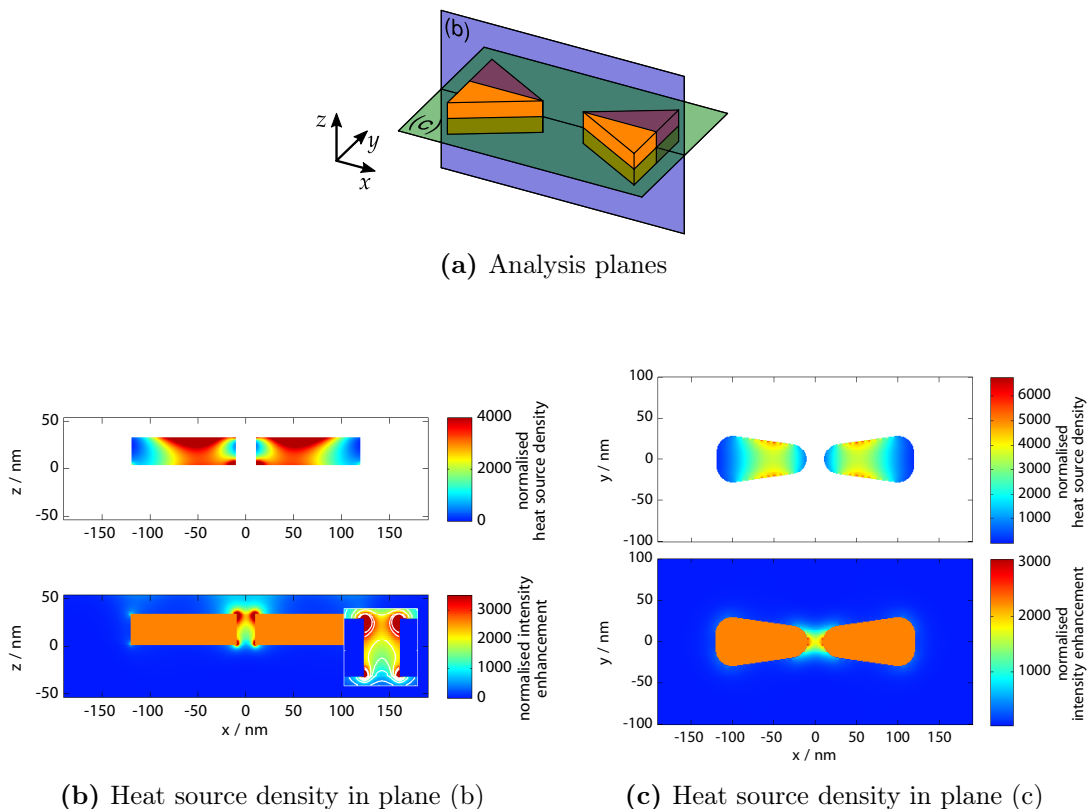


**Figure 3.10:** top: heat source density of a bow tie antenna with 110 nm antenna length,  $30^\circ$  opening angle, 20 nm feed gap, 20 nm radius of curvature and an antenna height of 30 nm. bottom: corresponding normalised intensity enhancement.

for rod-type antennas, the substrate is located in the bottom half in figure 3.10(b) and treated as an ideal dielectric with a zero imaginary part of the dielectric function. Thus, again the heat source density is also zero and the laser pulse itself does not deposit heat in the substrate. The substrate is therefore only heated via heat conduction and serves as a cooler for the antenna.

In the antenna on the other hand, the non-zero imaginary part of the dielectric function leads to heating of the structure with two prominent maxima in each antenna arm. One occurs at the apex' bottom caused by the strong local electric field there, which also reaches into the antenna material. The other one is located at the top of the antenna at the interface to the surrounding dielectric i.e. vacuum or air. Its origin becomes clearer after examining the electric field in the  $xy$ -plane. Generally, heat deposition within the antenna is strongly non-uniform and mostly concentrated at the antenna half facing towards the gap. In particular, the outer antenna ends are only heated via heat conduction and thus reduce the overall temperature in each antenna arm. Interestingly, a minimum for the heat source density also occurs at the upper apex part, even stretching further into the antenna, although the antenna's bottom part is significantly heated.

The corresponding electric field enhancement in the  $xz$ -plane is shown in the bottom half of figure 3.10(b), which is also non-uniform along the antenna thickness. Two pronounced maxima occur at the antenna's top and bottom side and are caused by the sharp tips in that direction. The top one is particularly strong because the field stretches undisturbed into the dielectric, whereas at the bottom the field distribution is changed due to the additional interface resulting from the substrate. Nonetheless, enhancement factors in the order of  $10^3$  are present in large parts of the gap area along the  $z$ -direction.

Figure 3.10(c) shows the heat source density and the normalised intensity enhancement factor for the same bow tie antenna as before in the  $xy$ -plane. The former exhibits strongly localised maxima at the interface to the surrounding dielectric, which coincide with those observed in the  $xz$ -plane and decrease towards the centre line. At both antenna ends no heating occurs, because surface charge is accumulated there, resulting in a decreasing current towards the ends. This is in agreement with previous calculations for currents in bow tie antennas [Cro03]. On the other hand, the accumulated surface charge leads to the strong field enhancement plotted in the bottom half of figure 3.10(c).



In comparison, bow tie antennas not only feature a higher intensity enhancement at resonance than rod-type antennas, but also exhibit a lower heat source density. Thus, bow tie antennas are less susceptible to thermal damage and better suited for experiments with high incident intensities, which are potentially close to the damage threshold. In the following, these thermal effects are analysed in greater detail.

## 3.5 Temperature evolution

Heat accumulation in the nano-antennas is a possible process for high repetition rates. It is therefore necessary to assess the influence of multiple pulses on the antenna temperature. This is achieved by solving the diffusion equation (2.23) with an appropriate initial temperature  $T_0$ . From the calculations outlined above a spatially averaged heat source density for different nano-antenna shapes is obtained. The initial temperature  $T_0$  is then finally determined by the averaged heat source density in combination with the particular laser pulse, i.e. its energy density.

### 3.5.1 Model

As a first approximation, the exact temperature distribution in the antenna is neglected and a spatially averaged heat source density is determined from previous calculations for each antenna. To further simplify the problem, the optical antenna is treated as a spherical nano-particle with radius  $R$  such that the volumes of the sphere and the antenna are equal. Solving the diffusion equation (2.23) is therefore reduced to a one dimensional problem, which can be implemented much more easily [Baf11] and provides an upper bound for the antenna temperature. This is a common method to determine bounds for and this way evaluate numerical methods, for instance in computational mechanics [Zoh08]. In the model the particle itself is immersed in a surrounding medium e.g. sapphire or fused silica. To account for the experimental conditions, where the antenna is deposited on top of a substrate, the thermal conductivity is lowered proportionally to the contact area in the  $xy$ -plane. Since the remaining surrounding medium is vacuum, heat conduction does not occur and its contribution to the temperature evolution is neglected. All material parameters are also assumed to be constant within the considered temperature range. Moreover, the duration of the incident laser pulse has to be much smaller than the characteristic time of

electron-phonon scattering for gold nano-particles  $\tau_{\text{e-ph}} \approx 1.7$  ps [Arb03; Hod99; Hua07; Lin99b], which is fulfilled for the maximally 9 fs long pulses used in the experiments.

Because of the symmetric system, spherical coordinates are used. The temperature increase  $T(r,t)$  at a point  $r$  and time  $t$  is then determined by the diffusion equation (2.23). This yields a set of two differential equations with boundary conditions at the interface between the antenna and the substrate

$$\begin{aligned} \rho_{\text{np}}c_{\text{np}}\partial_t T(r,t) &= \kappa_{\text{np}}\nabla^2 T(r,t) + q(r,t) \quad \text{for } r < R \\ \rho_{\text{sub}}c_{\text{sub}}\partial_t T(r,t) &= \kappa_{\text{sub}}\nabla^2 T(r,t) \quad \text{for } r > R . \end{aligned} \quad (3.13)$$

The boundary conditions at  $r = R$  are given by

$$\begin{aligned} \kappa_{\text{sub}}\partial_r T(R,t) &= \kappa_{\text{np}}\partial_r T(R,t) \\ T_{\text{sub}}(R,t) &= T_{\text{np}}(R,t) . \end{aligned} \quad (3.14)$$

Here,  $\kappa$  denotes the thermal conductivity,  $c$  the specific heat capacity,  $\rho$  the mass density, and  $q(r,t)$  the heat source density. The subscripts refer to the nano-particle and the substrate, respectively. The set of equations in (3.13) and (3.14) is then solved numerically by using a finite difference method and a Runge-Kutta algorithm. Details concerning the implementation are explained in [Baf11].

Heating of the nano particle is described as a three step process resulting from the different time scales involved [Gru03; Ino98].

*Electronic absorption* First, the gas of free electrons in the nano-particle interacts with the incident laser pulse and the pulse energy is absorbed proportionally to the spatially averaged heat source density  $q$ . Subsequently the electronic gas thermalises very fast to a Fermi-Dirac distribution over a time scale  $\tau_e \approx 100$  fs [Ino98]. Thus, the electronic temperature  $T_e$  increases while the lattice temperature  $T_p$ , i.e. phonons, is still unchanged, resulting in a non-equilibrium state of the nano-particle. The absorbed energy is determined from the nano-antenna's normalised heat source density  $q$  calculated in section 3.4 and the incident laser pulse energy density  $\mathcal{E}_p$ .

$$E_{\text{abs}} = \mathcal{E}_p q V , \quad (3.15)$$

where  $V$  denotes the nano particle's volume.

*Electron-phonon thermalisation* In a second step, the hot electron gas cools down via internal electron-phonon scattering, which is characterised by the time scale  $\tau_{\text{e-ph}}$ . For nano-particles larger than 5 nm this time is approximately 1.7 ps [Arb03; Hod99; Hua07; Lin99b]. Although the nano-particle is now at a uniform temperature, it is not in equilibrium with the surrounding medium yet.

*External heat diffusion* Finally, this equilibrium is achieved via diffusion at a characteristic time scale  $\tau_{\text{d}}$ , leading to a cooling of the nano particle and a heating of the surrounding, respectively. This time scale depends on the nano-particle size and increases for larger particles. Typical time scales for a water gold interface range from 100 ps to a few nanoseconds. In case of particles smaller than 20 nm the last time step can even overlap with the electron-phonon thermalisation [Hu02]. Normally, however, the latter is much faster than the external heat diffusion and the nano-particle's initial temperature  $T_0$  is given by energy conservation and related to the absorbed energy  $E_{\text{abs}}$

$$E_{\text{abs}} = V \rho_{\text{np}} c_{\text{np}} T_0 \quad , \quad (3.16)$$

where  $V$  denotes the nano-particle's volume,  $\rho_{\text{np}}$  its mass density, and  $c_{\text{np}}$  its specific heat capacity. In combination with equation (3.15) this yields

$$T_0 = \frac{q \mathcal{E}_{\text{p}}}{\rho_{\text{np}} c_{\text{np}}} \quad . \quad (3.17)$$

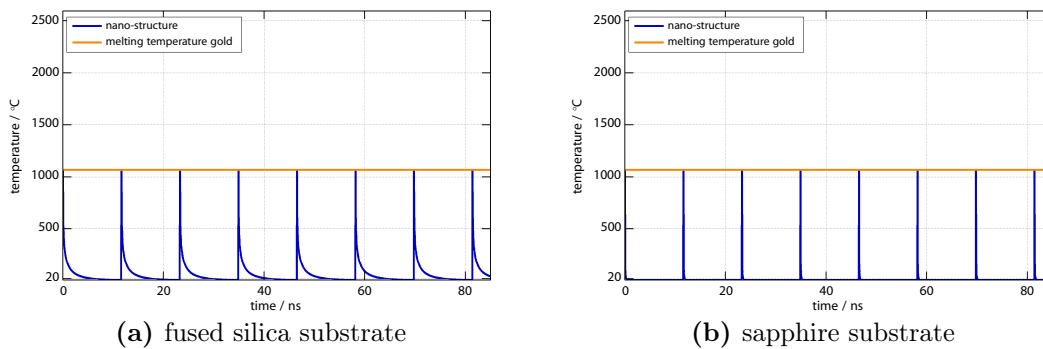
The initial temperature increase therefore only depends on the pulse energy density, i.e. the pulse energy, and is independent of the pulse duration. In case  $T_0$  reaches the nano-particle's melting temperature, the latent heat of fusion also has to be considered to calculate the correct initial temperature. The used material constants are listed in table 3.1.

### 3.5.2 Results

Figure 3.11 shows the temperature evolution of a typical bow tie antenna on a fused silica and a sapphire substrate illuminated by eight successive pulses with a repetition rate of 86 MHz for an incident intensity of  $1 \cdot 10^{11} \text{ W cm}^{-2}$ . For a fused silica substrate plotted in figure 3.11(a) the antenna reaches the melting temperature of gold, but the

**Table 3.1:** Physical constants of used metals and substrate materials

	gold	sapphire	fused silica	unit
thermal conductivity $\kappa$	317	42	1.38	$\text{W m}^{-1} \text{K}^{-1}$
specific heat capacity $c$	129	750	1050	$\text{J kg}^{-1} \text{K}^{-1}$
mass density $\rho$	19.32	3.97	2.2	$10^3 \text{kg m}^{-3}$
thermal diffusivity $a$	127	4.7	0.199	$10^{-6} \text{m}^2 \text{s}^{-1}$
melting temperature	1336	2313	1988	K
heat of fusion	62.8			$10^3 \text{J kg}^{-1}$

**Figure 3.11:** Temperature evolution for an incident intensity of  $1 \cdot 10^{11} \text{W cm}^{-2}$ 

absorbed energy is only sufficient to melt a small fraction of the antenna. Therefore only minor damage to the antennas is expected. Heat conduction serves as a cooling mechanism and leads to a temperature decrease between two successive pulses. The thermal conductivity of fused silica limits the cooling, which becomes already apparent in figure 3.11(a). For the given repetition rate however, it is still sufficient and the antenna returns to its initial temperature before the next laser pulse heats it up again. Thus, despite the dramatic temperature increase after exposure to a laser pulse, no heat is accumulated within the nano-structures and consequently they are also expected to be stable on a long term basis. However, this does not hold for higher repetition rates because in that case the antennas would not return to their initial temperature and heat is accumulated. This effect can be compensated for by using a substrate with a higher thermal conductivity as shown in figure 3.11(b) for a sapphire substrate.

The maximum antenna temperature is independent of the substrate material hence they behave analogous to those on a fused silica substrate. Due to the 30 times higher thermal conductivity however, cooling is much stronger and consequently the antenna

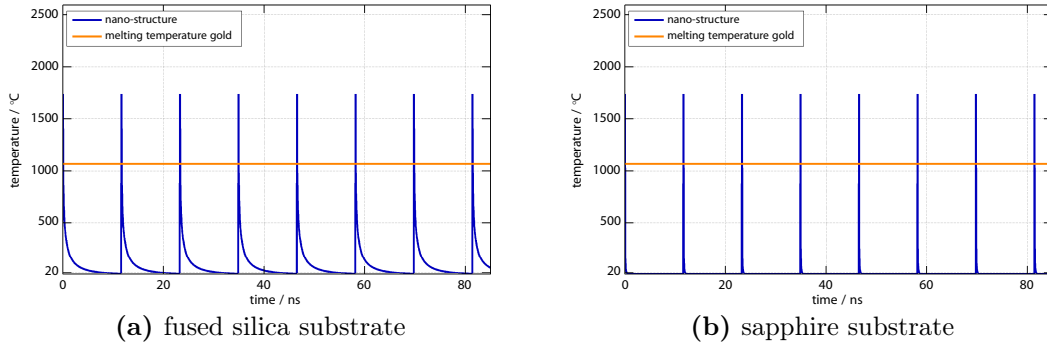


**Figure 3.12:** Temperature evolution for an incident intensity of  $2 \cdot 10^{11} \text{ W cm}^{-2}$

returns to its initial temperature significantly faster than in the case of fused silica.

In figure 3.12 the same bow tie antenna as before is illuminated with a peak intensity of  $2 \cdot 10^{11} \text{ W cm}^{-2}$ , twice as high as in the previous simulation. In this case, the melting temperature of gold is clearly exceeded and the material suffers a phase change from solid gold to liquid gold. Although the melting temperature is only exceeded for a few picoseconds, the antenna shape is expected to change [Koc05; Kor03] with detrimental effects on the antenna properties. According to equation (3.15), the absorbed energy and hence the maximum temperature for a given antenna design only depends on the pulse energy density. Therefore every antenna has a maximal incident intensity at which it is not yet damaged. For the one in figure 3.11 this intensity is  $1.4 \cdot 10^{11} \text{ W cm}^{-2}$ .

### 3.6 Antenna optimisation

The previous sections outlined different aspects of optical antennas, which are determined from FDTD calculations. For non-linear optics experiments and high-order harmonic generation in particular, all these aspects have to be combined to optimise the antenna design. For bow tie antennas the design parameters are sketched in

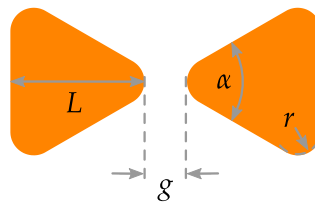


**Figure 3.13:** Bow tie antenna parameters

figure 3.13. However, only the antenna length  $L$ , and the gap size  $g$  are incorporated in the optimisation. This is due to constraints imposed by the manufacturing process, which limit the structures experimentally available. For example, the radius of curvature  $r$  at the edges is typically around 10 nm and the thickness  $t$  is usually 50 nm. Staircasing effects on the other hand limit the opening angle  $\alpha$  to  $30^\circ$ . Therefore, these parameters are kept constant.

As outlined in section 2.7.2 the gap size  $g$  has a major effect on the coupling between individual antenna arms and consequently also on the resulting intensity enhancement factor. Figure 3.14 shows the normalised intensity enhancement in the middle of the gap as a function of the gap size  $g$  as well as an exponential fit to the simulated data for 80 nm long antenna arms. For smaller gap sizes the enhancement factor increases exponentially with a steep slope, such that the enhancement at 20 nm gap size is already an order of magnitude smaller than for 10 nm gaps. For larger gap sizes the achievable enhancement is even further reduced. Thus to maximise the enhancement, gap sizes as small as possible are desirable, although this also reduces the volume in which enhancement occurs.

Ultimately, the determined antenna design also has to be experimentally feasible and manufactured reproducibly. Given the major influence of the gap size on the enhancement, this parameter is critical and has to be well-controlled, especially having the desired dimensions in mind. So far, gap sizes smaller than 20 nm have only been demonstrated for isolated antennas [Hua10b; Mer08] and are generally difficult to

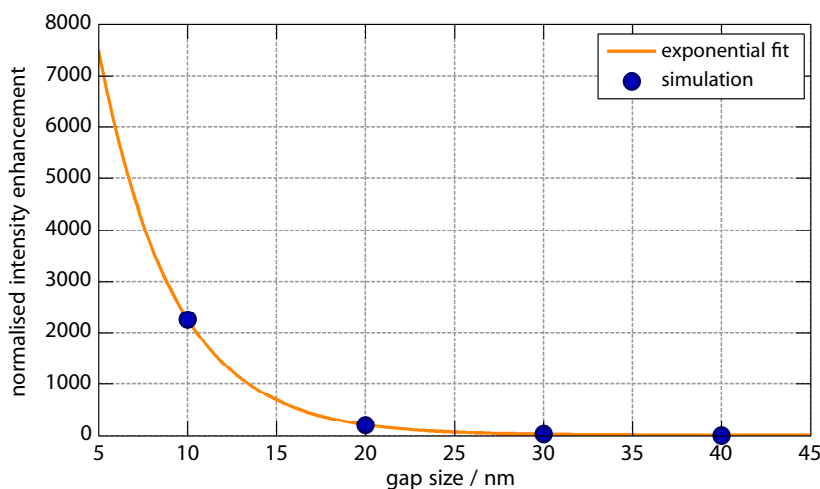


**Figure 3.14:** Intensity enhancement at the middle of the gap as a function of the gap size  $g$ . The antenna arm length is fixed at 80 nm.

achieve. For the intended experiments, however, antenna arrays are needed to increase the harmonic yield. There, 20 nm are achieved reproducibly and hence used for all further calculations.

Secondly, the antenna length is expected to have an important influence on the enhancement by shifting the resonance wavelength according to the Fabry-Pérot resonator model introduced in section 2.7.1. In figure 3.15 the normalised enhancement factor in the gap centre as well as at the apex are displayed for different antenna lengths. As in the calculations before, the antennas are illuminated by laser pulses centred around 800 nm. The enhancement reaches its maximum for an antenna length between 110 nm and 120 nm with enhancement factors well beyond 1500 in the centre and roughly 3000 at the tip. For larger antenna lengths the enhancement continuously drops down and is already halved at the centre and reduced to one third at the tip, for a 150 nm long antenna. In case of a 180 nm antenna only 20% of the peak enhancement at 115 nm remain in the gap centre and just 16% at the tip. Thus, especially for non-linear experiments, where an as high as possible field enhancement is beneficial, the optimal antenna length should be used.

So far, the optimisation process mainly focused on finding design parameters which facilitate a maximised intensity enhancement factor without taking possible damage processes like melting into account. Section 3.5 on the other hand pointed out the threshold intensity at which destruction to the design is still avoided. Figure 3.16

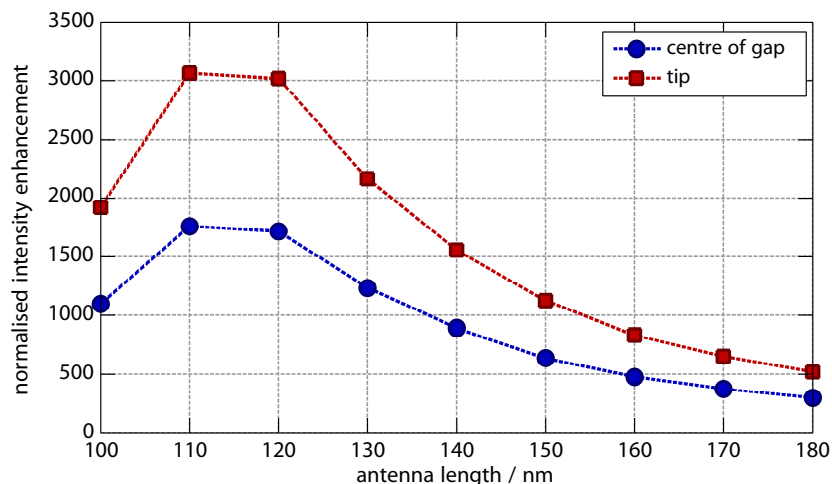


**Figure 3.15:** Intensity enhancement in the gap centre and at the tip as a function of the antenna arm length  $L$  at a constant gap size  $g$  of 20 nm. The antenna height is 30 nm for all calculations.

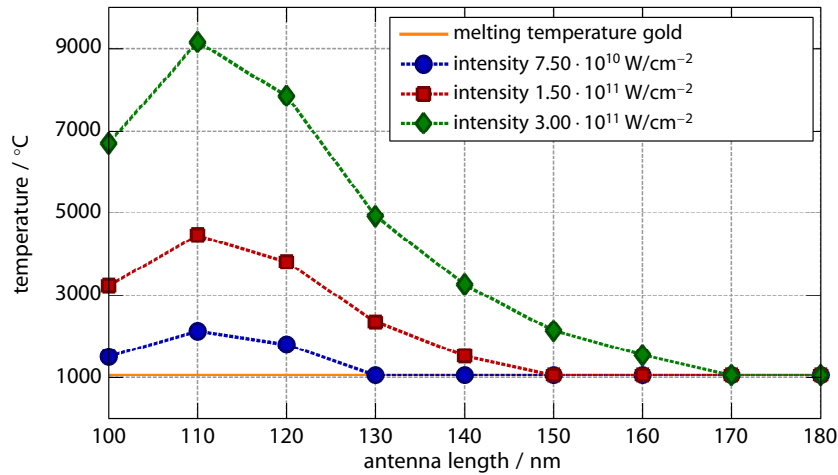


**Figure 3.16:** Maximal antenna temperature for different incident intensities as a function of the antenna length  $L$ .

shows the maximal antenna temperature for different incident intensities as a function of the antenna length  $L$  as well as the melting temperature of gold. Even for the lowest intensity of  $7.5 \cdot 10^{10} \text{ W cm}^{-2}$  antennas shorter than 130 nm are damaged due to melting because they are close to the resonance length of 115 nm. With increasing intensity the damage threshold shifts towards longer antennas since more energy has to be absorbed to heat them to the same temperature. Incorporating thermal effects into the design process of optical antennas for high-order harmonic generation thus considerably alters the optimal design parameters.

For high-order harmonic generation, intensities in the order of  $10^{13} \text{ W cm}^{-2}$  are required

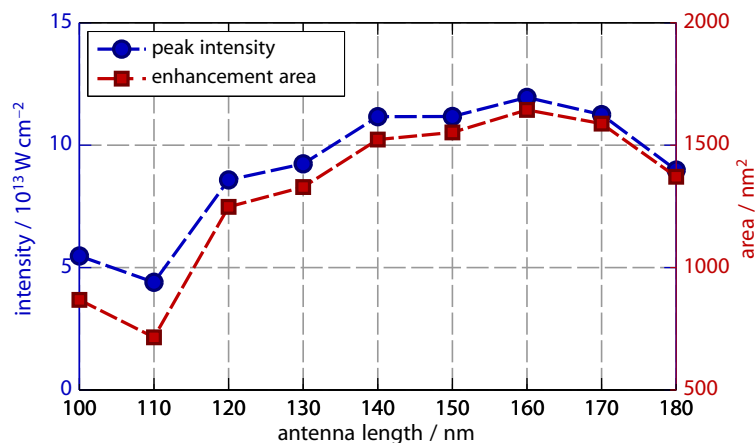


**Figure 3.17:** Temperature optimisation of bow tie nano-antennas.



and the harmonic yield ultimately depends on the peak intensity and the volume in which it is present. Therefore, taking thermal damage into account, not only the maximum enhancement has to be considered, but also the maximally possible incident intensity without damaging the antennas. Both quantities are derived by previously explained calculations. The intensity in the gap centre including enhancement from the nano-antennas as well as the area in the  $xy$ -plane with an intensity of at least  $3 \cdot 10^{13} \text{ W cm}^{-2}$ , is plotted for different antenna lengths in figure 3.17. For every length, thermal damage is avoided by choosing the respective maximum incident intensity. Antennas between 140 nm and 175 nm enable peak intensities higher than  $10^{14} \text{ W cm}^{-2}$  with an enhancement area in the  $xy$ -plane of more than  $1500 \text{ nm}^2$  per antenna. Both the peak intensity and the enhancement area are maximal for a 160 nm long antenna. Taking the accuracy of the manufacturing process into account, antennas between 140 nm and 175 nm are expected to produce the highest harmonic yield. All chosen parameters are experimentally feasible and different designs are experimentally tested in chapter 5.



# CHAPTER 4

---

## Harmonic generation

---

Already shortly after the invention of the laser in 1960 optical harmonic generation has been demonstrated by frequency doubling in a crystal [Fra61]. Since then a large variety of effects such as self-phase modulation or high-order harmonic generation (HHG) were observed with increasing available laser power. Therefore, by examining the generated electrons and photons further insight into the light matter interaction has been gained. For the experiments conducted within this thesis, particularly low-order harmonic generation at a surface and HHG in noble gases are of special interest. First, the former is explained, followed by a brief introduction into HHG, especially concentrating on HHG in presence of optical antennas.

### 4.1 Light matter interaction with intense laser fields

For low laser intensities, the polarisation and the electric field are linearly related by equation (2.4) as introduced in section 2.2. For intense laser fields, i.e. with intensities of  $10^{13} \text{ W cm}^{-2}$ , on the other hand not only the linear susceptibility  $\chi^{(1)}$ , but also higher-order susceptibilities  $\chi^{(i)}$  become relevant. The induced polarisation is thus given by

$$P = \varepsilon_0 \chi^{(1)} E + \varepsilon_0 \chi^{(2)} E^2 + \varepsilon_0 \chi^{(3)} E^3 + \dots , \quad (4.1)$$

where  $\varepsilon_0$  denotes the permittivity of free space and  $E$  the electric field of the incident laser pulse [Boy03]. For better readability the vectorial and tensorial character of the respective quantities is omitted. Equation (4.1) explains low-order processes

like second harmonic generation (SHG) and third harmonic generation (THG), the conversion efficiency of which is described by perturbation theory. For even higher laser intensities the description with equation (4.1) breaks down, though, and new concepts have to be used, which are explained in section 4.3.

In any case, further insight into possible effects is gained by examining the non-linear susceptibilities' symmetry. For a medium which is symmetric under a transformation  $T$ , its tensorial susceptibilities  $\chi^{(i)}$  also have to be symmetric with respect to  $T$  as stated by Neumann's principle. Therefore, e.g. for inversion symmetric media, all even susceptibilities  $\chi^{(2)}, \chi^{(4)}, \dots$  vanish and only odd processes are observed. Not surprisingly a broken symmetry, introduced for example by a surface, exhibits additional effects. In the following, low-order harmonic generation at a surface is explained in more detail.

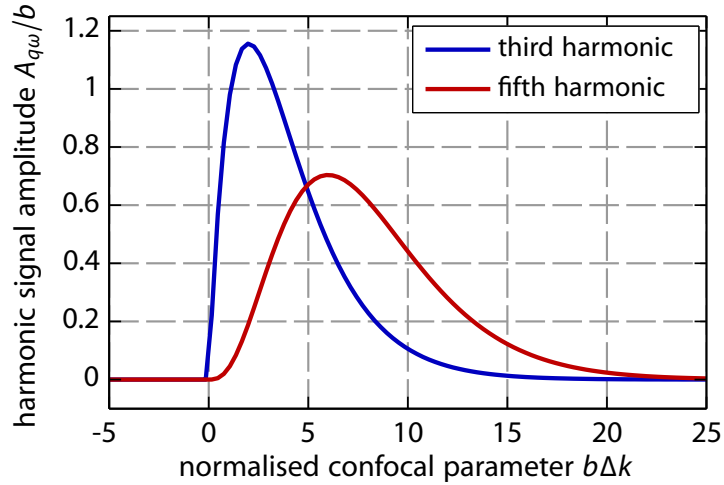
## 4.2 Surface harmonics

At a surface or an interface between two media, the bulk symmetry is broken and non-linear effects like SHG or THG are observed [Hei91; Tr 07]. Third-order non-linear effects in particular and specifically THG are of special interest for surface spectroscopy applications [Tr 07] since all materials have non-vanishing odd-order non-linear susceptibilities. THG is therefore a particularly well suited process to examine the surface of transparent objects [Bar97].

Low-order harmonics are described by the theory of harmonic generation with focussed Gaussian beams. The latter propagate in  $z$ -direction and the signal amplitude of harmonic order  $q$  is then given by

$$A_{q\omega} = \left| \int_{z'_L}^{z'_R} dz' \frac{\exp(i\Delta k z')}{(1 + 2iz'/b)^{q-1}} \right|^2. \quad (4.2)$$

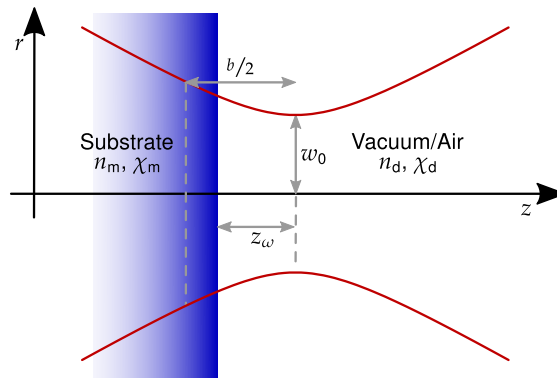
Here,  $\Delta k = k_{q\omega} - qk_\omega$  denotes the phase-mismatch between the fundamental wave number  $k_\omega$  and the  $q^{\text{th}}$  harmonic wave number  $k_{q\omega}$ . The fundamental beam is further described by its confocal parameter  $b = k_\omega w_0^2$ , the waist radius  $w_0$ , the normalised coordinate along the beam axis  $z' = z/b$ , and  $z'_L, z'_R$  are the respective input and output plane coordinates [Bar97; Boy03].



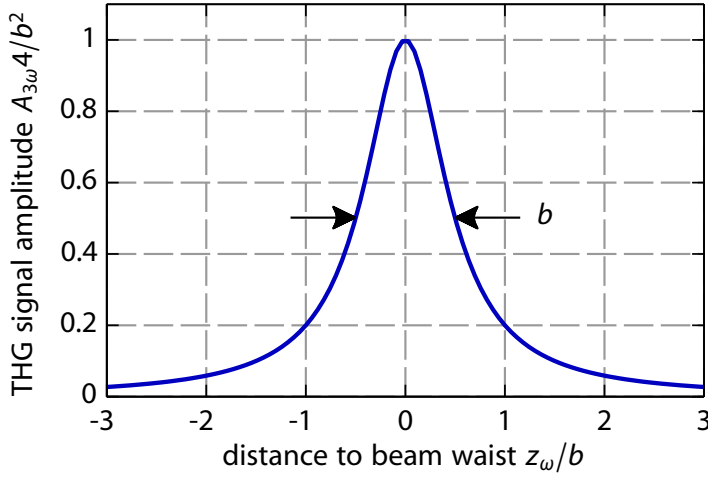
**Figure 4.1:**  $A_{q\omega}$  as a function of the normalised confocal parameter  $b\Delta k$  in the tight focussing limit for an infinite and uniform non-linear medium. Even for perfect phase-matching, i.e.  $\Delta k = 0$  the third and fifth harmonic signal vanish due to destructive interference of radiation produced before the focus with that generated after the focus.

Figure 4.1 depicts this harmonic signal amplitude as a function of the normalised confocal parameter  $b\Delta k$  in the case of an infinite, uniform non-linear medium and tightly focussed beams. For a phase-mismatch  $\Delta k \leq 0$  both the third and the fifth harmonic vanish, due to a destructive interference of radiation produced before the focus with that generated after the focus. This effect is caused by the Gouy phase shift and prevents for example THG in bulk media.

The situation is different at an interface, though, which is illustrated in figure 4.2. In particular, the medium is no longer uniform, but the refractive index and the



**Figure 4.2:** Low-order harmonic generation at an interface with a tightly focussed laser beam. The substrate is scanned along the optical axis with a distance  $z_\omega$  between the surface and the beam waist  $w_0$ . Both media are described by their refractive index  $n$  and the non-linear susceptibility  $\chi$ .



**Figure 4.3:** Amplitude of the third harmonic signal at an interface as a function of distance  $z_\omega$  to the beam waist  $b$ . Only close to the interface third harmonic radiation is efficiently generated within a FWHM set by the confocal parameter  $b$ .

non-linear susceptibility change from  $n_m, \chi_m$  in the medium to  $n_d, \chi_d$  in vacuum or air. Thus, efficient harmonic generation at the interface is realised via constructive interference. Concentrating on the THG process, and a single interface with perfect phase-matching, i.e.  $\Delta k = 0$ , the amplitude of the third harmonic signal is given by

$$A_{3\omega}(z_\omega) = \frac{b^2}{4} \frac{1}{1 + 4z_\omega^2/b^2}. \quad (4.3)$$

Here,  $z_\omega$  describes the distance between the interface and the beam waist [Sch02] as sketched in figure 4.2. The resulting THG amplitude is plotted as a function of this distance in figure 4.3. By scanning the interface along the optical axis the THG signal is optimised, which is only efficiently generated near the beam waist. It peaks when the interface is at the beam waist position and the FWHM is given by the confocal parameter  $b$ .

THG at interfaces has been studied experimentally in various solids [Tsa95] and also in liquids [Tsa96a]. Since odd order non-linear susceptibilities do not vanish, not only the third harmonic is generated at an interface, but also the next higher order process, namely fifth harmonic generation (FHG). However, THG has been found to be  $\approx 10^5$  times more efficient than FHG, indicating the generation process' perturbative behaviour [Pan89; Tsa96a].

Surface harmonic generation is further enhanced by making use of local resonances

e.g. plasmon resonances on metal surfaces [Tsa96b]. THG from a sample with optical antennas deposited on the surface is therefore an ideal tool to characterise the antennas in terms of their resonance properties [Sch09].

### 4.3 High-order harmonic generation

So far the interaction between atoms and the incident laser beam has had a perturbative character with peak intensities in the range of up to  $10^{13} \text{ W cm}^{-2}$  [Trä07]. For higher intensities the interaction becomes strongly non-perturbative and, among other things, HHG is possible [Kra92; Sch97].

Figure 4.4 shows a sketch of a typical harmonic spectrum generated in a gaseous medium, with the maxima occurring at odd integer multiples of the fundamental laser frequency. Within region I the intensity of low-order harmonics decreases rapidly with increasing order according to perturbation theory [Pan89] and is thus referred to as the perturbative regime. In the plateau region II on the other hand, the harmonic intensity stays relatively constant over many harmonic orders [Fer88; McP87]. This observation of a plateau in the harmonic spectrum is not explained by perturbation theory. The end of the plateau is marked by the cutoff in region III, where the harmonic intensity again decreases rapidly with harmonic order.

In general microscopic and macroscopic aspects have to be considered separately in HHG. The former is intuitively described by a semi-classical model introduced in section 4.3.1 and originates from the non-linear response of the atoms to the strong laser field. Macroscopic effects on the other hand, are caused by the coherent

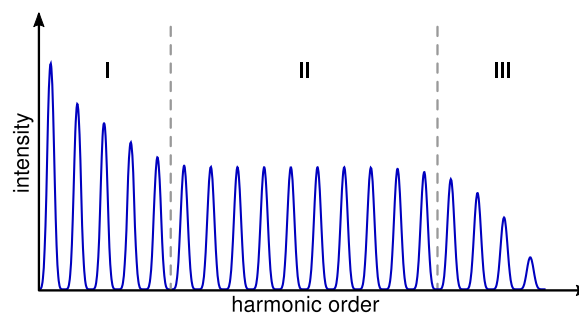


**Figure 4.4:** Sketch of a typical spectrum of high-order harmonics generated in a gaseous medium. The labelled areas are the perturbative region I, the plateau region II and the cutoff region III.

superposition of the fields emitted by all the atoms in the generating volume and are explained in section 4.3.2.

### 4.3.1 Semi-classical model

The semi-classical model explains the response of a single atom to the incident strong laser field [Cor93]. Both the laser field and the electron motion in the field are described classically, whereas the atom's electronic states are considered quantum mechanically. The generation process is then decomposed into three steps depicted in figure 4.5, where subfigure (a) shows the atomic potential without an external laser field.

#### Ionisation

Assuming a strong-field low-frequency regime, the atomic potential is deformed significantly leading to a lowered Coulomb barrier. Thus, the electron tunnels out from the core and tunnel ionisation becomes the dominating ionisation process as depicted in figure 4.5 (b). In general the tunnelling probability is high, when the electric field is at its maximum and minimal, when the electric field has a zero-crossing. Furthermore, the electron velocity  $v_0$  after the ionisation is assumed to be zero and the electron is located at the nucleus' position.

#### Acceleration

From this starting point the electron undergoes oscillations in the electric field  $E$ , while the Coulomb force from the nucleus is neglected. The mean kinetic energy

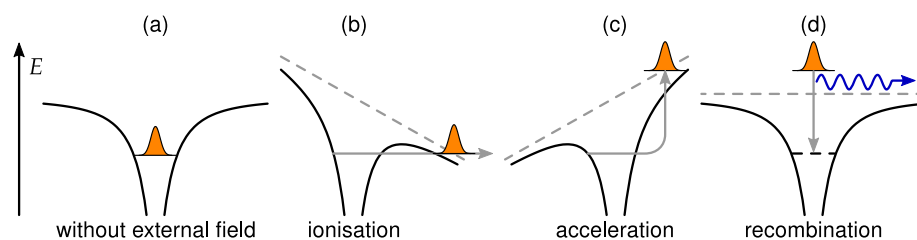


**Figure 4.5:** Semi-classical model of high-order harmonic generation. Subfigure (a) shows the atomic potential without an external laser field. In (b) the laser field has lowered the Coulomb barrier and electrons tunnel out from the core. These electrons are accelerated within the field (c) and can recombine with the parent ion (d), resulting in an emission of an XUV photon.



acquired by a free electron oscillating in the laser field is given by  $U_p$

$$U_p = \frac{e^2 \langle E^2 \rangle}{4m_e \omega^2} , \quad (4.4)$$

where  $e$  denotes the electron charge,  $m_e$  the electron mass and  $\omega$  the laser frequency.  $U_p$  is also known as the ponderomotive potential. When the laser field switches its sign, the electron travels in reverse direction and can thus return to its origin as shown in figure 4.5 (c).

### Recombination

Some of these returning electrons interact with their parent ion and lead to a radiative recombination depicted in figure 4.5(d). This light emission occurs at odd harmonics of the fundamental laser frequency. According to classical mechanics, the maximum kinetic energy acquired by the electron is  $3.17 U_p$ . In combination with the atom's binding energy  $I_p$ , the maximum photon energy is therefore given by

$$E_{\max} = 3.17 U_p + I_p . \quad (4.5)$$

Empirical values for the maximum kinetic energy range from 3.0 to 3.2 [Kra92; LHu93; Sch97].

The assumptions made by the semi-classical model have been justified by a full quantum mechanical theory, where a strong field approximation (SFA) to solve the time-dependent Schrödinger equation (TDSE) has been employed [Lew94]. Moreover, numerical simulations of the semi-classical model are qualitatively in good agreement with results from the full quantum mechanical description of HHG by the TDSE [Cor93; LHu91]. However, quantitative differences of up to one order of magnitude occur.

#### 4.3.2 Phase-matching conditions/macroscopic effects

As for low-order harmonics described previously, phase-matching is also important for efficient HHG. In case of HHG, however, different phase contributions play a role and compete with each other.

### Geometric phase

For HHG the fundamental laser beam is tightly focussed to reach the necessary peak intensities. The resulting change in wavefront curvature leads to a spatially dependent phase in comparison with a plane wave. This phase is typically referred to as the geometric phase and given by

$$\Phi_{\text{geo}}(r,z) = \underbrace{-\arctan\left(\frac{2z}{b}\right)}_{\text{Gouy-phase}} + \underbrace{\frac{\pi r^2}{\lambda R(z)}}_{\text{radial component}}, \quad (4.6)$$

where the first term represents the Gouy-phase along the propagation axis and the second term the phase resulting from the wavefront curvature. By defining a wave vector  $\mathbf{k}_1(r,z)$ , the coherence length  $L_{\text{coh}}$ , i.e. the length in which radiation interferes constructively, is determined [Bal97].  $\mathbf{k}_1$  describes the focussed laser beam and the wavefront's locus. Assuming beam propagation in  $z$ -direction, the wave vector becomes

$$\mathbf{k}_1 = k_1 \cdot \mathbf{e}_z + \nabla \Phi_{\text{geo}}, \quad (4.7)$$

with  $k_1 = 2\pi/\lambda$ . Further phase contributions are considered via pseudo wave vectors to calculate the total phase-mismatch  $\Delta k$ .

### Atomic phase

Another major phase contribution results from the electrons produced within high-order harmonic generation. While in the continuum, the electrons accumulate quantum phase, leading to a phase lag with respect to the generating laser field. It is usually referred to as the atomic phase and is obtained from the time-dependent dipole moment. Both the dipole strength as well as the phase depend on the intensity  $I$ . Within certain intensity ranges the latter is to a first order given by

$$\Phi_{\text{at}}(r,z) \approx -\alpha \cdot I(r,z). \quad (4.8)$$

Here,  $\alpha$  is a coefficient depending on the quantum path [Bal97], which is numerically determined from quantum mechanical calculations [Lew94]. Figure 4.6 shows the dipole strength and the atomic phase for the seventh harmonic in xenon for intensities of up to  $2 \cdot 10^{14} \text{ W cm}^{-2}$ . In the plateau regime, i.e. for intensities larger than  $5 \cdot 10^{13} \text{ W cm}^{-2}$ ,

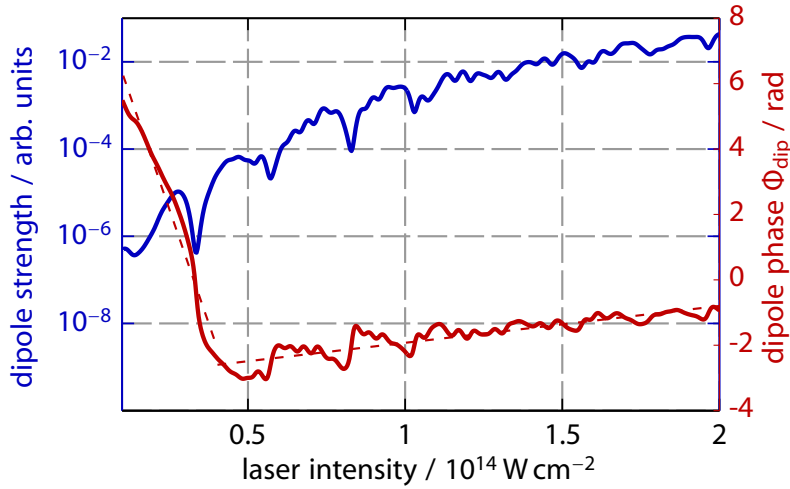


**Figure 4.6:** Dipole strength and dipole phase of the seventh harmonic in xenon as a function of intensity. The data is obtained from numerical simulations based on SFA solutions to the TDSE [Lew94]. For intensities higher than  $5 \cdot 10^{13} \text{ W cm}^{-2}$  the seventh harmonic lies in the plateau, leading to phase fluctuations caused by quantum path interference. The dashed lines indicate piecewise linear phase approximations for the plateau and cutoff regime.

the phase fluctuates. This is caused by different quantum paths interfering with each other. For lower intensities only one quantum path contributes, which leads to a smooth phase. The proportionality factors are  $\alpha_{\text{cutoff}} = -27.8 \cdot 10^{-14} \text{ cm}^2 \text{ W}^{-1}$  and  $\alpha_{\text{plateau}} = 1.1 \cdot 10^{-14} \text{ cm}^2 \text{ W}^{-1}$  respectively. The wave vector describing atomic phase contributions is

$$\mathbf{K}(r,z) = \nabla \Phi_{\text{at}} \approx -\alpha \nabla I(r,z) . \quad (4.9)$$

### Dispersion effects

Principally, neutral atoms as well as free electrons affect phase-matching for HHG. However, for the case of HHG utilising optical antennas the calculated maximum peak intensities are in the order of  $1.3 \cdot 10^{14} \text{ W cm}^{-2}$  as shown in figure 3.17. For xenon, this leads to less than 10% of ionised atoms and a coherence length of more than 1 mm. Given the typical antenna dimensions, this is already five orders of magnitude larger than the generation volume. Therefore, free electrons are not further considered for phase-matching.

The situation is similar for neutral atoms: with an estimated gas pressure at the sample in the millibar regime the coherence length due to neutral atoms alone is in the

order of several millimetres. Thus, this effect is also not considered in the following.

### Generalised phase-matching condition

The previously introduced phase contributions, namely the geometric phase in equation (4.7) and the atomic phase in equation (4.9), yield the wave vector of the harmonic beam  $\mathbf{k}_q$ , which is

$$\mathbf{k}_q(r, z) = q\mathbf{k}_1(r, z) + \mathbf{K}(r, z) . \quad (4.10)$$

Its length is then  $k_q = q\omega/c$  and the phase-mismatch becomes

$$\Delta k = k_q - |q\mathbf{k}_1 - \mathbf{K}| . \quad (4.11)$$

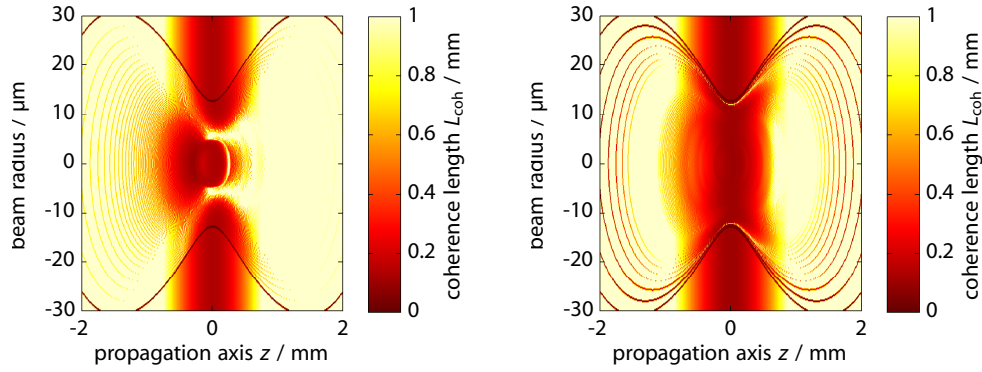
Since the coherence length  $L_{\text{coh}}$  is inversely proportional to the phase-mismatch  $\Delta k$  it is given by

$$L_{\text{coh}} = \frac{\pi}{|k_q - |q\mathbf{k}_1 - \mathbf{K}||} . \quad (4.12)$$

Areas with a small phase-mismatch therefore have large coherence lengths, indicating a significant contribution to the overall harmonic signal and vice versa [Roo99]. In the following the coherence length is used to assess phase-matching conditions for the case of nano-structure enhanced HHG.

#### 4.3.3 Phase-matching in the case of optical antennas

To analyse the phase-matching conditions in the case of HHG utilising optical antennas, the effects described in section 4.3.2 are examined numerically. Instead of relying on the linear approximation for the atomic phase, results from the quantum mechanical model [Lew94] were used. The necessary parameters are taken from the experiment and are listed in table 4.1. Figure 4.7 depicts the coherence length of the seventh and ninth harmonic in xenon as a function of propagation distance  $z$  and the beam radius  $r$ , with the fundamental beam propagating from left to right. White areas indicate a coherence length of at least 1 mm, i.e. five orders of magnitude larger than the thickness of the generation volume of approximately 50 nm. For both harmonics the interplay between the geometric and the atomic phase is clearly visible from the bow tie like features in the plots. For the seventh harmonic, the focus is particularly



(a) Phase-matching map for the 7<sup>th</sup> in xenon

(b) Phase matching map for the 9<sup>th</sup> in xenon

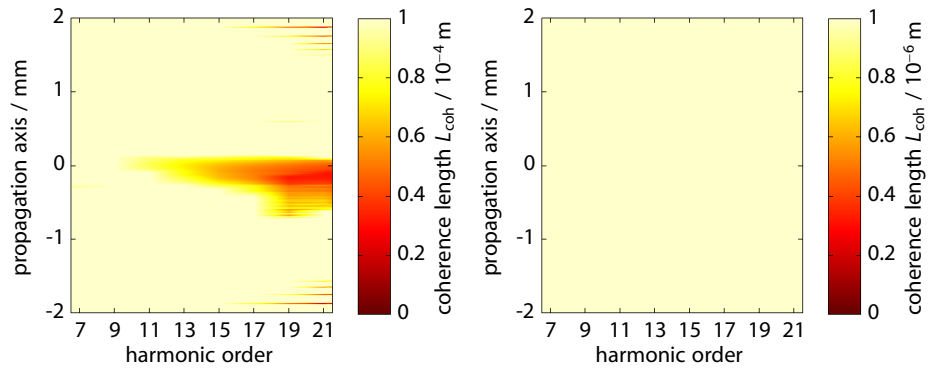
**Figure 4.7:** Phase-matching map for different harmonic orders as a function of propagation distance and beam radius. The fundamental beam propagates from left to right.

pronounced in the centre with coherence lengths in the order of 0.1 mm as shown in figure 4.7(a). The same feature is also found for the ninth harmonic in figure 4.7(b), but less distinct. Interestingly, there is an area of good phase-matching directly after the focus for the seventh harmonic, similar to the case of conventional HHG [Sal95], which is followed by an area with a lower coherence length.

Figure 4.8 gives an overview of the coherence length along the propagation axis for various harmonic orders using two different length scales. On a scale of  $10^{-4}$  m depicted in figure 4.8(a), phase-matching limits the harmonic generation around the beam waist for higher harmonic orders. On a length scale of one micron however, perfect phase-matching is achieved. Bearing the optical antenna dimensions with a thickness of 50 nm in mind, phase-matching is not expected to have a significant influence on HHG utilising optical antennas. This is particularly interesting from a

**Table 4.1:** Simulation parameters to analyse phase-matching conditions

parameter	value
ionisation potential $I_p$	12.1 eV (xenon)
confocal parameter $b$	$6 \cdot 10^{-4}$ m
peak intensity $I$	$1 \cdot 10^{14}$ W cm <sup>-2</sup>
pulse duration $\tau$	7 fs
central wavelength $\lambda$	820 nm



(a) Phase-matching map on a length scale of  $10^{-4}$  m.

(b) Phase-matching map on a length scale of  $1 \mu\text{m}$ .

**Figure 4.8:** Overview over phase-matching along the propagation axis for various harmonics at different length scales. Already for a generation volume with a thickness of  $1 \mu\text{m}$  perfect phase-matching is achieved. Therefore for HHG utilising optical antennas, no phase-matching effects are expected to influence the generation process.

theoretical point of view, since it opens up the opportunity to experimentally study microscopic and macroscopic effects of HHG independently.

#### 4.3.4 Field inhomogeneities

So far, the presented models did not consider the field inhomogeneity introduced by optical antennas and bow tie antennas in particular. Moreover, the presence of metallic particles confines the electrons produced during the HHG process within the gap area since they can principally collide with the metal. Since the highest electric fields occur close to the antenna surface, one can assume that this effect would especially influence cutoff harmonics. Recently, the semi-classical model as well as the quantum mechanical model based on the SFA were extended to include both the field inhomogeneity and the confinement of the electron movement [Cia12; Hus11]. Interestingly, both models predict an extension of the observed cutoff and also a generation of even harmonics due to a broken symmetry. For a fundamental wavelength of 800 nm electron confinement effects have a low influence on the harmonic generation, although they become apparent for longer wavelengths.





# CHAPTER 5

---

## Experiments

---

The following chapter concentrates on the experimental realisation of nano-antenna enhanced harmonic generation. First, two production techniques used to fabricate the antennas are briefly introduced. This is followed by a description of the antenna characterisation in terms of their resonance properties and thermal stability. The non-linear medium and its density have a major influence on HHG. Consequently, the gas nozzle is also characterised to accurately determine the gas density at the sample. Finally, the experimental setup and the results on nano-antenna enhanced harmonic generation are described in detail.

### 5.1 Production techniques

In order to perform experiments with optical antennas, reliable and reproducible production techniques are necessary. Given the typical antenna dimensions, a resolution below 10 nm is needed to define critical dimensions. Assuming a desired antenna length of 100 nm, an undesired length change by 10 nm would already lead to an error of 10% with major effects on the resonance. Bearing this in mind, current production techniques are pushed to their limits and thus producing optical antennas according to the design parameters is a major challenge, when performing experiments with them [Müh05].

In general, there are two approaches for producing optical antennas. Bottom-up approaches on one hand are based on chemical synthesis and self-assembly of metal nano-particles in solution and are therefore experimentally easy to realise. However,

to create non-trivial structures like bow tie antennas appropriate assembly strategies are required. These production techniques are therefore not considered further. On the other hand, top-down approaches such as electron beam lithography (EBL) and focussed ion beam (FIB) milling are capable of producing large arrays of almost identical and well defined antennas [Tse08]. Both techniques have been used to manufacture optical antennas for the experiments conducted within this thesis and are briefly described in the following.

### 5.1.1 Electron beam lithography

Electron beam lithography (EBL) is a technique commonly used to fabricate optical antennas on a flat substrate [Dor10; Fro04; Han09; Sch05]. The manufacturing steps are sketched in figure 5.1. First the substrate is coated with a high-resolution electron-sensitive resist such as PMMA (a), which is then patterned with a focussed electron beam (b). These patterns are then developed and selectively removed with a solvent (c). Subsequently a thin gold film with the desired thickness is evaporated onto the sample, covering both the voids and the remaining resist (d). Finally, the remaining resist is removed with a solvent, which leaves the metal structures in the voids unaffected and the written structures are uncovered (e).

Small structures in particular are easily destroyed during the lift off process, because the gold film does not stick well to the substrate material. Therefore, an adhesion layer of chromium with a thickness of less than five nanometres is used to increase the structures' stability. However, this layer can significantly increase the surface plasmon's damping [Hua10a]. Despite this effect, within this thesis all samples produced with EBL use an adhesion layer made of chromium.

A major advantage of EBL is, that large arrays of nano-structures can be easily produced. Therefore the antenna arrays have a diameter of  $25\ \mu\text{m}$ , which enables a variety of different focal spot sizes ranging from  $20.6\ \mu\text{m} \times 13.8\ \mu\text{m}$  to  $8.2\ \mu\text{m} \times 5.6\ \mu\text{m}$  and also allows a shift of the focal spot if necessary.

### 5.1.2 Focussed ion beam milling

Another manufacturing process for optical antennas is focussed ion beam (FIB) milling [Cub06; Kim08], which is sketched in figure 5.2. Here, a thin adhesion layer is also

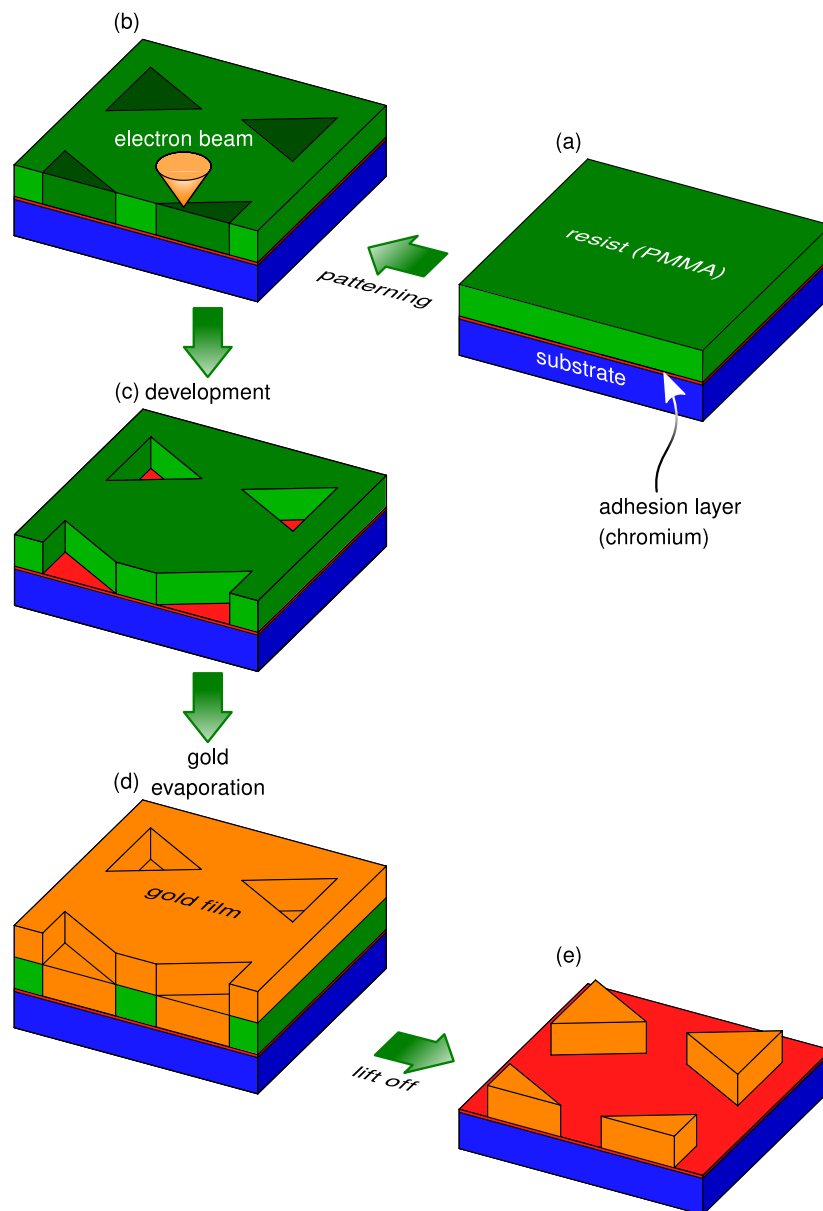


**Figure 5.1:** Electron beam lithography: A substrate is first coated with a high-resolution electron-sensitive resist (a) and then patterned with an electron beam (b). Afterwards, the written patterns are developed with a solvent (c). Gold is then evaporated onto the sample to cover the voids as well as the resist (d). Finally, the remaining resist is removed with a second solvent and the antennas are uncovered.

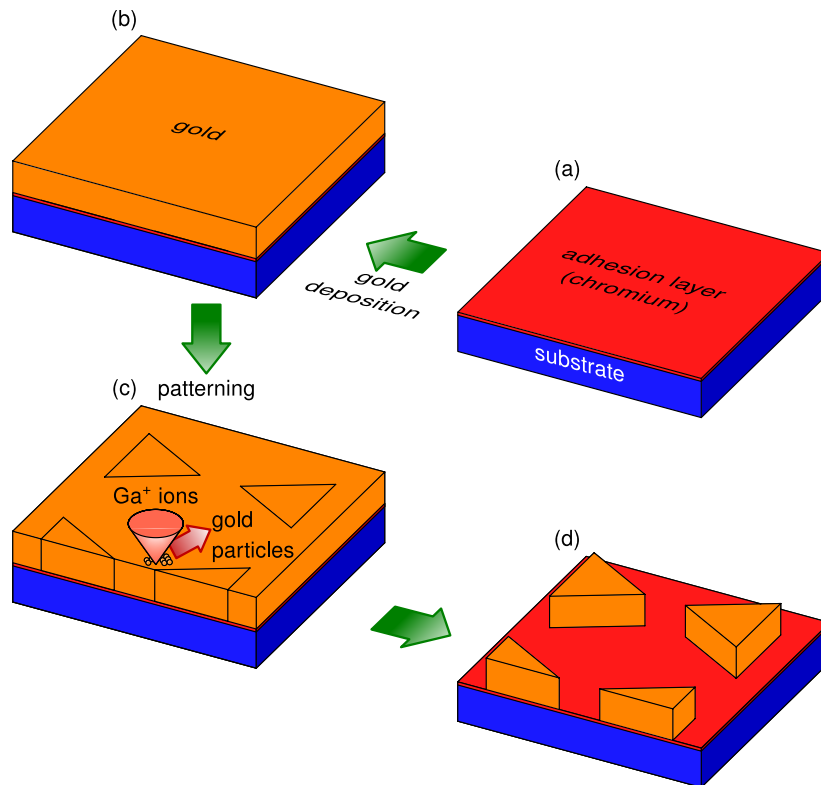
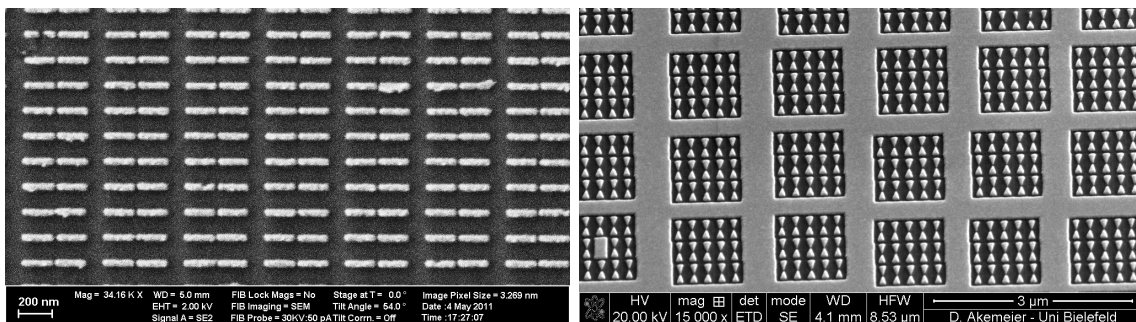


**Figure 5.2:** Focused ion beam milling: A substrate material is coated with an adhesion layer to improve the mechanical stability of the produced antennas (a). Afterwards a gold film of desired thickness is deposited onto the substrate (b). The antennas are then patterned with a gallium ion beam, whereupon all unwanted material is sputtered away (c). Only the antennas remain on the substrate (d).



(a) Rod-type antenna produced with EBL.

(b) Bow tie antenna produced with FIB

**Figure 5.3:** SEM images of produced nano-antennas. In case of EBL only the antennas remain on the substrate, whereas for FIB fabricated antennas the space between antenna blocks is still covered in gold to reduce the production time.

placed onto the substrate (a) before the gold film is deposited (b). A large variety of deposition processes can then be used to produce the gold film on top of the adhesion layer. Evaporation techniques for instance result in gold films with many small crystal grains of different size. A more uniform gold film with smaller crystal grain sizes on the other hand is obtained by using a sputtering technique. This allows a significantly higher spatial resolution, which is only exceeded by single crystalline metal flakes [Hua10a]. The patterning itself is performed by a focussed gallium ion beam which is scanned over the sample. Ion collisions cause a cascade within the gold film and particles are sputtered away from their original position (c), which leaves the desired structure on the substrate (d) [Tse08].

The main advantage of FIB milling is the very good spatial resolution in the range of 10 nm [Hua10b] and the direct manipulation of the designed structures. However, the manufacturing process is more time consuming than EBL since all the unwanted material has to be removed. This is sometimes redeposited onto the produced structures and causes an unintentional design change. Additionally, the accelerated ion beam can lead to ion implantation into both the gold film and the substrate with influences on the dielectric properties of the materials. Recently, gallium residues have been found to have an impact on the resonance frequency and quality factor of FIB-produced nano-antennas [Han11].

Several samples used for experiments in this work were produced with FIB milling, nonetheless. Due to the longer fabrication time, the antenna arrays are smaller than those produced with EBL, though, and have a quadratic form with an edge length of 20 nm. Figure 5.3 shows exemplary scanning electron microscope (SEM) images of optical antennas produced with EBL and FIB for the experiments described in the following.

## 5.2 Nano-antenna characterisation

All further experiments are based on the same optical setup sketched in figure 5.4. A homebuilt Ti:sapphire oscillator with  $< 10$  fs pulse duration centred around 820 nm with an average output power between 270 mW to 400 mW at a repetition rate of 80 MHz is used as a driving laser for the harmonic generation. The pulses are negatively chirped by several bounces on DCMs to compensate for dispersion added later i.e. a vacuum window, an achromatic lens and the substrate. It is fine-tuned via a pair of

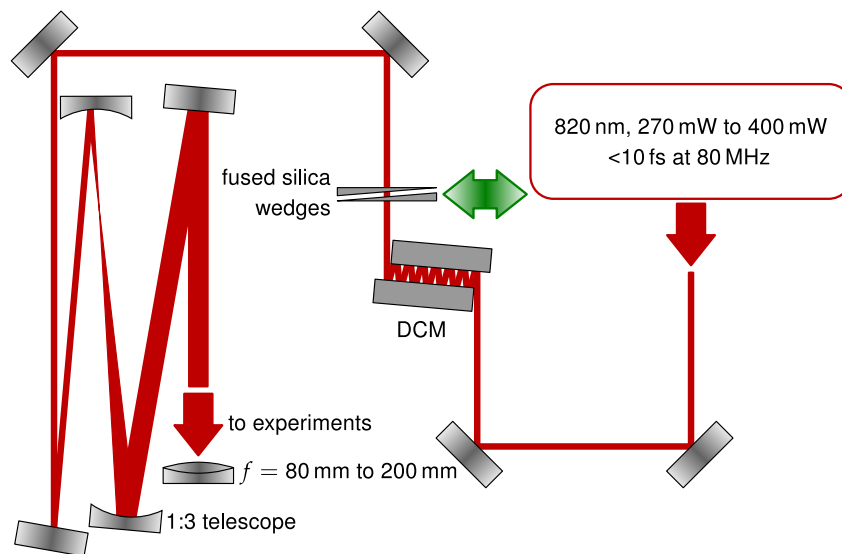
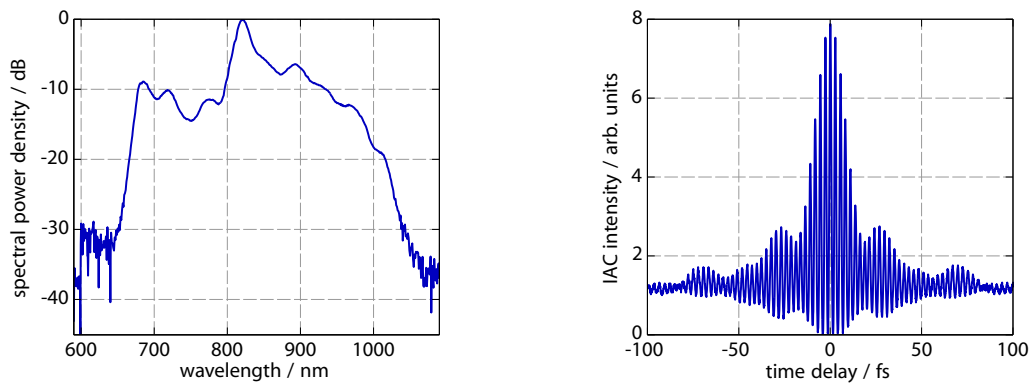


**Figure 5.4:** Sketch of the optical setup for nano-antenna enhanced harmonic generation. A homebuilt Ti:sapphire oscillator delivers pulses with a pulse duration of  $<10$  fs. Several reflections on a pair of DCMs in combination with a pair of fused silica wedges are then used to compensate for the dispersion of all used optical components in the setup. A telescope with a ratio of 1:3 then increases the beam size to tightly focus the laser beam onto the substrate with a variety of achromatic lenses.



(a) Driving laser spectrum with a bandwidth of more than 300 nm.

(b) Corresponding IAC trace of the laser pulse at the sample, after focussing with a 200 mm achromatic lens. It features a pulse duration at FWHM of 9 fs.

**Figure 5.5:** Spectrum and IAC trace of the driving laser. The pulse duration is measured behind the sample and thus confirms a well matched dispersion compensation.

thin fused silica wedges, where one wedge can be moved relative to the other. Finally, a telescope with a ratio of one to three expands the beam size to enable tight focussing with a variety of achromatic lenses.

Figure 5.5(a) shows the laser spectrum with a bandwidth of more than 300 nm. The corresponding interferometric autocorrelation (IAC) trace at the sample, i.e. with all optical components installed, is plotted in figure 5.5(b). It features a pulse duration of 9 fs measured at FWHM and demonstrates the correct dispersion compensation.

### 5.2.1 Third harmonic generation

The antenna design and the corresponding electric field enhancement is characterised with the setup depicted in figure 5.6, by means of the emitted THG signal. The optical setup has been described in the previous section and is therefore represented by the red box. Four different achromatic lenses with focal lengths reaching from 80 mm to

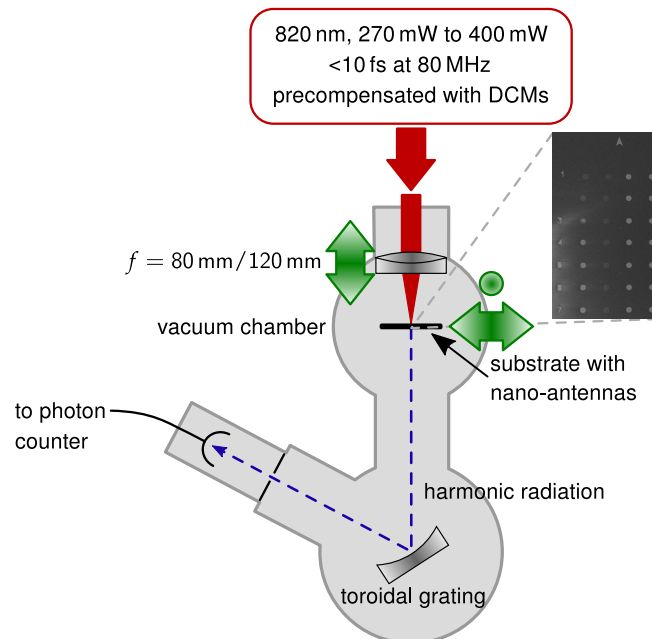


**Figure 5.6:** Sketched THG characterisation setup. For clarity the red box abbreviates the optical setup in figure 5.4. The laser beam is focussed with an achromatic lens onto the sample, which itself is mounted onto a two dimensional translation stage to address individual antenna arrays. These are represented by circles in the SEM image. The generation volume plays the role of the entrance slit to maximise the collection efficiency of the grating monochromator. A PMT detects the generated radiation behind the monochromator's exit slit. Green arrows indicate translation stages.

200 mm can be used for harmonic generation leading to different focal spot sizes and hence different peak intensities, which are listed in table 5.1. The lens is mounted on a translation stage to adjust the focal position as indicated by the green arrow, without breaking the vacuum. The sample with the nano-antennas is attached to a second translation stage moving in  $x$ - and  $y$ -direction to selectively address different antenna arrays, which appear as circles in the SEM image in figure 5.6. The laser polarisation and the antenna axis are aligned parallel to each other. To efficiently detect the generated harmonic radiation a confocal monochromator setup is used, where the generation volume acts as an entrance slit. The sample is thus mounted in the focal point of the toroidal mirror and the photon collection efficiency is maximised [Li89; Lin03]. Finally, a photomultiplier tube (PMT) capable of single photon counting (Hamamatsu H8259-09) is used in combination with a photon counter (Scientific Research SR400) to measure the harmonic signal behind the exit slit.

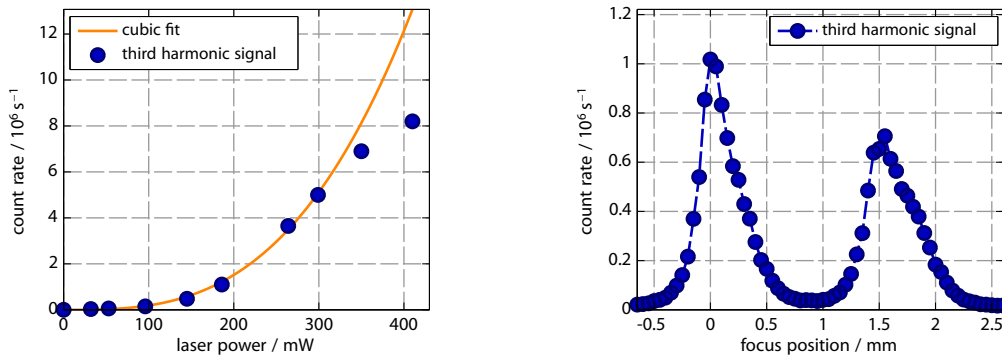
### Order of non-linearity and generation process

Figure 5.7(a) shows the generated THG signal as a function of the laser power and a cubic fit to the data. For this measurement rod-type antennas, which are produced with EBL are used. According to the datasheet of the PMT, the response is linear for up to  $2.5 \cdot 10^6$  counts/s and has an upper limit of  $12.5 \cdot 10^6$  counts/s. The non-linearity for higher count rates is already apparent in figure 5.7(a) for laser powers larger than 300 mW. Neglecting count rates higher than  $2.5 \cdot 10^6$  counts/s, the signal is fitted with a cubic function, which resembles the data perfectly and thereby confirms the order of the process. A further cross-check is performed by flipping a UV-grade fused silica substrate and a BK7 substrate into the harmonic beam. In the former case, the signal is reduced, whereas in the latter case it vanishes completely. Hence the radiation has a wavelength of less than 300 nm, which is in agreement with the third harmonic of

**Table 5.1:** Focal spot sizes for different achromatic lenses and corresponding peak intensities. The latter are calculated by taking the reconstructed pulse profile and the pulse duration from the IAC measurement into account.

focal length	focal spot size / $\mu\text{m}$	peak intensity / $10^{11} \text{ W cm}^{-2}$
200 mm	$20.6 \times 13.8$	1.8
120 mm	$12.4 \times 8.2$	5.1
100 mm	$10.4 \times 7.0$	7.2
80 mm	$8.2 \times 5.6$	11.4





(a) Third harmonic signal in dependence of incident laser power.

(b) Third harmonic signal in dependence of the focus position. Dashed lines serve as a guide to the eye.

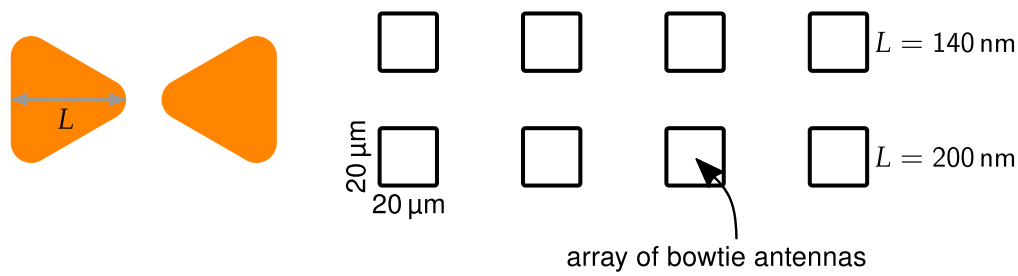
**Figure 5.7:** Third harmonic signal characterisation in terms of incident laser power and focus position. The signal increases with the laser power cubed and is generated at the surface of the substrate. It is therefore used to characterise the nano-antennas.

the driving laser at 273 nm.

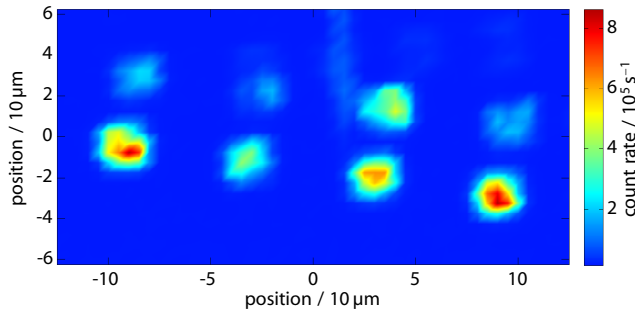
To understand the radiation's origin, the focal spot is scanned in  $z$ -direction, while the sample is fixed. In figure 5.7(b) the generated THG signal is plotted with respect to the focal position using a thick bare substrate. Two pronounced maxima appear with a spatial separation of 1.5 mm, which is exactly the substrate's thickness. Differing peak photon numbers for the front and back surface are caused by an increased pulse duration due to propagation of the laser pulse through the thick substrate. More specifically the incident 9 fs pulse is lengthened to 19 fs. Nonetheless, the experiment confirms the harmonic generation at the surface as described in section 4.2 and measured previously for other materials as well [Tsa95]. The generated THG can therefore be used to characterise the surface and hence the antennas [Sch09], as described below.

### Surface maps

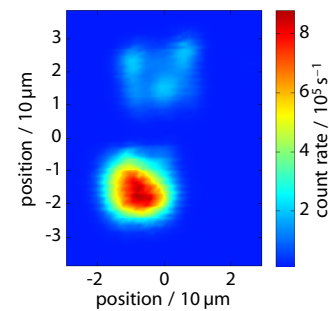
Since the THG process is sensitive to local resonances on the substrate's surface, their spatial distribution i.e. the position of the antenna arrays is determined by scanning the sample systematically in  $x$ - and  $y$ -direction, while measuring the harmonic signal at a wavelength of 280 nm. This way different antenna lengths are also resolved in the surface maps. For this particular measurement, bow tie antennas produced with FIB are used, although the technique serves as a tool for alignment purposes on a



(a) Sketched sample design.



(b) Overview map of a nano-antenna sample.



(c) Detail map of fourth column in (a).

**Figure 5.8:** Colour coded third harmonic signal as a function of  $x$ - and  $y$ -position to locate individual antenna arrays. Differences in the THG signal between the top and bottom row are due to different antenna arm lengths. Differences within one row are caused by imperfections resulting from the manufacturing process.

daily basis. Figure 5.8(b) shows the colour coded THG signal as a function of  $x$ - and  $y$ -position. All antenna arrays from the sample design figure 5.8(a) are reproduced although the intensity varies between different fields and especially between the top and the bottom row. The latter is due to different antenna arm lengths, which is 140 nm in the top row and 200 nm in the bottom row respectively. Within one row differences are explained by imperfections resulting from the manufacturing process. For example the antenna length or the opening angle can vary slightly, which is even the case within one antenna array. A detailed scan of the far right antenna arrays with a higher spatial resolution is shown in figure 5.8(c). The spatial dimensions with the quadratic shape and an edge length of 20  $\mu\text{m}$  are clearly visible in the bottom field. In the top field on the other hand, three brighter spots indicate different resonance properties with respect to the surrounding antennas. This illustrates the necessity to closely match the design parameters as well as the achievable accuracy of the FIB manufacturing technique.

## Spectrum

The differences between the rows in figure 5.8(b) become clear by examining the respective spectra, plotted in figure 5.9. They are measured using the antenna arrays in the third column in figure 5.8(b) and show a spectral shift with respect to the antenna length. For 140 nm antenna arms, the maximum occurs at 280 nm indicating a resonance wavelength of 840 nm. For 200 nm antenna arms on the other hand, the peak is located at 285 nm leading to a resonance wavelength of 855 nm. This spectral red-shift is in agreement with the simulations presented in section 3.6 and theoretical considerations from section 2.7.2. Due to the broad laser spectrum, with a bandwidth of more than 300 nm, both resonance wavelengths are covered and the spectral shift is observed in the experiments.

The different maximum photon numbers of  $8 \cdot 10^5 \text{ s}^{-1} \text{ nm}^{-1}$  and  $12 \cdot 10^5 \text{ s}^{-1} \text{ nm}^{-1}$ , however, are not explained by the simulations, which predict a higher field enhancement for the shorter antenna length. Consequently the generated THG signal should also be higher. On the other hand, the signal is highly dependent on the number of contributing emitters, which cannot easily be controlled when illuminating only a part of the whole antenna array. Varying antenna quantities are therefore most likely the cause for the observed difference in maximum photon numbers.

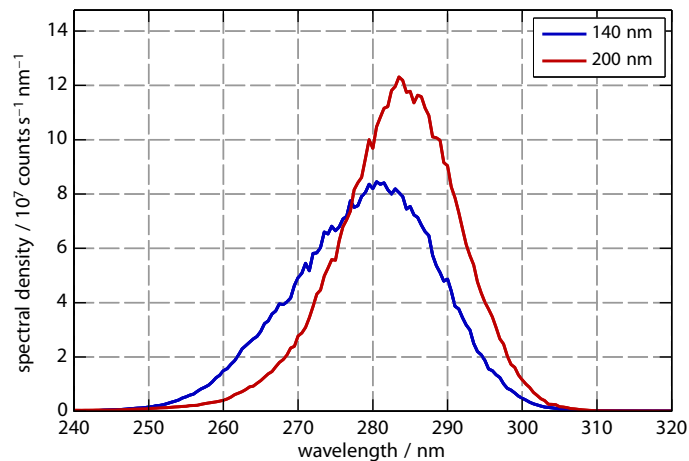


**Figure 5.9:** Third harmonic spectrum for 140 nm and 200 nm antenna arms. Longer antenna arms exhibit a red-shifted resonance with respect to shorter antennas. Differing maximum photon numbers point to unequal quantities of illuminated antennas.

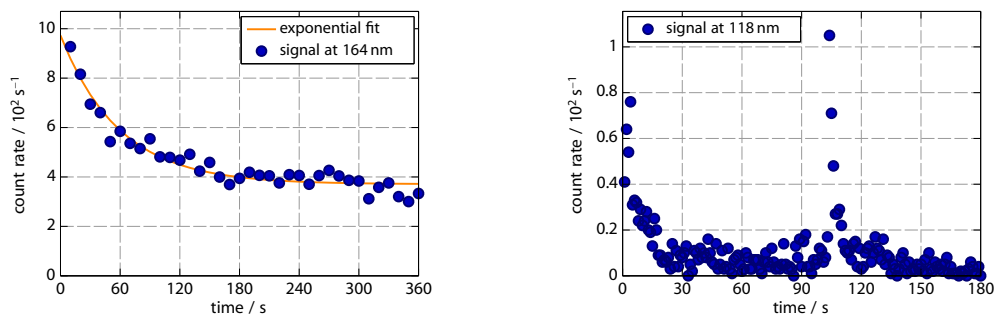
## Field enhancement

Due to the small feed gap size it is difficult to measure the field enhancement directly [Sch10a]. Instead the intensity enhancement is estimated by comparing the measured THG signal from the nano-antennas with that from the bare substrate. Within this estimation the feed gap size is considered to take the limited interaction volume of the nano-antennas into account. Estimated intensity enhancement factors are in the order of 300 for FIB-produced bow tie antennas.

In summary the optical antennas produced with EBL or FIB are resonant for the fundamental laser spectrum and the generated THG signal allows a characterisation of their resonance properties and an estimation of the intensity enhancement. Moreover, the antenna arrays are localised on the sample by measuring a surface map, which allows to individually address different antenna designs.

### 5.2.2 Thermal stability

Despite the spectral antenna properties, their thermal stability is also of major importance for HHG experiments with incident peak intensities in the range of  $10^{11} \text{ W cm}^{-2}$  as outlined in section 3.6. Previous measurements not only indicate third harmonic generation at a surface but also fifth harmonic generation (FHG)



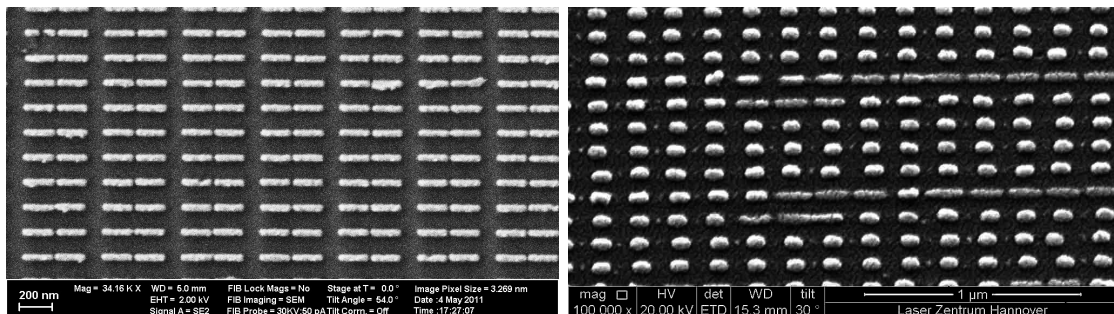
(a) Harmonic signal at 164 nm emitted by EBL-produced nano-antennas.

(b) Signal at 118 nm emitted by nano-antennas fabricated with FIB milling. After 100 s the sample was slightly moved to illuminate a fresh spot.

**Figure 5.10:** Harmonic signal in dependence of illumination time for different fabrication techniques. In both cases the signal drops exponentially and stabilises at a significantly reduced level. This points to an initial change of the original antenna design, which is not altered further.

[Tsa96a]. Higher-order non-linear processes scale strongly with the electric field and thus with the field enhancement of the antennas. Therefore, for instance a reduced field enhancement caused by antenna damage is observed much more easily with processes of higher order than THG. Section 5.4 describes measurements of higher harmonic orders conducted within this thesis in full detail. To characterise the antennas' thermal stability the generated fifth harmonic (i.e. at 164 nm) is used in case of EBL-produced antennas and radiation at 118 nm for those fabricated with FIB milling.

Figure 5.10 shows the harmonic signal at the indicated wavelengths for EBL- and FIB-produced antennas as a function of time. In both cases the harmonic signal decays exponentially and stabilises at a significantly reduced level. So the original antenna design is first changed for instance due to thermal reshaping and then remains in a different shape without further changes [Wan11]. The measurement was started immediately after addressing a new antenna array and briefly maximising the signal. Therefore, the starting time is accurate within a few seconds. This is also illustrated in figure 5.10(b) where the sample was slightly moved after approximately 100s to illuminate a fresh spot within the antenna array. Consequently the harmonic signal increases again until the respective antennas are also changed as before and the signal drops again. To assess the reshaping process, SEM images are taken before and after laser pulse illumination.



(a) Rod-type antennas before illumination      (b) Rod-type antennas after illumination

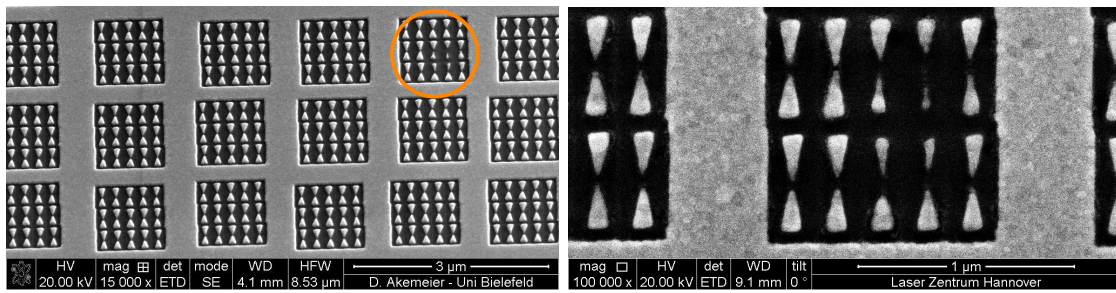
**Figure 5.11:** SEM images of EBL-produced optical antennas before and after illumination. After the fabrication identical rod-type antennas are found on the substrate, whereas after illumination most of the antennas have melted into half spheres of comparable size and only a few rod like structures remain. Additionally a thin organic layer is observed on the sample.

### EBL-produced antennas

Figure 5.11 shows SEM images of EBL-produced rod-type nano-antennas before and after illumination. Before illumination nearly identical optical antennas are found on the substrate as expected. After illumination on the other hand, most of the antennas have melted into half spheres of comparable size and only a few rod structures remain. Moreover, an additional organic layer is found on both the substrate and the antennas. The organic nature of this layer is revealed during the SEM analysis by a significant darkening of the layer. This behaviour occurs in electron microscopy when organic bonds are cracked [Gol03] and can in this case only be caused by oil contamination. The rotating vane pump can be ruled out as source of the contamination because additional oil filters were used at the vacuum side. However, no sample contamination was observed after removing a turbo molecular pump. Unfortunately no further EBL-produced antennas were available after the removal, meaning that the influence of contamination cannot be determined. Nonetheless, melting is obviously the dominating damage process as indicated by the final antenna shape since a half sphere has a significantly lower surface tension than a rod-type antenna.

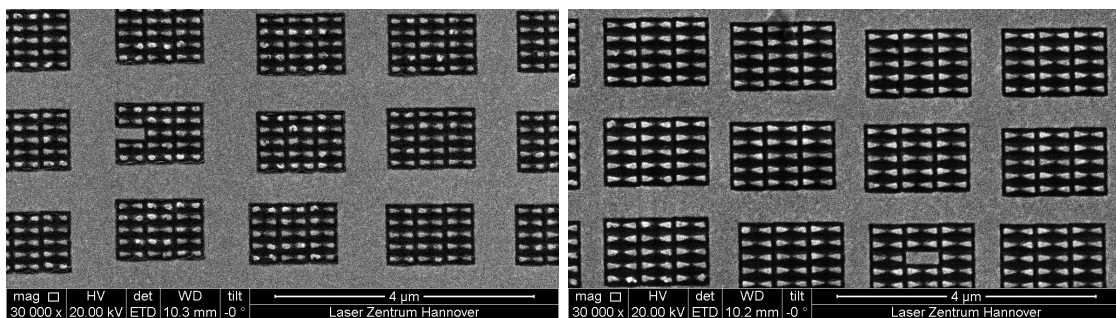
### FIB-produced antennas

Analogous measurements were carried out with FIB-produced bow tie antennas as shown in figure 5.12. Figure 5.12 depicts the antennas after finishing the fabrication process, where some antennas exhibit small features highlighted by the circle, which are caused by imperfections of FIB milling. Due to their small size, these features in particular should be much more sensitive to thermal damage than larger ones. However, like the surrounding antennas they are found to be unchanged after illumination when focussing with a 200 mm and 120 mm achromatic lens as shown in figure 5.12(b). With a tighter focus, i.e. focussing with a 80 mm achromatic lens, slight occasional damage is found for 200 nm antennas and regular damage due to melting for 140 nm ones as shown in figures 5.12(c) and 5.12(d), respectively. This is in agreement with the simulations described in section 3.4, which also showed a damage threshold depending on the antenna length. In further experiments 170 nm antennas were also found to be thermally stable, which validates the qualitative behaviour shown in figures 3.16 and 3.17. Quantitatively, however, differences occur which are caused by the simplicity of the temperature distribution model to solve the diffusion equation. Taking a non-uniform temperature distribution inside the nano-particle into account, the maximum



(a) Bow tie antennas before illumination.

(b) Bow tie antennas after illumination. Laser beam focussed with 200 mm and 120 mm achromatic lens.



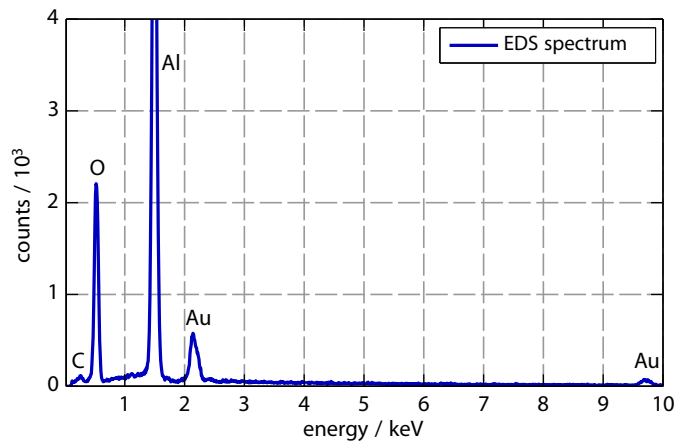
(c) 140 nm antenna arm length after illumination. Laser beam focussed with 80 mm achromatic lens.

(d) 200 nm antenna arm length after illumination. Laser beam focussed with 80 mm achromatic lens.

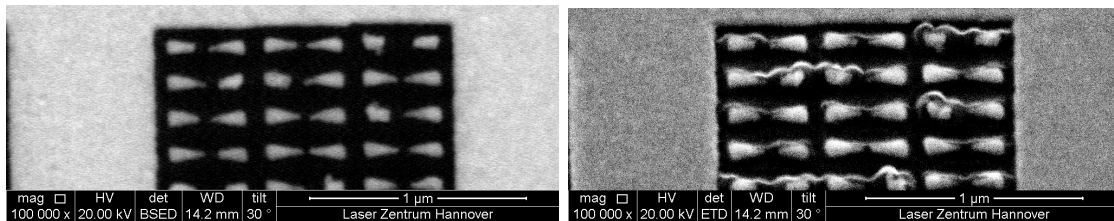
**Figure 5.12:** Bow tie antennas before and after illumination with varying antenna arm lengths and different achromatic lenses used to focus the laser beam. Only above an intensity threshold antenna destruction is observed (c). Additionally the destruction strongly depends on the antenna arm length since 140 nm long antennas are widely damaged (c), whereas only a few 200 nm long antennas are changed (d).

antenna temperature is slightly lowered by approximately 8% [Baf11]. This leads to an increased damage threshold for the antennas, as found in the experiments.

The damaged antennas are depicted at a higher magnification in figure 5.13 using backscattered electrons (figure 5.13(b)) or secondary electrons (figure 5.13(c)), respectively. Since the intensity of the former is mostly dependent on the atomic number, the image reveals material information of the analysed area. Materials with a higher atomic number generally lead to a higher signal, i.e. appear brighter and vice versa. All bright areas in figure 5.13(b) therefore consist of gold, whereas the dark areas represent the substrate material. Secondary electrons on the other hand, are only generated in the top sample layer with a thickness of a few nanometres and hence image the sample's topography. Figure 5.13(c) clearly reveals a strongly non-uniform



(a) Energy dispersive spectrum of the spot shown in (b) and (c). Only peaks associated with gold, aluminium, oxygen and carbon are found, pointing to a damage of the substrate material.



(b) Backscattered electron image resulting in a material contrast. Dark areas represent the substrate and bright areas represent the gold film.

(c) Secondary electron image to obtain information about the sample's topography.

**Figure 5.13:** SEM analysis of damaged antennas with different detectors and energy-dispersive X-ray spectroscopy. According to spectrum (a) no contamination is present in the analysed area, while from (b) the destroyed antennas are clearly visible. (c) reveals information about the sample's topology and points towards a damaged substrate material.

surface in close proximity to the antennas, although the adjacent substrate material is not altered. Additional information about the chemical compounds in the analysed area is gained by energy-dispersive X-ray spectroscopy, where the electron beam leads to the emission of characteristic X-ray radiation. This radiation is then measured with an energy resolved detector to obtain an energy spectrum. Details concerning the detection of different electrons as well as further information about energy-dispersive X-ray spectroscopy are found in [Gol03]. The respective energy spectrum plotted in figure 5.13(a) only contains measurable peaks for gold, aluminium, oxygen and carbon. The latter is caused by handling the sample outside a sealed atmosphere and is low in comparison with the others. Most prominent are the peaks from aluminium and



oxygen, which result from sapphire as a substrate material. Since the antennas only comprise a small part of the whole array, the gold peaks are also low compared with those from e.g. oxygen. Most importantly no other peaks occur and sample contamination is ruled out as a source for the incongruities in the secondary electron picture. From the simulations, peak intensities in the range of  $10^{13} \text{ W cm}^{-2}$  are expected in close proximity to the antennas and in the feed gap. For sapphire, optical breakdown with subsequent shape changes has been observed previously at a threshold intensity of  $(1.4 \pm 0.4) \cdot 10^{13} \text{ W cm}^{-2}$  [Lin96]. The incongruities are therefore most likely caused by a damaged substrate material, resulting in a final topography shown in figure 5.13(c).

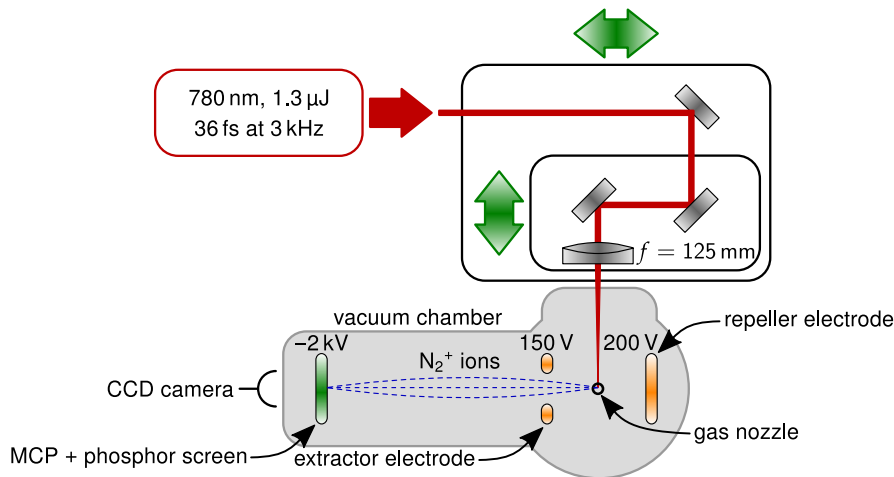
As indicated by the described measurements, thermal damage not only to the antennas but also to the substrate material occurs for the highest peak intensities accessible with the presented experimental apparatus. This is in agreement with previous experiments by Kim et al. [Kim12], who reported an analogous behaviour. Nonetheless, thermally stable antenna designs have been experimentally found in agreement with the previously introduced temperature evolution calculations. Most of the measurements on HHG utilising plasmonic field enhancement are consequently performed with approximately 170 nm antennas, which have been found to be less sensitive to thermal damage.

## 5.3 Gas nozzle

### 5.3.1 Characterisation

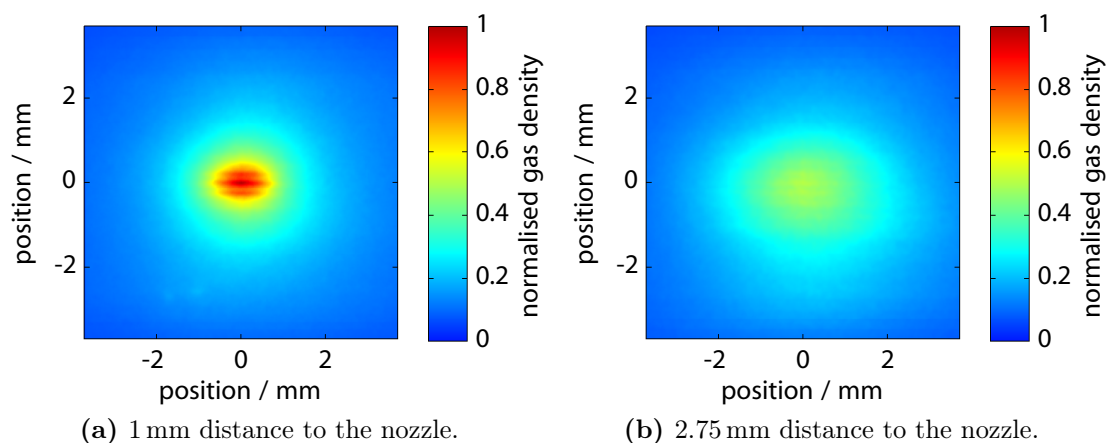
So far the driving laser as well as the nano-antennas have been thoroughly characterised. For THG the number of emitters has a large influence on the signal, since the harmonic intensity scales with the number of contributing atoms squared. As outlined in chapter 4 HHG is usually experimentally realised in gaseous media. For the particular case of HHG in combination with optical antennas a gas jet is used to feed gas onto the sample. To assess the number of atoms contributing to the harmonic signal, the gas nozzle is characterised with a velocity map imaging (VMI) spectrometer [Epp97].

In figure 5.14 the respective setup is sketched, with the gas nozzle placed in the middle between the extractor and the repeller electrode. The gas distribution behind the nozzle is then determined by ionising nitrogen atoms with a laser beam, which are produced by focussing the beam of a commercial chirped pulse amplification (CPA)



**Figure 5.14:** Sketched VMI setup to characterise the gas nozzle used for HHG. Nitrogen atoms are fed into the VMI chamber from different nozzle heights. In the laser focus atoms are ionised and then detected spatially resolved with a MCP. By scanning the laser focus across the gas jet, its spatial distribution is finally reconstructed. Green arrows indicate translation stages.

laser system into the VMI vacuum chamber. The focussing lens itself is mounted on translation stages in  $x$ - and  $y$ -direction (as indicated by the green arrows) to scan the laser focus across the gas jet while detecting the generated ions in a spatially resolved manner with a combination of a phosphorus-coated multi channel plate (MCP) and a sensitive CCD camera. Details about the particular measurement technique and the operation of a VMI spectrometer are found in [Epp97].



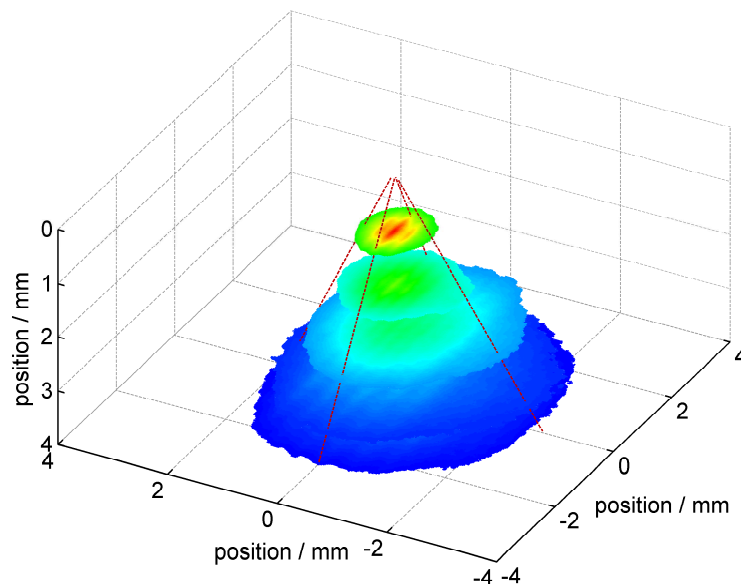
**Figure 5.15:** Reconstructed gas density behind the nozzle for two different distances. Approximately hundred images are used for the reconstruction at each distance. A varying overlap between individual images causes the fringes present in (a). A reduced gas density is clearly seen for larger distances.

Figure 5.15 shows the sum of approximately hundred single images to reconstruct the gas density in the  $xy$ -plane for two different  $z$ -positions. The fringes present in figure 5.15(a) are caused by a varying overlap of the underlying single images for a constant step size in both dimensions. Nonetheless, the resulting gas jet with its spatial distribution is clearly visible with a nearly circular shape. For larger separations from the nozzle, the gas density drops significantly as expected.

For each  $z$ -position the FWHM is determined in  $x$ - and  $y$ -direction, grouped and fitted with a linear function. The intersection of these fit curves then reveals the previously unknown nozzle position. Both the fit curves and the gas density at different  $z$ -positions are plotted in figure 5.16 to illustrate the gas density behind the nozzle. From the fit data a divergence angle of  $33^\circ$  is obtained.

### 5.3.2 Number of atoms at the sample

As pointed out above, the number of atoms contributing to the harmonic signal has a major influence on the harmonic intensity. With the previously determined gas distribution behind the nozzle and a mass flow detector the number of atoms at the sample is accessible. First, the experimental results for the gas density are



**Figure 5.16:** Three dimensional representation of the gas density. The edge of the gas jet is set to the FWHM for each measurement. The dashed lines show a linear fit of the calculated widths from which a divergence angle of  $33^\circ$  is obtained.

approximated by a number of slices with increasing radii. The radius itself is given by the distance to the nozzle and the divergence angle  $\alpha$ . Assuming a slice thickness of 1 nm, the gas density within the slice after time  $\Delta t$  is

$$\rho(z, j_m) = \frac{j_m \Delta t}{m} \frac{1}{\pi z^2 \tan^2 \alpha} \frac{1}{1 \text{ nm}} . \quad (5.1)$$

Here,  $m$  is the atomic or molecular mass of the used gas and  $j_m$  the respective mass flow. For xenon and a divergence angle of  $33^\circ$  the gas density becomes

$$\rho(z, j_m) = 4.3 \cdot 10^{13} \frac{j_m}{z^2} \frac{\text{s}}{\text{g nm}} . \quad (5.2)$$

Equation (5.2) only depends on the mass flow  $j_m$ , which is experimentally determined. A detailed derivation of equations (5.1) and (5.2) is given in [Wal11].

For the particular experiment, typical distances between the sample and the gas nozzle are in the order of 100  $\mu\text{m}$  and the measured mass flow is 0.175 sccm (measured with a MKS 647C controller), which is approximately  $1.7 \cdot 10^{-5} \text{ g s}^{-1}$ . Hence, the gas density at the sample is in the order of  $7.4 \cdot 10^{-2} \text{ atoms/nm}^3$ . Furthermore, for a 50 nm thick bow tie antenna with a gap size of 20 nm the conservatively estimated interaction volume is 20 nm  $\times$  50 nm  $\times$  40 nm leading to  $2.9 \cdot 10^3$  atoms in it. Since roughly 200 antennas are illuminated with the laser pulse, in total  $5.9 \cdot 10^5$  atoms contribute to the harmonic signal.

In case of HHG in a gas jet by far more atoms contribute to the harmonic signal as pointed out by Sivilis et al. [Siv12]. Therefore a reduced harmonic intensity is expected, which for their experimental conditions is estimated as

$$\frac{C_{\text{nano}}}{C_{\text{conv}}} \lesssim 10^{-8} . \quad (5.3)$$

Here,  $C_{\text{nano}}$  and  $C_{\text{conv}}$  denote the conversion efficiency for nano-structure-enhanced and conventional HHG respectively. Kim et al. [Kim12] on the other hand, report  $\sim 8 \cdot 10^4$  gas atoms in the interaction volume and therefore reach a ratio of  $10^{-4}$ . Although the interaction volume was estimated more conservatively for the calculations above, almost ten times more atoms contribute to the harmonic signal in the experiments presented in this thesis and the ratio thus becomes  $7 \cdot 10^{-4}$ . Using the same interaction volume as Kim et al., the ratio increases even to  $10^{-2}$  and nano-structure enhanced HHG should well be possible.

## 5.4 Harmonic generation

Figure 5.17 sketches the experimental setup for nano-antenna enhanced HHG experiments. The principal design is equivalent to the one used for characterising the antennas introduced earlier. Additionally gas is fed onto the sample via the gas nozzle previously characterised. The nozzle can be tilted backwards and forwards as well as left and right to optimise the alignment between the gas jet and the laser focus. Again, the laser focus plays the role of the entrance slit of the monochromator to maximise the collection efficiency as for other high-repetition-rate or early HHG experiments [Li89; Lin03]. The THG signal generated is detected with the known PMT, whereas higher harmonic orders are measured with an electron multiplier (Photonis 4751G-CsI) in combination with a photon counter (Stanford Research SR400). The electron multiplier is coated with caesium iodide to increase the quantum efficiency to around 20% over a wide spectral range [Bur10]. By flipping a mirror into the harmonic beam and setting the monochromator to the appropriate wavelength, it is possible to easily switch between HHG and THG signal detection. This allows for the addressing of

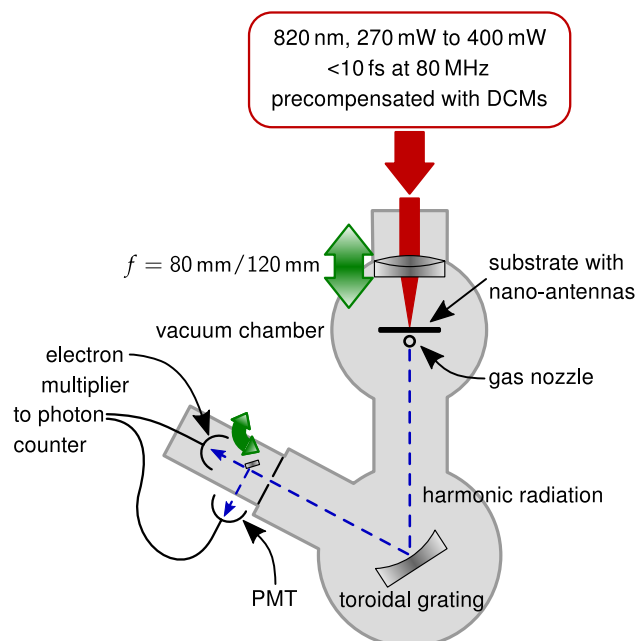


**Figure 5.17:** Sketched experimental setup for nano-antenna enhanced HHG. The principal design is equivalent to the THG setup in figure 5.17. Additionally, gas is fed onto the sample through a gas nozzle. For alignment purposes it is possible to switch between a detection with the PMT and an electron multiplier. Both detectors are connected to a photon counter.

different antenna arrays during the experiments as well as alignment cross checks. To cover the whole spectral range of interest, the toroidal grating can be switched between one designed for 110 nm to 310 nm and a second one for 20 nm to 220 nm. The latter has twice as many grooves (2400 grooves/mm) as the first one, though, and for mechanical reasons only a spectral range from 20 nm to 110 nm is accessible. Nonetheless, via a combination of both gratings, a broad spectral range is covered. In the following, all spectra and photon numbers are corrected for the diffraction efficiency and the detection efficiency of the respective grating and detector unless otherwise stated. Moreover the spectral resolution of the monochromator is taken into account to obtain a spectral density from the measured count rates.

#### 5.4.1 Low harmonic orders

Figure 5.18 shows the generated harmonic spectrum of EBL-produced rod-type optical antennas. It is corrected for the detection efficiency set by the grating and the electron multiplier and was taken under vacuum conditions with a background pressure of  $1 \cdot 10^{-6}$  mbar. The harmonic orders of the driving laser are indicated by grey background shading, with the fifth harmonic located at 164 nm and the seventh at

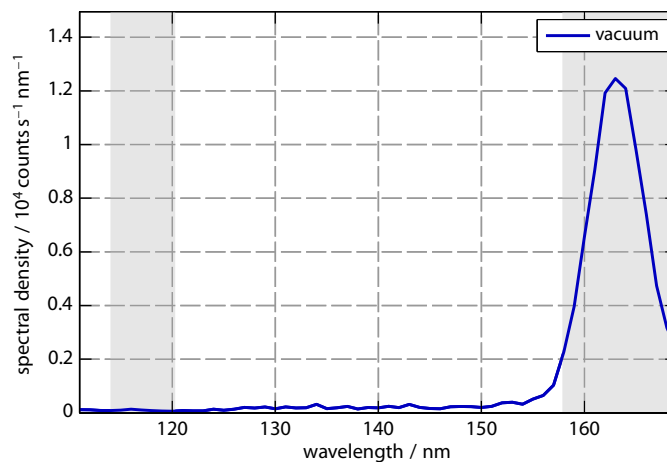


**Figure 5.18:** Measured spectrum using rod-type optical antennas, which are produced with EBL. Grey background shading indicates harmonic orders of the driving laser, where the width is determined from the fundamental laser spectrum. The incident intensity is in the order of  $10^{11}$  W cm<sup>-2</sup> and a strong fifth harmonic signal is found without feeding gas onto the sample. The radiation is therefore generated at the substrate's surface. In agreement with perturbation theory no higher harmonic orders are found.

117 nm. The width of the shading is determined from the fundamental laser spectrum. A pronounced peak is measured at the fifth harmonic, which reveals a ratio of  $10^{-5}$  in comparison with peak signals from THG measurements. This is identical to previously reported results [Tsa96a] and confirms the perturbative behaviour of the generation process. Moreover, the harmonic signal also originates from the surface as no gas was fed onto the sample.

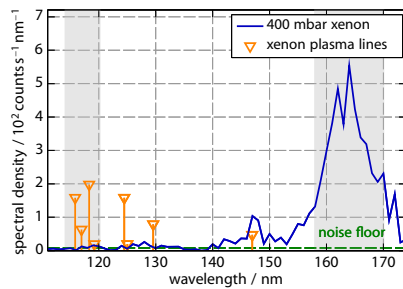
No radiation is measured at the seventh harmonic order, which is in agreement with perturbation theory.

#### 5.4.2 Higher harmonic orders and fluorescence

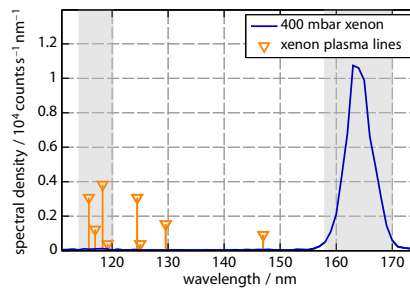
##### EBL-produced nano-antennas

A measured spectrum also using rod-type optical antennas and feeding xenon gas with a backing pressure of 400 mbar onto the sample is plotted in figure 5.19(a). The high backing pressure in this experiment is due to a smaller nozzle size as compared to the one characterised in section 5.3. The background pressure in the main experimental chamber is  $5 \cdot 10^{-5}$  mbar and  $1 \cdot 10^{-6}$  mbar at the electron multiplier. Grey background shading indicates the harmonic orders of the driving laser, whereas the orange lines represent xenon plasma lines and their respective relative intensities [San05]. The green dashed line shows the noise floor caused by dark counts from the electron multiplier.

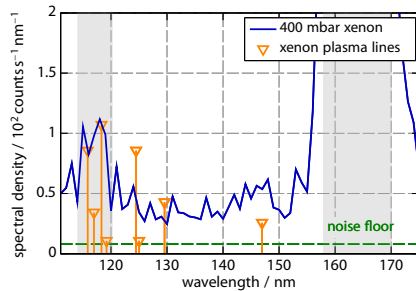
A significant fifth harmonic signal is measured at 164 nm, although it is two orders of magnitude smaller than in the previous measurement. Additionally a signal six times smaller is found at 147 nm, which vanishes as soon as the gas flow is turned off and therefore does not originate from the surface, but from the interaction of the enhanced laser field with the xenon atoms. In general, the total photon flux is only in the order of  $10^2 \text{ s}^{-1} \text{ nm}^{-1}$ , which is mainly caused by thermal destruction processes analysed in more detail in section 5.2.2. These limit the integration time and lead to a maximum spectral resolution of one nanometre in the measured spectra. Nonetheless, the peak at 147 nm is resolved and belongs to the  $6s \rightarrow 5p$  transition in neutral xenon, demonstrating a spectral resolution high enough to detect isolated atomic lines in the spectrum. The difference in the FHG signal in figures 5.19(a) and 5.18 points to a considerable difference in the local field enhancement for the respective nano-antennas.



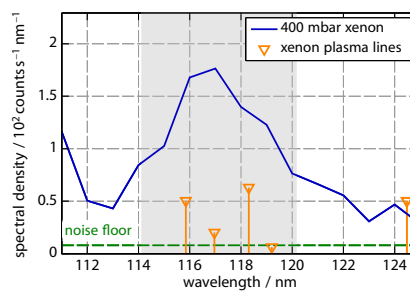
(a) Fifth harmonic and fluorescence from the  $6s \rightarrow 5p$  transition in neutral xenon.



(b) Measured spectrum in xenon with 400 mbar backing pressure.



(c) Measured spectrum in xenon with 400 mbar backing pressure and an enlarged  $y$ -axis.



(d) Detail scan between 111 nm and 125 nm to circumvent thermal destruction processes.

**Figure 5.19:** Measured spectra in xenon with rod-type nano-antennas at a backing pressure of 400 mbar. Grey background shading indicates harmonic orders of the driving laser, whereas orange lines represent xenon plasma lines and their respective relative intensities. Green dashed lines show the noise floor set by dark counts from the electron multiplier. Apart from the fifth harmonic, all spectral features require a xenon gas flow and are attributed to discrete transitions in neutral and single ionised xenon atoms.

Figures 5.19(b) and 5.19(c) show a spectrum taken with a different sample under equivalent conditions to the previous experiment with different  $y$ -axis scales to highlight weaker features in the spectrum. Here, the total photon flux for the fifth harmonic is in the order of  $10^4 \text{ s}^{-1} \text{ nm}^{-1}$ , pointing to an increased field enhancement. Additionally a signal two orders of magnitude lower is found around 117 nm, i.e. at the spectral position of the seventh harmonic. Again the signal vanishes as soon as the gas flow is turned off and the green dashed line in figure 5.19(c) represents the noise floor from the electron multiplier.

Early experiments on HHG with intensities of  $3 \cdot 10^{13} \text{ W cm}^{-2}$  reported fluorescence contributions from neutral and ionised xenon to their spectrum [Li89] or even nearly identical photon numbers for the harmonic radiation and the atomic line emission [LHu91]. Surprisingly, the emission from the  $6s \rightarrow 5p$  transition in neutral xenon



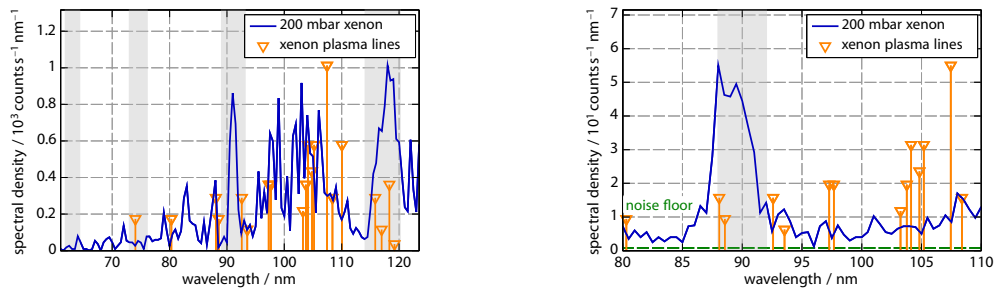
is less pronounced in figure 5.19(c) than in figure 5.19(a) and the spectral features cannot be directly assigned to discrete transitions in neutral xenon or  $\text{Xe}^+$  ions. Since the integration time is still limited by destruction issues, a small spectral range from 111 nm to 125 nm was measured separately and is plotted in figure 5.19(d), with the green dashed line indicating the noise floor. The xenon plasma line at 119 nm corresponds to a transition in neutral xenon, whereas the others belong to transitions in  $\text{Xe}^+$ .

Due to the spectral resolution, different atomic lines are not resolved in the spectrum. Nonetheless, the overall shape points to a superposition of the individual contributions. Moreover a strong transition in  $\text{Xe}^+$  is located at 110 nm, which fits well to the measured spectrum. Experiments on tunnel ionisation in noble gases have found an intensity threshold of approximately  $6 \cdot 10^{13} \text{ W cm}^{-2}$  for the generation of  $\text{Xe}^+$  ions [Aug89] and laser intensity effects in the energy distribution of electrons produced in multiphoton ionisation were observed for intensities of roughly  $1 \cdot 10^{13} \text{ W cm}^{-2}$  [Lom85]. Although the radiation around 117 nm is most likely caused by fluorescence and not by harmonic generation, the spectra point to an enhanced laser intensity in the range of  $10^{13} \text{ W cm}^{-2}$ , i.e. a field enhancement of at least two orders of magnitude. Thus, the laser intensities necessary for high-order harmonic generation are in this case reached with the optical antennas used, despite thermal destruction processes which limit the overall performance.

In conclusion, antennas facilitating a higher photon flux are necessary to measure with an increased spectral resolution and enable further experiments. Spatial coherence measurements, for example, give additional information on the origin of the radiation generated, since harmonic generation is a coherent process with a well-defined beam profile. Higher photon fluxes have been obtained with FIB-produced nano-antennas and the respective results are described in the following.

#### FIB-produced nano-antennas

In figure 5.20, exemplary spectra for 200 nm bow tie antennas are plotted with sub-figure (a) covering a broader spectral range and sub-figure (b) showing a detail scan around 90 nm. For both spectra xenon gas with a backing pressure of 200 mbar was fed onto the sample and the nozzle position has been optimised. The nozzle is identical to the one characterised in section 5.3. Grey background shading indicates the harmonic orders of the driving laser and orange lines represent xenon plasma lines and their



(a) Measured spectrum in xenon with 200 mbar backing pressure.

(b) Detail scan between 80 nm and 110 nm at a different fundamental wavelength. (spectrum is not efficiency corrected)

**Figure 5.20:** Measured spectra in xenon with 200 nm bow tie antennas at a backing pressure of 200 mbar. Grey background shading indicates harmonic orders of the driving laser, whereas orange lines represent xenon plasma lines and their respective relative intensities. Radiation from multiple plasma lines is found around 104 nm (a). Surprisingly, these contributions do not show up at a different central wavelength of the driving laser, which is shown in (b).

relative intensities [San05]. In general, the photon flux is at least an order of magnitude higher than in previous measurements. Moreover, the antennas were less affected by thermal damage due to their increased length. Most strikingly, high photon numbers are detected between 100 nm and 110 nm, which is attributed to multiple plasma lines in this spectral range. A pronounced peak with the highest photon numbers is found at 117 nm, where only four plasma lines can contribute to the total signal. Taking the relative intensities into account and comparing the photon numbers with those at 104 nm a lower signal is expected if plasma radiation alone is its source. Another spectral peak coincides with the spectral position of the ninth harmonic at 91 nm. However, the spectral width is smaller than expected for the harmonic radiation.

Due to different laser parameters, i.e. centred around 810 nm instead of 820 nm, the alignment was cross-checked, which requires the grating with a design wavelength from 110 nm to 310 nm. Therefore, no diffraction efficiency is known for the spectral range below 110 nm and the spectrum in figure 5.20(b) has not been corrected for it. As before, the dashed green line indicates the noise floor caused by dark counts from the electron multiplier. Interestingly no plasma line contributions for wavelengths larger than 95 nm are found in the spectrum. However, a pronounced peak at 90 nm is present, which does not directly coincide with xenon plasma lines.

Additional spectra were taken under identical conditions as before with 170 nm antennas to maximise the electric field enhancement as pointed out in section 3.6.

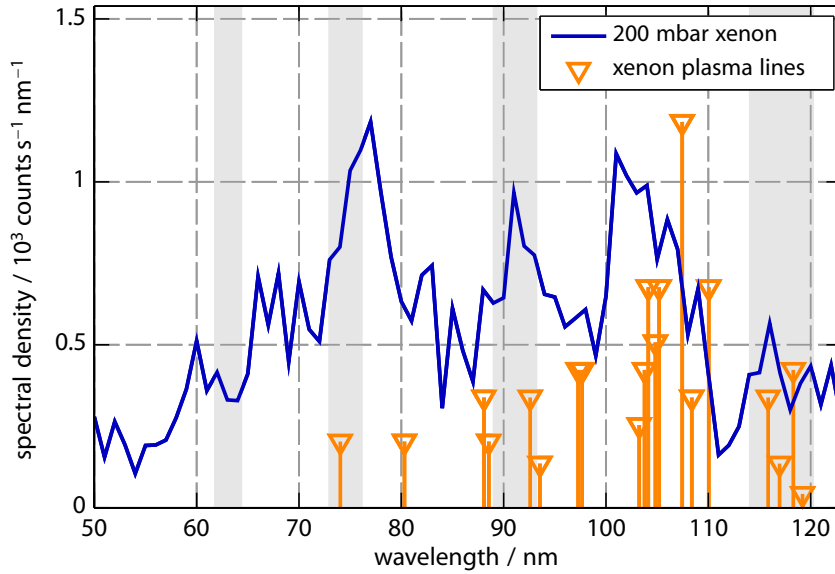
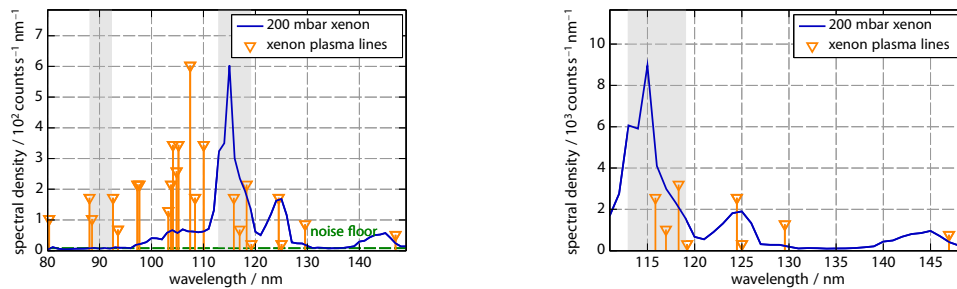


**Figure 5.21:** Measured spectra in xenon with 170 nm long bow tie antennas at a backing pressure of 200 mbar. Again, radiation from multiple plasma lines is found around 104 nm, but surprisingly few photons are detected around 117 nm. The highest photon numbers occur at 76 nm, which is close to the eleventh harmonic of the driving laser.

The central laser wavelength is 820 nm as expected and figure 5.21 shows an efficiency-corrected spectrum in the range between 50 nm and 120 nm to detect higher harmonic orders. As before, significant photon numbers are detected around 104 nm, which result from discrete transitions in single-ionised xenon [San05]. Surprisingly few photons are measured at 117 nm, though. The highest photon numbers are found at 76 nm, which is close to the spectral position of the eleventh harmonic. Slightly less signal is present at 91 nm, i.e. at the ninth harmonic order.

To distinguish between harmonic radiation and fluorescence in the spectra, detailed measurements at the spectral position of the seventh harmonic were performed. For alignment purposes and additional cross-checks, these were again performed with the grating designed for 110 nm to 310 nm. Both the resulting efficiency-corrected and the uncorrected spectrum are shown in figure 5.22. The green dashed line in figure 5.20(a) indicates the known noise floor and atomic line contributions at 147 nm and 125 nm match to the measured spectrum well. Additionally, a sharp spectral peak occurs at 117 nm with higher photon numbers than expected from plasma radiation alone. Multiple plasma lines around 104 nm lead to a shoulder, which drops off at 100 nm.



(a) Spectrum without correcting for the diffraction efficiency of the grating.

(b) Diffraction efficiency corrected spectrum.

**Figure 5.22:** Measured spectra in xenon with 170 nm long bow tie antennas at a backing pressure of 200 mbar. Again radiation from multiple plasma lines is found around 104 nm. The highest photon numbers occur at 117 nm, which is close to the seventh harmonic of the driving laser. Spectral features at 125 nm and 147 nm can be directly assigned to discrete transitions in xenon.

Due to the low diffraction efficiency of the grating in this spectral range, the photon numbers are relatively low, but still significant since they lie above the noise floor.

In summary, the spectra obtained with FIB-produced nano-antennas are all in contrast to data reported by Kim et al. [Kim08], who claim to have observed harmonic radiation alone without additional lines resulting from plasma radiation in an identical experiment. They are however in agreement with early experiments on HHG with peak intensities of  $3 \cdot 10^{13} \text{ W cm}^{-2}$ , where contributions from neutral and single-ionised xenon to the spectra have been found [LHu91; Li89]. These intensities are well within reach in the feed gap of the nano-antennas and atomic line emission as an incoherent process is likely to occur. This is supported by the observed changes to the sapphire substrate, which require peak intensities of at least  $1 \cdot 10^{13} \text{ W cm}^{-2}$  as outlined in section 5.2.2 in order to appear. An insufficient field enhancement from the nano-antennas as a possible source of error is therefore highly unlikely. Moreover, atomic line emission alone has been found in independent experiments on HHG in the presence of optical antennas, which further confirms the measured spectra [Siv12].

However, particularly figures 5.20(b) and 5.22 contain hints for harmonic generation as well. Because the harmonic radiation and some xenon plasma lines are emitted at the same wavelength, a spectral analysis alone cannot resolve the origin of the generated photons. Unfortunately this is also the case for krypton, which has a similar ionisation potential as xenon. Atomic line emission and HHG on the other hand differ strongly in terms of their spatial coherence properties. Since HHG is a coherent process, a

well-defined beam profile is expected, whereas atomic line emission is incoherent and therefore uniformly distributed. Additional measurements to resolve the spatial profile of the emitted radiation are thus introduced below.

### 5.4.3 Beam profile measurements

The earlier introduced setup for HHG has been extended and is sketched in figure 5.23. For clarity, all known parts are left out. The beam profile measurements itself are performed with a razor blade, which is mounted on a translation stage and scanned across the exit slit of the monochromator as indicated by the green circle. The harmonic signal is then recorded as a function of the blade position either with the electron multiplier or the PMT.

A typical measurement of the third harmonic signal and an error function fit are plotted in figure 5.24(a). The fit resembles the data well and reveals a beam radius of 1.2 mm. Figure 5.24(b) shows the corresponding beam profile along the exit slit of the monochromator.

Unfortunately, technical defects prevented measurements for higher harmonic orders or atomic lines so far. In particular the vacuum feedthrough for the translation stage caused pressure changes at the electron multiplier of approximately one order of magnitude. These led to an electric breakdown with possible damage to the electron multiplier. Therefore, the origin of the generated radiation currently remains an open question. Measurements with the third harmonic demonstrate the experimental feasibility of the technique though, and with a modified design additional insight is envisaged.

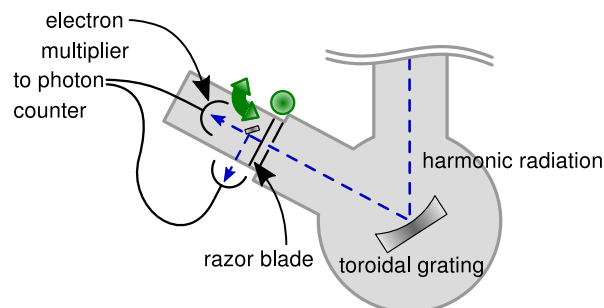
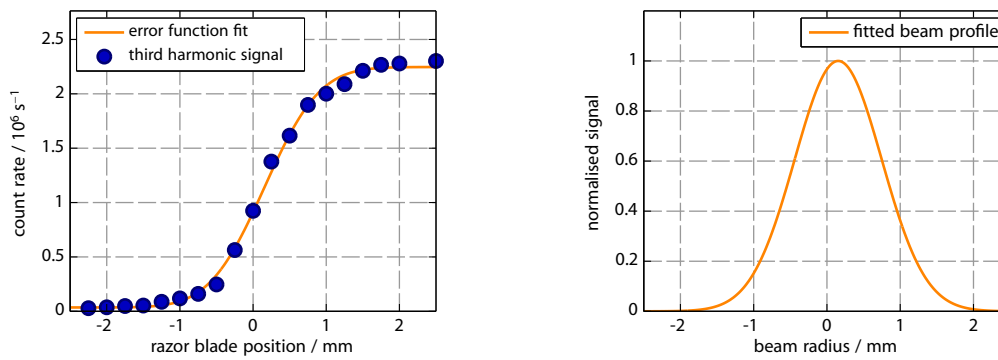


**Figure 5.23:** Sketched experimental setup for beam profile measurements in the UV. A razor blade is attached to a translation stage to scan it along the exit slit of the monochromator.



(a) Measured data and fitted error function to determine the beam radius of the third harmonic.

(b) Fitted beam profile for the third harmonic signal.

**Figure 5.24:** Beam profile measurement of the third harmonic revealing a beam radius of 1.2 mm.

# CHAPTER 6

---

## Summary and Outlook

---

In this thesis, optical antennas and their suitability for nano-structure enhanced high-order harmonic generation (HHG) were analysed both numerically and experimentally. The necessary peak intensities for HHG have been reached in experiments and measured spectra have been shown to contain indications for harmonic generation in noble gases.

Numerical simulations based on the finite difference time domain (FDTD) method provided a detailed understanding of nano-antennas and are in good agreement with experimental results. In particular, thermal damage processes have been found to limit the antenna performance in experiments. Consequently, these processes have been included into the modelling and a length depending intensity threshold was predicted for bow tie antennas. This also enabled an optimisation of these antennas with respect to the near-field intensity enhancement while avoiding thermal damage. An antenna length slightly off resonance proved to be best in this case and an optimal antenna design with a length of 160 nm, an opening angle of  $30^\circ$ , a gap size of 20 nm, and a thickness of 30 nm has been found.

Additionally, the phase-matching conditions for nano-structure-enhanced HHG were also analysed numerically to assess possible phase-matching effects. On the relevant length scale of the antenna thickness, perfect phase-matching was found for experimentally feasible harmonic orders. This has two major consequences: First, phase-matching effects do not limit the generation of high-order harmonics. Secondly, an independent observation of the microscopic and the macroscopic response in HHG is envisaged which offers the possibility of improving existing theoretical models of the HHG process.

To verify the obtained numerical results experimentally, a compact and versatile scientific apparatus was developed. Based on the third harmonic radiation generated at the surface, the optical antennas were thoroughly characterised and a significant intensity enhancement has been found. Estimated intensity enhancement factors are in the order of 300 for focussed ion beam (FIB)-produced bow tie antennas, i.e. peak intensities of  $10^{13} \text{ W cm}^{-2}$  are feasible. In separate measurements, peak intensities in the range of  $10^{13} \text{ W cm}^{-2}$  to  $10^{14} \text{ W cm}^{-2}$  emerged, which is sufficient for HHG. Moreover, the numerically-predicted dependence of the intensity threshold on the antenna length was observed experimentally and is qualitatively in good agreement with the performed simulations. As expected, the optimised bow tie antenna design was not thermally destroyed and also produced the highest photon fluxes. Thus, the optical antennas are well-described by the simulations and also proved to work well in experiments.

For measurements on high-order harmonics, the gas jet used was characterised to gain access to the number of atoms contributing to the harmonic signal. The divergence angle and the mass flow were determined experimentally resulting in approximately  $2.9 \cdot 10^3$  atoms per antenna feed gap. This number is more than ten times larger than previously anticipated in comparable experiments [Kim12].

The measured spectra on nano-structure-enhanced HHG contain contributions from various spectral lines originating from neutral and single-ionised xenon. The necessary peak intensities for high-order harmonic generation have therefore clearly been reached in the experiments. Additionally, the spectral peaks found match harmonics of the driving laser, but are also in close proximity to those from atomic transitions. Therefore, the observed features could not unambiguously be attributed to HHG or atomic line emission, via spectral measurements alone.

## Outlook

Currently, there is renewed interest in this field with interesting prospects and several ideas for future experiments exist. Most importantly, additional measurements on the spatial profile of the generated radiation will allow the distinguishment of HHG from atomic line emission. A successful verification of HHG would open up new intriguing experiments on frequency combs in the extreme ultraviolet regime.

To achieve this goal, further improvements to the experimental setup can be made. For instance, an additional sapphire layer coated on top of the antennas after the



fabrication process could help to thermally stabilise the antennas. This would potentially increase the damage threshold and higher intensity enhancement factors are envisaged, thus helping to increase the total photon flux. Moreover, antennas produced from single crystalline gold flakes have nearly perfect edges and hence a reduced damping is expected. This in turn should lead to an increased intensity enhancement. Alternatively, the fundamental wavelength can be shifted into the infrared spectral region. Resonant antennas are larger there, which makes it easier to manufacture them according to the design parameters. Secondly, all materials for plasmonic applications behave more like ideal metals in that spectral range, also leading to reduced losses. Antennas produced from single crystalline gold flakes, which are designed for the infrared, are therefore the most promising candidates for a significantly increased intensity enhancement.

Other improvements aim at an increased number of atoms fed at the sample to increase the total photon flux. This could either be achieved by further optimising the gas nozzle or by switching to a different concept altogether. One possible approach is to use a gas cell to significantly increase the gas pressure at the sample and hence the number of atoms. However, the gas propagates co-linearly with the harmonics generated and also towards the detector, which can lead to absorption. In solid state materials on the other hand, the atom density is naturally orders of magnitude higher than in gases. By focussing onto a fused silica substrate with a peak intensity of  $8 \cdot 10^{13} \text{ W cm}^{-2}$  harmonics up to the eleventh order have already been observed [Rau07]. Moreover, low-order harmonics have already been generated at the surface of the substrate as shown in chapter 5. Hence, by changing to a setup where the harmonics are generated in reflection rather than in transmission and the optical antennas are embedded into a material such as sapphire or fused silica, for example, high-order harmonic generation seems feasible.



---

## Bibliography

---

- [Arb03] A. Arbouet, C. Voisin, D. Christofilos, P. Langot, N. D. Fatti, F. Vallée, J. Lermé, G. Celep, E. Cottancin, M. Gaudry, M. Pellarin, M. Broyer, M. Maillard, M. P. Pileni, and M. Treguer: *Electron-Phonon Scattering in Metal Clusters*. Phys. Rev. Lett. **90** (17 2003), p. 177401.
- [Aug89] S. Augst, D. Strickland, D. D. Meyerhofer, S. L. Chin, and J. H. Eberly: *Tunneling ionization of noble gases in a high-intensity laser field*. Phys. Rev. Lett. **63** (20 1989), pp. 2212–2215.
- [Baf10] G. Baffou, C. Girard, and R. Quidant: *Mapping Heat Origin in Plasmonic Structures*. Phys. Rev. Lett. **104**, 13 (2010), p. 136805.
- [Baf11] G. Baffou and H. Rigneault: *Femtosecond-pulsed optical heating of gold nanoparticles*. Phys. Rev. B **84**, 3 (2011), p. 035415.
- [Bal97] P. Balcou, P. Salières, A. L’Huillier, and M. Lewenstein: *Generalized phase-matching conditions for high harmonics: The role of field-gradient forces*. Phys. Rev. A **55** (4 1997), pp. 3204–3210.
- [Bar03] W. L. Barnes, A. Dereux, and T. W. Ebbesen: *Surface plasmon subwavelength optics*. Nature **424**, 6950 (2003), pp. 824–830.
- [Bar08] E. S. Barnard, J. S. White, A. Chandran, and M. L. Brongersma: *Spectral properties of plasmonic resonator antennas*. Opt. Express **16**, 21 (2008), pp. 16529–16537.
- [Bar97] Y. Barad, H. Eisenberg, M. Horowitz, and Y. Silberberg: *Nonlinear scanning laser microscopy by third harmonic generation*. Applied Physics Letters **70**, 8 (1997), pp. 922–924.
- [Bec07] B. R. Beck, J. A. Becker, P. Beiersdorfer, G. V. Brown, K. J. Moody, J. B. Wilhelmy, F. S. Porter, C. A. Kilbourne, and R. L. Kelley: *Energy Splitting of the Ground-State Doublet in the Nucleus  $^{229}\text{Th}$* . Phys. Rev. Lett. **98** (2007), p. 142501.
- [Ber94] J.-P. Berenger: *A perfectly matched layer for the absorption of electromagnetic waves*. Journal of Computational Physics **114**, 2 (1994), pp. 185–200.

- [Boh07] C. F. Bohren and D. R. Huffman: *Absorption and Scattering of Light by Small Particles*. Wiley-VCH Verlag GmbH, 2007.
- [Boy03] R. W. Boyd: *Nonlinear Optics*. Academic Press, 2003.
- [Bro07] M. L. Brongersma and P. G. Kik, eds.: *Surface Plasmon Nanophotonics*. Vol. 131. Springer Series in Optical Sciences. Springer, 2007.
- [Bur10] Burle: *Channeltron electron multiplier handbook for mass spectrometry applications*. Burle. 2010.
- [Cai07] W. Cai, U. K. Chettiar, A. V. Kildishev, and V. M. Shalaev: *Optical cloaking with metamaterials*. Nat. Photon. **1**, 4 (2007), pp. 224–227.
- [Cha99] S.-S. Chang, C.-W. Shih, C.-D. Chen, W.-C. Lai, and C. R. C. Wang: *The Shape Transition of Gold Nanorods*. Langmuir **15**, 3 (1999), pp. 701–709.
- [Cia12] M. F. Ciappina, J. Biegert, R. Quidant, and M. Lewenstein: *High-order-harmonic generation from inhomogeneous fields*. Phys. Rev. A **85** (3 2012), p. 033828.
- [Cin12] A. Cingoz, D. C. Yost, T. K. Allison, A. Ruehl, M. E. Fermann, I. Hartl, and J. Ye: *Direct frequency comb spectroscopy in the extreme ultraviolet*. Nature **482**, 7383 (2012), pp. 68–71.
- [Cor93] P. B. Corkum: *Plasma perspective on strong field multiphoton ionization*. Phys. Rev. Lett. **71**, 13 (1993), pp. 1994–1997.
- [Cro03] K. B. Crozier, A. Sundaramurthy, G. S. Kino, and C. F. Quate: *Optical antennas: Resonators for local field enhancement*. Journal of Applied Physics **94**, 7 (2003), pp. 4632–4642.
- [Cub06] E. Cubukcu, E. A. Kort, K. B. Crozier, and F. Capasso: *Plasmonic laser antenna*. Applied Physics Letters **89**, 9, 093120 (2006), p. 093120.
- [Cub08] E. Cubukcu, N. Yu, E. Smythe, L. Diehl, K. Crozier, and F. Capasso: *Plasmonic Laser Antennas and Related Devices*. Selected Topics in Quantum Electronics, IEEE Journal of **14**, 6 (2008), pp. 1448–1461.
- [Dit02] H. Ditlbacher, J. R. Krenn, G. Schider, A. Leitner, and F. R. Aussenegg: *Two-dimensional optics with surface plasmon polaritons*. Applied Physics Letters **81**, 10 (2002), pp. 1762–1764.
- [Dor09] J. Dorfmueller, R. Vogelgesang, R. T. Weitz, C. Rockstuhl, C. Etrich, T. Pertsch, F. Lederer, and K. Kern: *Fabry-Pérot Resonances in One-Dimensional Plasmonic Nanostructures*. Nano Letters **9**, 6 (2009), pp. 2372–2377.
- [Dor10] J. Dorfmueller, R. Vogelgesang, W. Khunsin, C. Rockstuhl, C. Etrich, and K. Kern: *Plasmonic Nanowire Antennas: Experiment, Simulation, and Theory*. Nano Letters **10**, 9 (2010), pp. 3596–3603.
- [Dra94] B. T. Draine and P. J. Flatau: *Discrete-dipole approximation for scattering calculations*. J. Opt. Soc. Am. A **11**, 4 (1994), pp. 1491–1499.

- [Dre01] M. Drescher, M. Hentschel, R. Kienberger, G. Tempea, C. Spielmann, G. A. Reider, P. B. Corkum, and F. Krausz: *X-ray Pulses Approaching the Attosecond Frontier*. *Science* **291**, 5510 (2001), pp. 1923–1927.
- [Epp97] A. T. J. B. Eppink and D. H. Parker: *Velocity map imaging of ions and electrons using electrostatic lenses: Application in photoelectron and photofragment ion imaging of molecular oxygen*. *Review of Scientific Instruments* **68**, 9 (1997), pp. 3477–3484.
- [Fan06] W. Fan, S. Zhang, N.-C. Panouiu, A. Abdenour, S. Krishna, R. M. Osgood, K. J. Malloy, and S. R. J. Brueck: *Second Harmonic Generation from a Nanopatterned Isotropic Nonlinear Material*. *Nano Letters* **6**, 5 (2006), pp. 1027–1030.
- [Fei08] E. Feigenbaum and M. Orenstein: *Ultrasmall Volume Plasmons, yet with Complete Retardation Effects*. *Phys. Rev. Lett.* **101** (16 2008), p. 163902.
- [Fer88] M. Ferray, A. L’Huillier, X. F. Li, L. A. Lompre, G. Mainfray, and C. Manus: *Multiple-harmonic conversion of 1064 nm radiation in rare gases*. *Journal of Physics B: Atomic, Molecular and Optical Physics* **21**, 3 (1988), p. L31.
- [Fra61] P. A. Franken, A. E. Hill, C. W. Peters, and G. Weinreich: *Generation of Optical Harmonics*. *Phys. Rev. Lett.* **7** (4 1961), pp. 118–119.
- [Fro04] D. P. Fromm, A. Sundaramurthy, P. J. Schuck, G. Kino, and W. E. Moerner: *Gap-Dependent Optical Coupling of Single "Bowtie" Nanoantennas Resonant in the Visible*. *Nano Letters* **4**, 5 (2004), pp. 957–961.
- [Fun09] A. M. Funston, C. Novo, T. J. Davis, and P. Mulvaney: *Plasmon Coupling of Gold Nanorods at Short Distances and in Different Geometries*. *Nano Letters* **9**, 4 (2009), pp. 1651–1658.
- [Goh05] C. Gohle, T. Udem, M. Herrmann, J. Rauschenberger, R. Holzwarth, H. A. Schuessler, F. Krausz, and T. W. Hänsch: *A frequency comb in the extreme ultraviolet*. *Nature* **436**, 7048 (2005), pp. 234–237.
- [Gol03] J. Goldstein: *Scanning electron microscopy and X-ray microanalysis*. Vol. 1. Springer, 2003.
- [Gou08] E. Goulielmakis, M. Schultze, M. Hofstetter, V. S. Yakovlev, J. Gagnon, M. Uiberacker, A. L. Aquila, E. M. Gullikson, D. T. Attwood, R. Kienberger, F. Krausz, and U. Kleineberg: *Single-Cycle Nonlinear Optics*. *Science* **320**, 5883 (2008), pp. 1614–1617.
- [Gru03] P. Grua, J. P. Morreeuw, H. Bercegol, G. Jonusauskas, and F. Vallée: *Electron kinetics and emission for metal nanoparticles exposed to intense laser pulses*. *Phys. Rev. B* **68** (3 2003), p. 035424.

- [Han09] T. Hanke, G. Krauss, D. Träutlein, B. Wild, R. Bratschitsch, and A. Leitenstorfer: *Efficient Nonlinear Light Emission of Single Gold Optical Antennas Driven by Few-Cycle Near-Infrared Pulses*. Phys. Rev. Lett. **103**, 25 (2009), p. 257404.
- [Han11] G. Han, D. Weber, F. Neubrech, I. Yamada, M. Mitome, Y. Bando, A. Pucci, and T. Nagao: *Infrared spectroscopic and electron microscopic characterization of gold nanogap structure fabricated by focused ion beam*. Nanotechnology **22**, 27 (2011), p. 275202.
- [Han12] T. Hanke, J. Cesar, V. Knittel, A. Trügler, U. Hohenester, A. Leitenstorfer, and R. Bratschitsch: *Tailoring Spatiotemporal Light Confinement in Single Plasmonic Nanoantennas*. Nano Letters **12**, 2 (2012), pp. 992–996.
- [Hei91] T. Heinz: ‘Nonlinear Surface Electromagnetic Phenomena’. Ed. by H.-E. Ponath and G. Stegeman. Elsevier, 1991. Chap. Second-Order Nonlinear Optical Effects at Surfaces and Interfaces, pp. 353–416.
- [Hir03] L. R. Hirsch, R. J. Stafford, J. A. Bankson, S. R. Sershen, B. Rivera, R. E. Price, J. D. Hazle, N. J. Halas, and J. L. West: *Nanoshell-mediated near-infrared thermal therapy of tumors under magnetic resonance guidance*. Proceedings of the National Academy of Sciences **100**, 23 (2003), pp. 13549–13554.
- [Hod99] J. H. Hodak, A. Henglein, and G. V. Hartland: *Size dependent properties of Au particles: Coherent excitation and dephasing of acoustic vibrational modes*. The Journal of Chemical Physics **111**, 18 (1999), pp. 8613–8621.
- [Hu02] M. Hu and G. V. Hartland: *Heat Dissipation for Au Particles in Aqueous Solution: Relaxation Time versus Size*. The Journal of Physical Chemistry B **106**, 28 (2002), pp. 7029–7033.
- [Hua07] W. Huang, W. Qian, M. A. El-Sayed, Y. Ding, and Z. L. Waong: *Effect of the Lattice Crystallinity on the Electron-Phonon Relaxation Rates in Gold Nanoparticles*. The Journal of Physical Chemistry C **111**, 29 (2007), pp. 10751–10757.
- [Hua10a] J.-S. Huang, V. Callegari, P. Geisler, C. Brüning, J. Kern, J. C. Prangma, X. Wu, T. Feichtner, J. Ziegler, P. Weinmann, M. Kamp, A. Forchel, P. Biagioni, U. Sennhauser, and B. Hecht: *Atomically flat single-crystalline gold nanostructures for plasmonic nanocircuitry*. Nat. Commun. **1** (2010), pp. 150–.
- [Hua10b] J.-S. Huang, J. Kern, P. Geisler, P. Weinmann, M. Kamp, A. Forchel, P. Biagioni, and B. Hecht: *Mode Imaging and Selection in Strongly Coupled Nanoantennas*. Nano Letters **10**, 6 (2010), pp. 2105–2110.
- [Hus11] A. Husakou, S.-J. Im, and J. Herrmann: *Theory of plasmon-enhanced high-order harmonic generation in the vicinity of metal nanostructures in noble gases*. Phys. Rev. A **83**, 4 (2011), p. 043839.

- [Ino98] H. Inouye, K. Tanaka, I. Tanahashi, and K. Hirao: *Ultrafast dynamics of nonequilibrium electrons in a gold nanoparticle system*. Phys. Rev. B **57** (18 1998), pp. 11334–11340.
- [Jac98] J. D. Jackson: *Classical Electrodynamics*. 3rd ed. John Wiley & Sons, 1998.
- [Jin02] J. Jin, J. Jin, and J. Jin: *The finite element method in electromagnetics*. 2nd. John Wiley & Sons, 2002.
- [Joh72] P. B. Johnson and R. W. Christy: *Optical Constants of the Noble Metals*. Phys. Rev. B **6** (12 1972), pp. 4370–4379.
- [Jon05] R. J. Jones, K. D. Moll, M. J. Thorpe, and J. Ye: *Phase-Coherent Frequency Combs in the Vacuum Ultraviolet via High-Harmonic Generation inside a Femtosecond Enhancement Cavity*. Phys. Rev. Lett. **94**, 19 (2005), p. 193201.
- [Jos91] R. M. Joseph, S. C. Hagness, and A. Taflov: *Direct time integration of Maxwell's equations in linear dispersive media with absorption for scattering and propagation of femtosecond electromagnetic pulses*. Opt. Lett. **16**, 18 (1991), pp. 1412–1414.
- [Kan10] D. Z. Kandula, C. Gohle, T. J. Pinkert, W. Ubachs, and K. S. E. Eikema: *Extreme Ultraviolet Frequency Comb Metrology*. Phys. Rev. Lett. **105**, 6 (2010), p. 063001.
- [Kas90] T. Kashiwa and I. Fukai: *A treatment by the FD-TD method of the dispersive characteristics associated with electronic polarization*. Microwave and Optical Technology Letters **3**, 6 (1990), pp. 203–205.
- [Kim08] S. Kim, J. Jin, Y.-J. Kim, I.-Y. Park, Y. Kim, and S.-W. Kim: *High-harmonic generation by resonant plasmon field enhancement*. Nature **453**, 7196 (2008), pp. 757–760.
- [Kim12] S. Kim, J. Jin, Y.-J. Kim, I.-Y. Park, Y. Kim, and S.-W. Kim: *Kim et al. reply*. Nature **485**, 7397 (2012), E1–E3.
- [Koc05] J. Koch, F. Korte, T. Bauer, C. Fallnich, A. Ostendorf, and B. Chichkov: *Nanotexturing of gold films by femtosecond laser-induced melt dynamics*. Applied Physics A: Materials Science & Processing **81** (2 2005), pp. 325–328.
- [Kor03] F. Korte, J. Serbin, J. Koch, A. Egbert, C. Fallnich, A. Ostendorf, and B. Chichkov: *Towards nanostructuring with femtosecond laser pulses*. Applied Physics A: Materials Science & Processing **77** (2 2003), pp. 229–235.
- [Kra09] F. Krausz and M. Ivanov: *Attosecond physics*. Rev. Mod. Phys. **81** (1 2009), pp. 163–234.
- [Kra92] J. L. Krause, K. J. Schafer, and K. C. Kulander: *High-order harmonic generation from atoms and ions in the high intensity regime*. Phys. Rev. Lett. **68** (24 1992), pp. 3535–3538.

- [Kre68] E. Kretschmann and H. Raether: *Radiative decay of non radiative surface plasmons excited by light*. Zeitschrift für Naturforschung, Teil A **23** (1968), p. 2135.
- [Kun93] K. Kunz and R. Luebbers: *The finite difference time domain method for electromagnetics*. CRC, 1993.
- [Leo07] U. Leonhardt: *Optical metamaterials: Invisibility cup*. Nat. Photon. **1**, 4 (2007), pp. 207–208.
- [Lew94] M. Lewenstein, P. Balcou, M. Y. Ivanov, A. L’Huillier, and P. B. Corkum: *Theory of high-harmonic generation by low-frequency laser fields*. Phys. Rev. A **49** (3 1994), pp. 2117–2132.
- [LHu91] A. L’Huillier, K. J. Schafer, and K. C. Kulander: *Theoretical aspects of intense field harmonic generation*. Journal of Physics B: Atomic, Molecular and Optical Physics **24**, 15 (1991), p. 3315.
- [LHu93] A. L’Huillier and P. Balcou: *High-order harmonic generation in rare gases with a 1-ps 1053-nm laser*. Phys. Rev. Lett. **70** (6 1993), pp. 774–777.
- [Li89] X. F. Li, A. L’Huillier, M. Ferray, L. A. Lompré, and G. Mainfray: *Multiple-harmonic generation in rare gases at high laser intensity*. Phys. Rev. A **39** (11 1989), pp. 5751–5761.
- [Lin03] F. Lindner, W. Stremme, M. G. Schätzel, F. Grasbon, G. G. Paulus, H. Walther, R. Hartmann, and L. Strüder: *High-order harmonic generation at a repetition rate of 100 kHz*. Phys. Rev. A **68**, 1 (2003), p. 013814.
- [Lin96] D. von der Linde and H. Schüler: *Breakdown threshold and plasma formation in femtosecond laser–solid interaction*. J. Opt. Soc. Am. B **13**, 1 (1996), pp. 216–222.
- [Lin99a] S. Link, C. Burda, M. B. Mohamed, B. Nikoobakht, and M. A. El-Sayed: *Laser Photothermal Melting and Fragmentation of Gold Nanorods: Energy and Laser Pulse-Width Dependence*. The Journal of Physical Chemistry A **103**, 9 (1999), pp. 1165–1170.
- [Lin99b] S. Link, C. Burda, Z. L. Wang, and M. A. El-Sayed: *Electron dynamics in gold and gold–silver alloy nanoparticles: The influence of a nonequilibrium electron distribution and the size dependence of the electron–phonon relaxation*. The Journal of Chemical Physics **111**, 3 (1999), pp. 1255–1264.
- [Lom85] L. A. Lompré, A. L’Huillier, G. Mainfray, and C. Manus: *Laser-intensity effects in the energy distributions of electrons produced in multiphoton ionization of rare gases*. J. Opt. Soc. Am. B **2**, 12 (1985), pp. 1906–1912.
- [Lou70] R. Loudon: *The propagation of electromagnetic energy through an absorbing dielectric*. Journal of Physics A: General Physics **3**, 3 (1970), p. 233.



- [Lue90] R. Luebbers, F. Hunsberger, K. Kunz, R. Standler, and M. Schneider: *A frequency-dependent finite-difference time-domain formulation for dispersive materials*. *Electromagnetic Compatibility, IEEE Transactions on* **32**, 3 (1990), pp. 222–227.
- [Mai07] S. A. Maier: *Plasmonics: fundamentals and applications*. Springer, 2007.
- [Mar04] A. Marian, M. C. Stowe, J. R. Lawall, D. Felinto, and J. Ye: *United Time-Frequency Spectroscopy for Dynamics and Global Structure*. *Science* **306**, 5704 (2004), pp. 2063–2068.
- [McP87] A. McPherson, G. Gibson, H. Jara, U. Johann, T. S. Luk, I. A. McIntyre, K. Boyer, and C. K. Rhodes: *Studies of multiphoton production of vacuum-ultraviolet radiation in the rare gases*. *J. Opt. Soc. Am. B* **4**, 4 (1987), pp. 595–601.
- [Mer08] J. Merlein, M. Kahl, A. Zuschlag, A. Sell, A. Halm, J. Boneberg, P. Leiderer, A. Leitenstorfer, and R. Bratschitsch: *Nanomechanical control of an optical antenna*. *Nat. Photon.* **2**, 4 (2008), pp. 230–233.
- [Mil05] T. A. Milligan: *Modern Antenna Design*. John Wiley & Sons, Inc., 2005.
- [Müh05] P. Mühschlegel, H.-J. Eisler, O. J. F. Martin, B. Hecht, and D. W. Pohl: *Resonant Optical Antennas*. *Science* **308**, 5728 (2005), pp. 1607–1609.
- [Nor04] P. Nordlander, C. Oubre, E. Prodan, K. Li, and M. I. Stockman: *Plasmon Hybridization in Nanoparticle Dimers*. *Nano Letters* **4**, 5 (2004), pp. 899–903.
- [Nov07] L. Novotny: *Effective Wavelength Scaling for Optical Antennas*. *Phys. Rev. Lett.* **98** (26 2007), p. 266802.
- [Nov94] L. Novotny and C. Hafner: *Light propagation in a cylindrical waveguide with a complex, metallic, dielectric function*. *Phys. Rev. E* **50** (5 1994), pp. 4094–4106.
- [Osk10] A. F. Oskooi, D. Roundy, M. Ibanescu, P. Bermel, J. Joannopoulos, and S. G. Johnson: *Meep: A flexible free-software package for electromagnetic simulations by the FDTD method*. *Computer Physics Communications* **181**, 3 (2010), pp. 687–702.
- [Ott68] A. Otto: *Excitation of nonradiative surface plasma waves in silver by the method of frustrated total reflection*. *Zeitschrift für Physik A Hadrons and Nuclei* **216** (1968), pp. 398–410.
- [Oza08] A. Ozawa, J. Rauschenberger, C. Gohle, M. Herrmann, D. R. Walker, V. Pervak, A. Fernandez, R. Graf, A. Apolonski, R. Holzwarth, F. Krausz, T. W. Hänsch, and T. Udem: *High Harmonic Frequency Combs for High Resolution Spectroscopy*. *Phys. Rev. Lett.* **100**, 25 (2008), p. 253901.
- [Pal98] E. Palik and G. Ghosh: *Handbook of optical constants of solids*. Vol. 3. Academic press, 1998.

- [Pan89] L. Pan, K. T. Taylor, and C. W. Clark: *High-harmonic generation in hydrogenic ions*. Phys. Rev. A **39** (9 1989), pp. 4894–4897.
- [Pei03] E. Peik and C. Tamm: *Nuclear laser spectroscopy of the 3.5 eV transition in Th-229*. EPL (Europhysics Letters) **61**, 2 (2003), p. 181.
- [Pro03] E. Prodan, C. Radloff, N. J. Halas, and P. Nordlander: *A Hybridization Model for the Plasmon Response of Complex Nanostructures*. Science **302**, 5644 (2003), pp. 419–422.
- [Rae88] H. Raether: *Surface plasmons*. Springer, 1988.
- [Rak98] A. D. Rakic, A. B. Djurišić, J. M. Elazar, and M. L. Majewski: *Optical Properties of Metallic Films for Vertical-Cavity Optoelectronic Devices*. Appl. Opt. **37**, 22 (1998), pp. 5271–5283.
- [Rau07] J. Rauschenberger: ‘Phase-stabilized Ultrashort Laser Systems for Spectroscopy’. PhD thesis. Ludwig Maximilians Universität München, 2007.
- [Rec03] W. Rechberger, A. Hohenau, A. Leitner, J. Krenn, B. Lamprecht, and F. Aussenegg: *Optical properties of two interacting gold nanoparticles*. Optics Communications **220**, 1–3 (2003), pp. 137–141.
- [Roo99] L. Roos, E. Constant, E. Mével, P. Balcou, D. Descamps, M. B. Gaarde, A. Valette, R. Haroutunian, and A. L’Huillier: *Controlling phase matching of high-order harmonic generation by manipulating the fundamental field*. Phys. Rev. A **60** (6 1999), pp. 5010–5018.
- [Rup02] R. Ruppin: *Electromagnetic energy density in a dispersive and absorptive material*. Physics Letters A **299**, 2-3 (2002), pp. 309–312.
- [Sal95] P. Salières, A. L’Huillier, and M. Lewenstein: *Coherence Control of High-Order Harmonics*. Phys. Rev. Lett. **74** (19 1995), pp. 3776–3779.
- [Sam91] J. R. Sambles, G. W. Bradbery, and F. Yang: *Optical excitation of surface plasmons: An introduction*. Contemporary Physics **32**, 3 (1991), pp. 173–183.
- [San05] J. E. Sansonetti and W. C. Martin: *Handbook of Basic Atomic Spectroscopic Data*. Journal of Physical and Chemical Reference Data **34**, 4 (2005), pp. 1559–2259.
- [Sch02] J. M. Schins, T. Schrama, J. Squier, G. J. Brakenhoff, and M. Müller: *Determination of material properties by use of third-harmonic generation microscopy*. J. Opt. Soc. Am. B **19**, 7 (2002), pp. 1627–1634.
- [Sch05] P. J. Schuck, D. P. Fromm, A. Sundaramurthy, G. S. Kino, and W. E. Moerner: *Improving the Mismatch between Light and Nanoscale Objects with Gold Bowtie Nanoantennas*. Phys. Rev. Lett. **94** (1 2005), p. 017402.
- [Sch09] O. Schwartz and D. Oron: *Background-Free Third Harmonic Imaging of Gold Nanorods*. Nano Letters **9**, 12 (2009), pp. 4093–4097.

- [Sch10a] M. Schnell, A. Garcia-Etxarri, J. Alkorta, J. Aizpurua, and R. Hillenbrand: *Phase-Resolved Mapping of the Near-Field Vector and Polarization State in Nanoscale Antenna Gaps*. *Nano Letters* **10**, 9 (2010), pp. 3524–3528.
- [Sch10b] J. A. Schuller, E. S. Barnard, W. Cai, Y. C. Jun, J. S. White, and M. L. Brongersma: *Plasmonics for extreme light concentration and manipulation*. *Nat. Mater.* **9**, 3 (2010), pp. 193–204.
- [Sch97] K. J. Schafer and K. C. Kulander: *High Harmonic Generation from Ultrafast Pump Lasers*. *Phys. Rev. Lett.* **78** (4 1997), pp. 638–641.
- [Sha07] V. M. Shalaev: *Optical negative-index metamaterials*. *Nat. Photon.* **1**, 1 (2007), pp. 41–48.
- [Siv12] M. Siviş, M. Duwe, B. Abel, and C. Ropers: *Nanostructure-enhanced atomic line emission*. *Nature* **485**, 7397 (2012), E1–E3.
- [Sko11] E. Skopalová, D. Y. Lei, T. Witting, C. Arrell, F. Frank, Y. Sonnefraud, S. A. Maier, J. W. G. Tisch, and J. P. Marangos: *Numerical simulation of attosecond nanoplasmonic streaking*. *New Journal of Physics* **13**, 8 (2011), p. 083003.
- [Søn08] T. Søndergaard, J. Beermann, A. Boltasseva, and S. I. Bozhevolnyi: *Slow-plasmon resonant-nanostrip antennas: Analysis and demonstration*. *Phys. Rev. B* **77** (11 2008), p. 115420.
- [Ste11] S. L. Stebbings, F. Süßmann, Y.-Y. Yang, A. Scrinzi, M. Durach, A. Rusina, M. I. Stockman, and M. F. Kling: *Generation of isolated attosecond extreme ultraviolet pulses employing nanoplasmonic field enhancement: optimization of coupled ellipsoids*. *New Journal of Physics* **13**, 7 (2011), p. 073010.
- [Su03] K.-H. Su, Q.-H. Wei, X. Zhang, J. J. Mock, D. R. Smith, and S. Schultz: *Interparticle Coupling Effects on Plasmon Resonances of Nanogold Particles*. *Nano Letters* **3**, 8 (2003), pp. 1087–1090.
- [Sul92] D. Sullivan: *Frequency-dependent FDTD methods using Z transforms*. *Antennas and Propagation, IEEE Transactions on* **40**, 10 (1992), pp. 1223–1230.
- [Sun05] A. Sundaramurthy, K. B. Crozier, G. S. Kino, D. P. Fromm, P. J. Schuck, and W. E. Moerner: *Field enhancement and gap-dependent resonance in a system of two opposing tip-to-tip Au nanotriangles*. *Phys. Rev. B* **72**, 16 (2005), p. 165409.
- [Taf05] A. Taflove and S. C. Hagness: *Computational Electrodynamics: The Finite-Difference Time-Domain Method*. 3rd. Artech House, 2005.
- [Taf80] A. Taflove: *Application of the Finite-Difference Time-Domain Method to Sinusoidal Steady-State Electromagnetic-Penetration Problems*. *Electromagnetic Compatibility, IEEE Transactions on* **22**, 3 (1980), pp. 191–202.

- [Tam11] T. H. Taminiau, F. D. Stefani, and N. F. van Hulst: *Optical Nanorod Antennas Modeled as Cavities for Dipolar Emitters: Evolution of Sub- and Super-Radiant Modes*. Nano Letters **11**, 3 (2011), pp. 1020–1024.
- [Tom05] H. Tompkins and E. Irene: *Handbook of ellipsometry*. William Andrew, 2005.
- [Trä07] F. Träger, ed.: *Springer Handbook of Lasers and Optics*. 1st ed. Springer Handbook. Springer, 2007.
- [Tsa95] T. Y. F. Tsang: *Optical third-harmonic generation at interfaces*. Phys. Rev. A **52**, 5 (1995), pp. 4116–4125.
- [Tsa96a] T. Tsang: *Third- and fifth-harmonic generation at the interfaces of glass and liquids*. Phys. Rev. A **54** (6 1996), pp. 5454–5457.
- [Tsa96b] T. Y. F. Tsang: *Surface-plasmon-enhanced third-harmonic generation in thin silver films*. Opt. Lett. **21**, 4 (1996), pp. 245–247.
- [Tse08] A. A. Tseng: *Nanofabrication: fundamentals and applications*. World Scientific Publishing, 2008.
- [Ude02] T. Udem, R. Holzwarth, and T. W. Hänsch: *Optical frequency metrology*. Nature **416**, 6877 (2002), pp. 233–237.
- [Val08] G. D. Valle, T. Sondergaard, and S. I. Bozhevolnyi: *Plasmon-polariton nano-stripresonators: from visible to infra-red*. Opt. Express **16**, 10 (2008), pp. 6867–6876.
- [Ver08] E. Verhagen, A. Polman, and L. ( Kuipers: *Nanofocusing in laterally tapered plasmonic waveguides*. Opt. Express **16**, 1 (2008), pp. 45–57.
- [Via05] A. Vial, A.-S. Grimault, D. Macías, D. Barchiesi, and M. L. de la Chapelle: *Improved analytical fit of gold dispersion: Application to the modeling of extinction spectra with a finite-difference time-domain method*. Phys. Rev. B **71** (8 2005), p. 085416.
- [Wag98] C. Wagner and J. Schneider: *Divergent fields, charge, and capacitance in FDTD simulations*. Microwave Theory and Techniques, IEEE Transactions on **46**, 12 (1998), pp. 2131 –2136.
- [Wal11] C. Waltermann: ‘Erzeugung harmonischer Strahlung an plasmonischen Nanoantennen’. MA thesis. Leibniz Universität Hannover, 2011.
- [Wan06] F. Wang and Y. R. Shen: *General Properties of Local Plasmons in Metal Nanostructures*. Phys. Rev. Lett. **97** (20 2006), p. 206806.
- [Wan11] J. Wang, Y. Chen, X. Chen, J. Hao, M. Yan, and M. Qiu: *Photothermal reshaping of gold nanoparticles in a plasmonic absorber*. Opt. Express **19**, 15 (2011), pp. 14726–14734.
- [Wit05] S. Witte, R. T. Zinkstok, W. Ubachs, W. Hogervorst, and K. S. E. Eikema: *Deep-Ultraviolet Quantum Interference Metrology with Ultrashort Laser Pulses*. Science **307**, 5708 (2005), pp. 400–403.

- [Yee66] K. Yee: *Numerical solution of initial boundary value problems involving maxwell's equations in isotropic media*. Antennas and Propagation, IEEE Transactions on **14**, 3 (1966), pp. 302–307.
- [Yos09] D. C. Yost, T. R. Schibli, J. Ye, J. L. Tate, J. Hostetter, M. B. Gaarde, and K. J. Schafer: *Vacuum-ultraviolet frequency combs from below-threshold harmonics*. Nat. Phys. **5**, 11 (2009), pp. 815–820.
- [You01] J. Young and R. Nelson: *A summary and systematic analysis of FDTD algorithms for linearly dispersive media*. Antennas and Propagation Magazine, IEEE **43**, 1 (2001), pp. 61–126.
- [Zin06] R. T. Zinkstok, S. Witte, W. Ubachs, W. Hogervorst, and K. S. E. Eikema: *Frequency comb laser spectroscopy in the vacuum-ultraviolet region*. Phys. Rev. A **73**, 6 (2006), p. 061801.
- [Zoh08] T. Zohdi and P. Wriggers: *An introduction to computational micromechanics*. Vol. 20. Springer Verlag, 2008.



---

## List of Figures

---

1.1	Lycurgus cup . . . . .	1
2.1	Comparison Drude-Sommerfeld model with experimental data . . . . .	9
2.2	Dielectric functions for different metals . . . . .	11
2.3	Surface Plasmon Polartion at a dielectric/metal interface . . . . .	12
2.4	Surface Plasmon Polartion at a dielectric/metal interface . . . . .	13
2.5	Spherical antenna . . . . .	14
2.6	Single-wire antenna . . . . .	16
2.7	Field enhancement around a single-wire antenna . . . . .	18
2.8	Dimer wire antenna . . . . .	19
2.9	Coupling of two wire antennas . . . . .	20
2.10	Field enhancement Dimer antenna . . . . .	21
3.1	Yee-lattice for FDTD . . . . .	24
3.2	Simulation geometry for transmission spectrum calculations . . . . .	28
3.3	Dielectric function of gold in MEEP . . . . .	29
3.4	Transmission spectra for rod-type optical antennas . . . . .	31
3.5	Simulation geometry for intensity enhancement calculations . . . . .	33
3.6	Near-field intensity distribution for a rod-type antenna . . . . .	35
3.7	Near-field intensity distribution for a bow tie antenna . . . . .	36
3.8	Simulation geometry for temperature distribution calculations . . . . .	37
3.9	Heat source density of a rod-type two-wire antenna . . . . .	38
3.10	Heat source density of a bow tie antenna . . . . .	39
3.11	Temperature evolution for an incident intensity of $1 \cdot 10^{11} \text{ W cm}^{-2}$ . . . . .	44
3.12	Temperature evolution for an incident intensity of $2 \cdot 10^{11} \text{ W cm}^{-2}$ . . . . .	45
3.13	Bow tie antenna parameters . . . . .	45
3.14	Intensity enhancement at the middle of the gap as a function of the gap size $g$ . . . . .	46
3.15	Parameter scan bow tie antennas . . . . .	47
3.16	Maximal antenna temperature for different incident intensities as a function of the antenna length $L$ . . . . .	48
3.17	Temperature optimisation of bow tie antennas . . . . .	48

4.1	Harmonic signal amplitude in dependence of the normalised confocal parameter . . . . .	53
4.2	Low-order harmonic generation at an interface with a tightly focussed laser beam . . . . .	53
4.3	Third harmonic signal dependence on the focus position . . . . .	54
4.4	Sketched high-order harmonic spectrum . . . . .	55
4.5	Semi-classical model of high-order harmonic generation . . . . .	56
4.6	Dipole strength and dipole phase of the seventh harmonic in xenon . . . . .	59
4.7	Phase-matching map for different harmonic orders . . . . .	61
4.8	Overview of phase-matching along the propagation axis . . . . .	62
5.1	Schematic representation of electron beam lithography . . . . .	67
5.2	Schematic representation of focussed ion beam milling . . . . .	68
5.3	SEM images of produced nano-antennas . . . . .	68
5.4	Sketched optical setup for harmonic experiments . . . . .	70
5.5	Laser spectrum and corresponding IAC trace . . . . .	70
5.6	Experimental setup for experiments on third harmonic generation . . . . .	71
5.7	Third harmonic signal in dependence of laser power and focus position . . . . .	73
5.8	Surface maps to locate individual antenna arrays . . . . .	74
5.9	Third harmonic spectrum for different antenna arm lengths . . . . .	75
5.10	Thermal stability of illuminated nano-antennas . . . . .	76
5.11	EBL-produced optical antennas before and after illumination. . . . .	77
5.12	Antenna destruction as a function of incident intensity and antenna arm length . . . . .	79
5.13	Detailed SEM analysis of damaged antennas . . . . .	80
5.14	Sketched VMI setup for a gas nozzle characterisation . . . . .	82
5.15	Reconstructed gas density behind the nozzle . . . . .	82
5.16	3d representation of the gas density . . . . .	83
5.17	Sketched experimental setup for nano-antenna enhanced HHG . . . . .	85
5.18	Fifth harmonic spectrum . . . . .	86
5.19	Spectra in xenon with EBL-manufactured nano-antennas . . . . .	88
5.20	Spectra in xenon with FIB milling manufactured 200 nm bow tie antennas . . . . .	90
5.21	Spectrum in xenon with FIB milling manufactured 170 nm bow tie antennas . . . . .	91
5.22	Detailed spectra in xenon using 170 nm long bow tie antennas . . . . .	92
5.23	Sketched experimental setup for beam profile measurements in the UV . . . . .	93
5.24	Beam profile of the third harmonic . . . . .	94



---

## List of Tables

---

3.1 Physical constants of used metals and substrate materials . . . . .	44
4.1 Simulation parameters to analyse phase-matching conditions . . . . .	61
5.1 Focal spot sizes for different achromatic lenses and corresponding peak intensities. . . . .	72



---

## Publications

---

### Scientific publications

1. MARTIN SIEGEL, **NILS PFULLMANN**, GUIDO PALMER, THOMAS BINHAMMER, MILUTIN KOVACEV AND UWE MÖRGNER: ‘Microjoule pulse energy from a chirped-pulse Ti:Sapphire oscillator with cavity dumping’. *Opt. Lett.* (2009), Vol. 34: p. 740-742.

### Contributions at international conferences

1. MARTIN SIEGEL, **NILS PFULLMANN**, STEFAN RAUSCH, THOMAS BINHAMMER, GUIDO PALMER, AND UWE MÖRGNER: ‘Microjoule pulse energy from a chirped-pulse Ti:Sapphire oscillator with cavitydumping’. *Advanced Solid-State Photonics*. Optical Society of America, 2009: paper WE3.
2. MARTIN SIEGEL, **NILS PFULLMANN**, STEFAN RAUSCH, THOMAS BINHAMMER, GUIDO PALMER, AND UWE MÖRGNER: ‘Microjoule pulse energy from a chirped-pulse Ti:Sapphire oscillator with cavitydumping’. *CLEO/Europe and EQEC 2009 Conference Digest*. Optical Society of America, 2009: paper CA7.5.
3. **NILS PFULLMANN**, MARTIN SIEGEL, STEFAN RAUSCH, THOMAS BINHAMMER AND UWE MÖRGNER: ‘Cryogenically Cooled cw-Pumped Double-Pass Ti:sapphire Amplifier Emitting  $\mu$ J Pulse Energies’. *Conference on Lasers and Electro-Optics*. Optical Society of America, 2010: paper CTuK2.
4. **NILS PFULLMANN**, CHRISTIAN WALTERMANN, MILUTIN KOVACEV, TOBIAS HANKE, RUDOLF BRATSCHITSCH, ALFRED LEITENSTORFER AND UWE MÖRGNER: ‘Generation of Harmonics utilising plasmonic field enhancement in gold nanoantennas’. *Symposium of Attoscience and Ultrafast Quantum Control*. Imperial College London. 2011.
5. **NILS PFULLMANN**, CHRISTIAN WALTERMANN, MILUTIN KOVACEV, VANESSA KNITTEL, RUDOLF BRATSCHITSCH, ALFRED LEITENSTORFER AND UWE MÖRGNER: ‘Analysis of Gold Nanoantennas for Harmonic Generation Utilising

Plasmonic Field Enhancement'. *High Intensity Lasers and High field Phenomena*. Optical Society of America, 2012: paper JT2A.58.

## Contributions at national conferences

1. MARTIN SIEGEL, GUIDO PALMER, **NILS PFULLMANN**, ANDY STEINMANN AND UWE MORGNER: 'Theoretische und experimentelle Limits von modengekoppelten Scheibenlasern mit Cavity-Dumping'. *Verhandlungen*. DPG. Darmstadt, 2008.
2. MARTIN SIEGEL, **NILS PFULLMANN**, GUIDO PALMER, FLORIAN SCHEWE AND UWE MORGNER: 'Titan-Saphir Laseroszillator mit Mikrojoule Pulsenergie'. *Verhandlungen*. DPG. Hamburg, 2009.
3. **NILS PFULLMANN**, MARTIN SIEGEL AND UWE MORGNER: 'Kryogene Nachverstärkung von  $\mu\text{J}$ -Laserpulsen'. *Verhandlungen*. DPG. Hamburg, 2009.
4. **NILS PFULLMANN**, MARTIN SIEGEL, CARSTEN CLEVER AND UWE MORGNER: 'Kryogener Doppelpass-Verstärker mit  $\mu\text{J}$ -Pulsenergien'. *Verhandlungen*. DPG. Hannover, 2010.
5. **NILS PFULLMANN**, CARSTEN CLEVER, CHRISTIAN WALTERMANN, MILUTIN KOVACEV, TOBIAS HANKE, RUDOLF BRATSCHITSCH, ALFRED LEITENSTORFER AND UWE MORGNER: 'Erzeugung Harmonischer Strahlung mit Goldnanoantennen'. *Verhandlungen*. DPG. Dresden, 2011.
6. **NILS PFULLMANN**, CHRISTIAN WALTERMANN, MILUTIN KOVACEV, VANESSA KNITTEL, RUDOLF BRATSCHITSCH, ALFRED LEITENSTORFER AND UWE MORGNER: 'Erzeugung Harmonischer Strahlung mit Goldnanoantennen'. *Verhandlungen*. DPG. Stuttgart, 2012.

---

## Curriculum Vitae

---

### Personal details

Name Nils Pfullmann  
born March the 16th, 1983 in Stade, Germany  
unmarried, German

### Education

10/2008 - 7/2012 Grant of a PhD-fellowship in the programme *Excellence in QUEST*

11/2007 - 11/2008 Diploma student at the Ultrafast Laser Laboratory  
Institute of Quantum Optics, Leibniz Universität Hannover  
Project: *cryogenic amplification of  $\mu\text{J}$  laser pulses*  
Supervisor: Prof. Dr. Uwe Morgner  
overall grade: excellent

November 2007 Diploma exams, overall grade: excellent

10/2006 - 07/2007 Visiting student at the Centre of Experimental Photonics,  
University of Oxford  
Project: *design and build-up of a low repetition rate modelocked  
Ti:Sapphire laser*  
Supervisor: Prof. Dr. Ian Walmsley

09/2003 - 11/2008 Leibniz Universität Hannover  
Studies in general physics  
Vordiplom, overall grade: excellent

2002 - 2003 Alternative Civilian Service at Hannoversche Werkstätten

1995 - 2002 Elsa-Brändström-Schule  
Abitur, overall grade: 1.0 (excellent)



---

## Acknowledgements

---

A doctoral thesis is probably not possible without the support of a number of people. In particular, I would like to thank:

My supervisor Uwe Morgner, who not only gave me the opportunity to work in an interesting and emerging field of research, but also for encouragement and trust to get this challenging experiment running.

John Tisch for taking over the review of my dissertation and making the effort to travel to Hanover for my defence.

Manfred Lein also for taking over the review of my dissertation.

Reinhard Werner for being the head of the committee.

Dieter Akemeier (FIB-samples), Vanessa Knittel and Tobias Hanke (EBL-samples), who put a lot of effort into the optimisation and fabrication of the respective nano-antennas used for the experiments.

Carsten Reinhardt for many fruitful discussion on plasmonics as well as harmonics. Moreover the proofreading was a major help to improve this thesis.

My past diploma/master students Carsten Clever and Christian Waltermann, who contributed to the success of the project with ideas, special knowledge, fruitful discussions, and endurance in the lab.

Thomas Binhammer and Stefan Rausch from *VENTEON Laser Technologies GmbH*, who readily shared a pump laser with me, when it was desperately needed, provided expert knowledge of the Ti:sapphire system as well as a very neat and easy to use interferometric autocorrelation and SPIDER-setup.

All past and present members of the *Ultrafast Laser Laboratory*, who made life in this group very enjoyable.

The offices of *Institut für Quantenoptik* and QUEST, namely Elke Hünitzsch, Katrin Pfennig, Birgit Ohlendorf and Barbara Thiele-Bode for sorting out all the organisational details and challenges involved during a PhD.

The precision mechanics workshop of the *Institut für Quantenoptik*, who produced mechanical parts precisely and – even in busy times – incredibly fast.

My eights crew, who provided distraction and fun during uncountable hours in the boat as well as on shore. Especially our present cox Caitlin Duscheness, who also provided the lectrate in an incredibly fast time and sorted out various punctuation issues.

My friend Tobias Vockerodt, who was always willing to discuss physics or anything else. Moreover his insight into graphical design and his feedback greatly improved this thesis.

My parents and my family for love and constant support throughout the years. Without you, I would not have achieved my past and present goals.

Above all, I would like to thank Dana Müller-Hoeppe. You are incredibly important for me and make me so happy.